



COUNCIL ON IONIZING
RADIATION MEASUREMENTS
AND STANDARDS

Radiation in a Digital and Virtual World

28TH ANNUAL VIRTUAL MEETING • APRIL 26-27, 2021

Meeting Abstracts

Table of Contents

| | |
|--|-----------|
| Special Thanks To Our Meeting Sponsors..... | 3 |
| Monday, April 26, 2021..... | 5 |
| Plenary Session | 5 |
| Varian FLASH Research Update | 5 |
| Radiation processing dosimetry – From dosimeter to distribution | 6 |
| Technical aspects on the development and use of standards | 7 |
| Junior Investigator Symposium (2020 awardees)..... | 8 |
| Investigations of Well Chamber Altitude Corrections for Novel Low Energy Photon Brachytherapy Sources | 8 |
| Efficient method for daily quality assurance of an MR-Linac using time-gated scintillation imaging | 11 |
| Validating current-mode operation of the Nested Neutron Spectrometer under high neutron fluence-rates in radiation therapy using a novel passive system with gold foils..... | 14 |
| Measurements of a new Xofigo Axxent source model using an A26 microionization chamber..... | 18 |
| Junior Investigator Symposium (2021 awardees)..... | 21 |
| Uncertainty analysis of radiochromic film dosimetry at orthovoltage energy - TG-51 vs TG-61 approach | 21 |
| Volume determination of a commercially available ionization chamber | 24 |
| Towards primary and secondary standards for dosimetry in Flash radiotherapy..... | 29 |
| Tuesday, April 27, 2021..... | 31 |
| Medical Applications Subcommittee | 31 |
| Applications of plastic scintillation dosimetry for radiation oncology: A startup founder perspective | 31 |
| Evaluation of proton dose accuracy improvements with dual-energy CT | 32 |
| Challenges in multi-center quantitative imaging for TRT dosimetry..... | 33 |
| Industrial Applications Subcommittee | 34 |
| Current solutions and needs in dosimetry for radiation processing applications..... | 34 |
| Chip-scale, integrated photonics for radiation dosimetry and calorimetry | 35 |
| Recent advances towards a deployable emergency response dosimetry system (ERDS)..... | 36 |
| Radiation Safety and Security Subcommittee | 37 |
| Performance testing samples in radioactivity analysis: What they are and how to choose the appropriate ones | 37 |
| A new technology that will help radiation labs be more productive and safer | 38 |
| Additional Abstracts | 39 |
| Proffered Abstracts from 2020 Meeting (canceled due to COVID-19 pandemic) | 39 |
| Measurement and modeling of the radioactivity of neutron-irradiated jade | 39 |

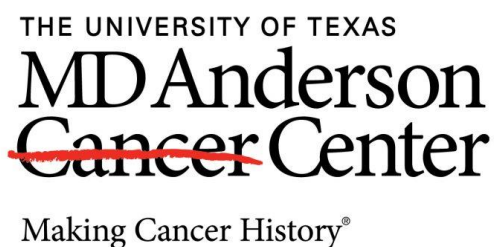
| | |
|---|-----------|
| Characterization and inter-calibration of laboratory irradiation sources used for multiple solid-state dosimetry modalities | 40 |
| Proficiency testing for interlaboratory comparison of dosimetry systems | 41 |
| Development of a fast neutron spectroscopic/imaging system using a Ga ₂ O ₃ -based scintillator | 42 |
| Development of advanced materials for the extraction of uranium from seawater | 43 |
| Performance of 2nd-generation FNTD reader in neutron-dose measurements..... | 44 |
| Space-based ionosonde receiver and visible limb-viewing airglow sensor (SIRVLAS): A CubeSat instrument suite for enhanced ionospheric charge density measurements | 45 |
| The primary standard for neutron emission rate at the National Research Council Canada..... | 46 |
| Equivalency of an X-Ray and a ¹³⁷ Cs irradiator - It's more than just comparing energy spectra..... | 47 |
| Contributions to commissioning of proton centers with new modes of delivery techniques | 48 |
| Validating ⁴⁸ VO(acac) ₂ synthesis through <i>in vivo</i> and <i>in vitro</i> studies..... | 49 |
| Imaging dose in breast radiotherapy by X-ray CT calibration of Cherenkov light..... | 53 |
| Quantifying uncertainty in microdosimetric measurements for carbon ion radiotherapy | 57 |
| Unstructured mesh unification for MCNP6.2 | 59 |
| An open-source algorithm to standardize neutron spectra unfolding in radiation therapy..... | 63 |
| Mevex's new radiation transport library for CAD models: an open-source collaboration between Mevex and the Canadian National Research Council | 66 |
| A statistical analysis of HDR Ir-192 customer well chamber calibrations at an ADCL | 70 |
| Proffered Abstracts from 2021 Virtual Meeting | 74 |
| A compact storage phosphor dosimeter attachable to smart phones for widely deployable radiation monitoring and measurements | 74 |
| Rapid HPGe well detector gamma bioassay of ¹³⁷ Cs, ⁶⁰ Co, and ¹⁹² Ir method | 75 |
| High energy X-ray fruit irradiation qualification with Monte Carlo code..... | 76 |
| Low-energy, high-production x-ray for food irradiation and sterilization | 77 |
| A kinetic model of CH ₄ conversion into H ₂ and hydrocarbons by electron beam irradiation | 78 |
| Radiation measurements for dosimetry with ionization chambers and hybrid pixel detectors | 79 |
| Dosimetry auditing in the time of COVID: Overcoming border closures through relocation and remote auditor support.... | 80 |
| Design of operational radiation protection in commissioning of compact proton therapy centers (CPTC) | 81 |
| Ne-22 Ion-beam radiation damage to DNA: From initial free radical formation to resulting DNA-base damage | 83 |
| Number of replacement of oxygen atom by sulfur in the phosphate group dictates the directionality of hole transfer between base and backbone | 84 |
| Comprehensive beam characterization and feedback for FLASH-RT using radioluminescent dosimeters..... | 85 |
| Quantifying the effects of beam and tissue properties on reemitted Cherenkov light during external beam irradiation | 88 |
| Characterization of phosphorescent strontium aluminate as a real-time dosimeter | 89 |
| Investigating the accuracy of a general cavity theory through Monte Carlo simulations..... | 90 |
| Dosimetric characterization of individual electron FLASH beam pulses from a LINAC using radioluminescence and Cherenkov imaging | 91 |

Special Thanks To Our Meeting Sponsors

Sponsors of the Junior Investigator Competition



Other Generous Sponsors



DEPARTMENT OF MEDICAL PHYSICS
Medical Radiation Research Center
UNIVERSITY OF WISCONSIN
SCHOOL OF MEDICINE AND PUBLIC HEALTH

Hidex range of instruments

LabLogic Wilma
In-Line LSC



Hidex 600 OX
Six-Sample Oxidizer



Hidex AMG
NaI Gamma Counter



Hidex 300 SL
Benchtop LSC



Hidex 600 SL
High Capacity LSC



Hidex Q-ARE
Eichrom Extractor



www.lablogic.com

© 2021 LabLogic Systems Ltd

LANDAUER®

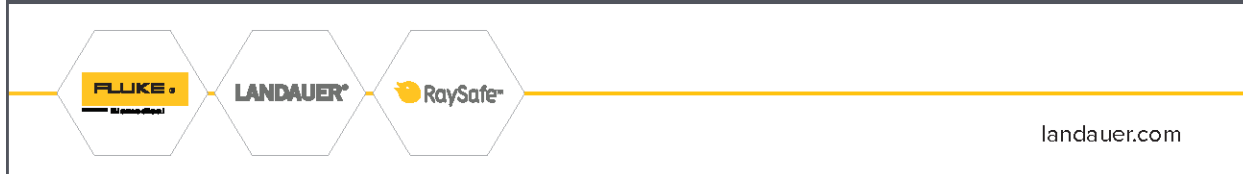
LANDAUER is proud to sponsor the 2020 Council on Ionizing Radiation Measurements & Standards Meeting and student presenter

Autumn E. Walter

University of Wisconsin – Madison, Medical Radiation Research Center

Measurements of a new Xoft Axxent Source Model using an A26 Microionization Chamber

LANDAUER joins RaySafe and Fluke Biomedical in delivering quality radiation safety products and services.



landauer.com

Monday, April 26, 2021

Plenary Session

Varian FLASH Research Update

Adam Harrington

Varian Medical Systems, Inc, adam.harrington@varian.com

The Varian FlashForward initiative can be characterized by three main categories: basic science research, new technology development, and clinical evidence generation. A comprehensive overview of the current FlashForward Consortium (FFC) pre-clinical proton research showing the first results of normal tissue sparing with a scanned pencil beam will be presented covering a wide variety of animal models and tissue types.

In addition to generating an ever growing body of preclinical evidence, the FFC has also launched the first in-human proton FLASH clinical trial. The FAST-01 Feasibility Study of FLASH Radiotherapy for the Treatment of Symptomatic Bone Metastases (FAST-01), currently accruing at the Cincinnati Proton Center, is just the first FFC trial on the path toward creating a body of evidence to enable the eventual clinical use of FLASH therapy. Details of the FAST-01 protocol and delivery methodology will be provided.

Finally, all of the exciting research presented above has been enabled by the development FLASH specific technology. From defining a framework for FLASH dose rate under pencil beam scanning delivery, to the engineering of ultra-high dose rate compatible devices as well as innovating new methods to deal with new treatment planning paradigms introduced by FLASH, the FFC and Varian have worked together to provide comprehensive solutions. Current developments and future directions will be presented.

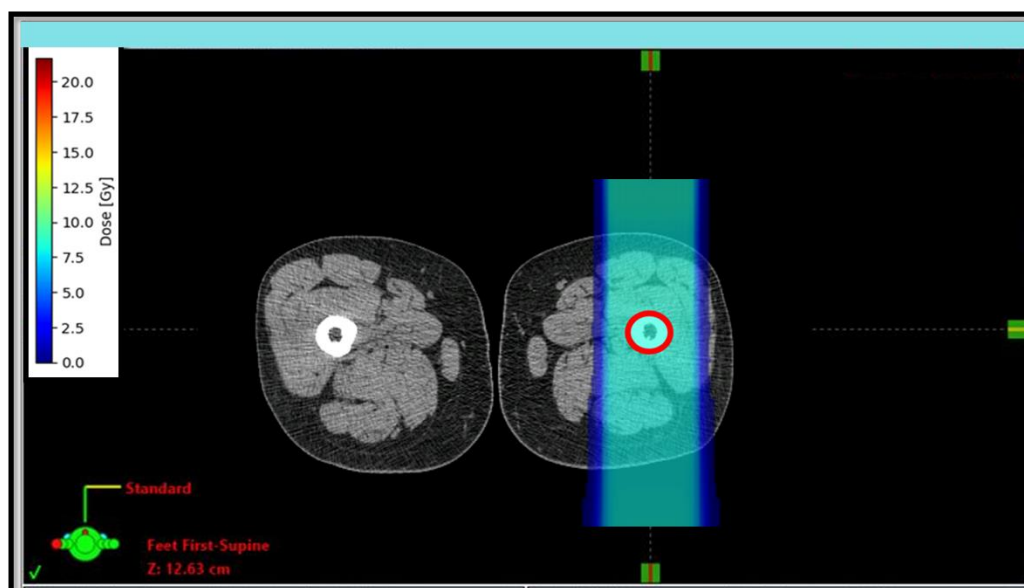


Figure 1. Single Field Image-Guided Treatment of Femur Metastasis

Radiation processing dosimetry – From dosimeter to distribution

Malcolm McEwen

National Research Council Canada, Ottawa, ON, Malcolm.McEwen@nrc-cnrc.gc.ca

The radiation sterilization of medical products can be viewed as a problem similar to the delivery of radiation therapy for cancer treatment: the aim is to deliver a homogeneous and efficacious dose to an inhomogeneous 3-D object. Whereas radiation therapy has, for decades, used complex simulations (treatment planning systems) combined with limited experimental validation (1-D or sometimes 2-D), radiation processing has relied on extensive experimental dose mapping. This latter process requires a large number of dosimeters, is therefore costly in equipment and time, and does not necessarily provide the full 3-D dose distribution that is required. This presentation will explore the transition that is occurring within the radiation processing community to implement advanced radiation simulation models to provide additional insight improve efficiency and accuracy, and provide a process that is easier to adapt to new delivery systems (energy, type of radiation, geometry, etc).

Technical aspects on the development and use of standards

Leticia Pibida

National Institute of Standards and Technology, Gaithersburg, MD, leticia.pibida@nist.gov

Documentary standards are great tools for many applications that rely on ionizing radiation measurements used routinely in the field of radiation protection, homeland security, nuclear medicine, nuclear power, radiation instrumentation and source manufacturing, etc. These standards are published by National and International organizations such as International Electrotechnical Commission (IEC), the International Organization for Standardization (ISO), the Institute of Electrical and Electronics Engineers (IEEE) and the American National Standards Institute (ANSI) with the goal of addressing different measurement needs for many applications. Depending on the type of standard (e.g., ANSI, ASTM, IEC, ISO, IEEE) they address different aspects for the different types of instrumentations. For example, standards developed under ANSI, IEC or IEEE mainly focus on performance and design requirements and their associated test methods. These standards are mainly used for procurement, calibration and setup of radiation detection instruments. While standards such as ASTM and ISO concentrate on the use and applications of different types of instruments. These are mainly used for developing laboratory and field procedures, for example to carry out measurements or sample collections. Other standards developed under these organizations can also cover data format, computer firmware and software. Many standards are used as part of regulations, guidance or procurement processes.

This presentation will focus on standards developed for two specific applications:

- IEC and ANSI standards developed for homeland security and detection of illicit trafficking of radioactive materials
 - IEC standards developed for radioactivity and radiation protection measurements.
-

Junior Investigator Symposium (2020 awardees)

(junior investigator awardee underlined)

Investigations of Well Chamber Altitude Corrections for Novel Low Energy Photon Brachytherapy Sources

Jacob Lambeck, Wendy Kennan, and Larry DeWerd

Medical Radiation Research Center, University of Wisconsin at Madison, Madison, WI,
jlambeck@wisc.edu

Objective: To determine the air kerma strength of their brachytherapy seeds prior to implant, a common practice in the clinic is the use of an air communicating well-type ionization chamber. A number of correction factors are applied to the raw electrometer signal, including a correction to standard temperature and pressure [1]. This correction has been shown to overcorrect the signal for low energy photon sources at low ambient air pressures, such as those typically found at high altitudes [2]. An additional pressure correction (P_A) to account for this effect is applied after the standard temperature and pressure correction. This correction is calculated as:

$$P_A = k_1[P(mmHg)]^{k_2}$$

where the coefficients k_1 and k_2 are dependent on the source and model of chamber used. This work focused on the determination of the pressure corrections for a new Cesium-131 (Cs-131) low energy photon brachytherapy source called Cesium Blu from Isoray Inc. and a directional Palladium-103 (Pd-103) source called the CivaDot from CivaTech Oncology Inc.

Materials and Methods: A purpose-built pressure chamber was constructed in the past which could achieve pressures ranging from 560 mmHg to 800 mmHg. Three of each source were tested over this pressure range in increments of 20 mmHg in three Standard Imaging (Middleton, WI) HDR1000+ chambers, and the Cs-131 sources were also tested in two Standard Imaging (Middleton, WI) IVB1000 chambers. Both chambers are air communicating well-type ionization chambers. Three runs of each source/chamber combination were completed. The standard temperature and pressure correction was applied to the average result at each pressure then normalized to the result at 760 mmHg. The chamber response was also simulated using MCNP6 to validate the experimental results.

Results: Both the HDR and IVB results followed the expected form of a power fit and the correction coefficients obtained from the fits are listed in Table 1. The responses for the planar CivaDot were averaged over all four cardinal directions.

Conclusions and Significance: The correction factors for Cs-131 in the HDR1000+ and IVB 1000 well chambers were different from those determined for other low energy brachytherapy sources, such as Palladium-103 and Iodine-125. The factors for these other sources in both chambers were within error of each other, so a single pair of correction factors could be used independent of chamber model. However, the responses of the two chambers (HDR 1000+ and IVB 1000) with Cs-131 were different enough such that it necessitated a difference in correction

factors. Thus, clinics must be careful to use the factors which correspond to the specific chamber model they use for air kerma strength calculations.

This difference was predicted through analysis of Monte Carlo models for the behavior of low energy photons in the chambers. Through a combination of larger active regions in the IVB 1000 and the higher energy of Cs-131 than Pd-103 or I-125, the differences in energy deposition between the chambers are exacerbated to a point where their pressure responses no longer fall within error of each other [3]. If new low energy photon brachytherapy sources are developed at an energy higher than the 30.4 keV Cs-131 source, care must be taken to experimentally test both chambers' pressure response.

The directionally averaged result for the CivaDot had good agreement with previously published Pd-103 values. The Monte Carlo calculated chamber response agreed with the experimental results within 2% for all sources and chambers at all pressures.

Relevance to CIRMS: As CIRMS has noted, brachytherapy is becoming a widely used option to treat prostate cancer [4]. This work demonstrates the importance of rigorously testing new products in a variety of situations as opposed to assuming they respond similarly to those previously used. While NIST has a calibration for these sources, the well chamber response was not measured. Due to the equipment and time needed to perform the experiments, Standards Labs are uniquely positioned to investigate new developments in the use of radiation much faster than many end users. For medical uses, this allows clinics to implement improvements in patient care sooner, fostering positive interactions between the Standards Labs and clinics. The first author intends to become a clinical medical physicist and currently works in a research laboratory which focuses on metrology. To complete this project, the first author learned how to correctly measure low dose rate brachytherapy sources and the importance of properly applying the necessary correction factors. These are skills that the author will take into their clinical work and share with future colleagues.

References

1. P. R. Almond, P. J. Biggs, B. M. Coursey et al., "AAPM's TG-51 protocol for clinical reference dosimetry of high-energy photon and electron beams," *Med. Phys.* 26(9), 1847–1870 (1999).
2. S. L. Griffin, L. A. DeWerd, J. A. Micka, and T. D. Bohm, "The effect of ambient pressure on well chamber response: Experimental results with empirical correction factors," *Med. Phys.* 32(3), 700–709 (2005).
3. T. D. Bohm, S. L. Griffin, P. M. DeLuca, and L. A. DeWerd, "The effect of ambient pressure on well chamber response: Monte Carlo calculated results for the HDR 1000 Plus," *Med Phys.* 32(4), 1103–1114 (2005).
4. CIRMS, "About Us," *CIRMS*. cirms.org/aboutus. Web.

Table 1. Table of coefficients to be used with the P_A correction factor as obtained from analytical curve fitting.

| Source | k_1 | k_2 |
|------------------------------|--------|--------|
| Cs-131 (HDR1000+) | 0.0587 | 0.4275 |
| Cs-131 (IVB1000) | 0.0829 | 0.3748 |
| CivaDot (Pd-103 in HDR1000+) | 0.0233 | 0.5665 |

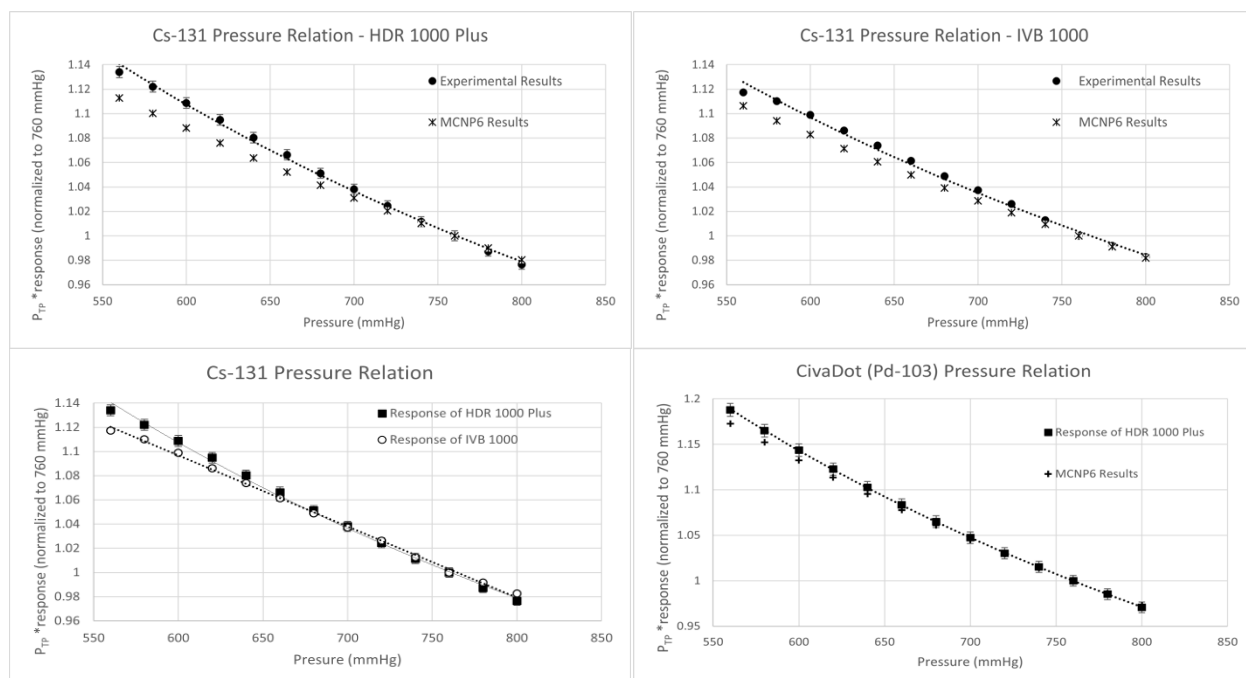


Figure 1. Pressure responses for Cesium Blu and the CivaDot at varying pressures. Upper plots show comparisons between experimental results and results from MCNP6 for both chamber models with a Cesium Blu Source. Bottom left plot compares the experimental results for the Cesium Blu source in both chambers. Bottom right plot shows comparison between experimental results and results from MCNP6 for the CivaDot source in the HDR 1000+ chamber.

Efficient method for daily quality assurance of an MR-Linac using time-gated scintillation imaging

Daniel A. Alexander¹, Rongxiao Zhang^{2,3}, Petr Bruza¹, Brian W. Pogue^{1,2,3}, David J. Gladstone^{1,2,3}

¹*Thayer School of Engineering, Dartmouth College, Hanover, NH,*

daniel.a.alexander.th@dartmouth.edu

²*Geisel School of Medicine, Dartmouth College, Hanover, NH*

³*Norris Cotton Cancer Center, Dartmouth-Hitchcock Medical Center, Lebanon, NH*

Purpose: The arrival of magnetic resonance guided radiation therapy (MRgRT) has posed a challenge for many current quality assurance (QA) protocols, as MRgRT systems do not include onboard x-ray imagers often used to make regular measurements, and many detector arrays for routine QA are not MR-compatible. Optical imaging of radioluminescence signals has been shown to be a reliable and efficient method for QA and *in vivo* dosimetry [1,2], and can provide a rapid, MR-compatible solution for performing daily QA tasks. In this study, a method is proposed for measuring output, symmetry, field centering and multileaf-collimator (MLC) position of a MR-linac using a time-gated, intensified camera and a scintillation screen, with the sensitivity of this system to possible variations in beam parameters characterized.

Materials and Methods: This study was performed using a 0.35 T MR-linac (MRIdian, ViewRay, Cleveland, OH). In order to image optical signals generated by the 6 MV flattening filter free (FFF) beam, an intensified CMOS camera (C-Dose Research, DoseOptics LLC, Lebanon, NH) was mounted on the wall facing into the bore, at a distance of 5.5 m to isocenter and an angle of 13 degrees. The camera was remotely triggered to the rep rate of the linac using an internal stray x-ray detector, and the intensifier was gated to the pulse width of the linac, allowing for substantial suppression of background light. All images were background subtracted and a flat-field correction was applied. A 14 x 17 inch scintillation screen (Blue 400, Penn Jersey X-Ray, Jacksonville, FL) was centered at isocenter using lasers in the x- and y- dimensions, with the z-position lowered completely to provide the best view from the camera (Figure 1). The screen was placed on top of a 2 cm slab of solid water to provide adequate backscatter. A 6 x 7 square checkerboard was placed at the same position as the screen, which was used to apply a projective transformation to all optical images and convert them to a beam's eye view. Varying numbers of monitor units (MUs) were delivered by the linac at a fixed field size of 14.94 x 14.94 cm to test output response of the scintillation screen. Subsequently, various square field sizes ranging from 3.32 x 3.32 cm to the maximum field size of 27.40 x 24.07 cm were used to irradiate the sheet, to assess crossplane (x) and in-plane profiles (y) measured from the optical signal captured by the camera. Additionally, the 14.94 x 14.94 field was shifted from -3 to +3 mm in the x-direction programmatically using the MLC to characterize the system's sensitivity to small spatial deviations. Lastly, an MLC picket fence test was performed by irradiating the screen with a thin field at various x-positions, and the measured optical line profile was analyzed to reproduce and verify the preprogrammed MLC positions.

Results: The optical emission from the scintillation screen was found to be sensitive to deviations in output of 0.5%, and the signal was found to be linear with the number of MUs

delivered ($R^2 = 0.99$). The full widths at maximum of the measured crossplane profiles were compared to the defined field sizes, with a minimum discrepancy of 0.3 mm at 3.32 cm field size, and a maximum discrepancy of 3.7 mm at 27.4 cm field size (Figure 2). Additionally, the measured shifts from the optical images matched the programmed field shifts in the x-direction with discrepancies ranging from 0.2 mm to 1.0 mm, with an average absolute discrepancy of 0.7 mm (Figure 3). Lastly, field positions from the picket fence test were measured by finding the prominent local maxima of a line profile integrated along the y-direction in the optical image, reproducing the MLC positions with < 2 mm discrepancy (Figure 4) (tolerance 2mm).

Conclusions: This study suggests that a gated intensified camera coupled with a scintillation screen can provide valuable output and symmetry information for consistency in daily QA of an MR-linac. The system shows high sensitivity to shifts in position and output and can reproduce positional information with milliliter-level precision in many cases. Since daily QA concerns relative changes from day to day, absolute discrepancy is not a concern, as it can be included in the baseline measurement. Future work will involve making heterogeneity corrections for the screen itself, as well as combining the optical imaging technique with an MR phantom to perform MR-MV co-isocentricity measurements.

Relevance to CIRMS: This work aligns with the goals of the CIRMS medical subcommittee, specifically in how it supports development of procedures which ensure safe and accurate delivery of intensity modulated radiation therapy. Quality assurance in the radiation therapy clinic is essential to patient safety and treatment efficacy, and improvements in efficiency and accuracy of these protocols directly supports these efforts. This study is a component of the first author's doctoral work, which consists of translating Cherenkov and radioluminescence imaging to the clinic in various capacities, including patient surface dosimetry and QA.

References

- 1) Ashraf MR, Bruza P, Pogue BW, et al. Optical imaging provides rapid verification of static small beams, radiosurgery, and VMAT plans with millimeter resolution. *Med Phys*. doi:10.1002/mp.13797
- 2) Tendler I, Brůža P, Andreozzi J, et al. Rapid Multisite Remote Surface Dosimetry for Total Skin Electron Therapy: Scintillator Target Imaging. *Int J Radiat Oncol*. 2019;103(3):767-774. doi:10.1016/j.ijrobp.2018.10.030

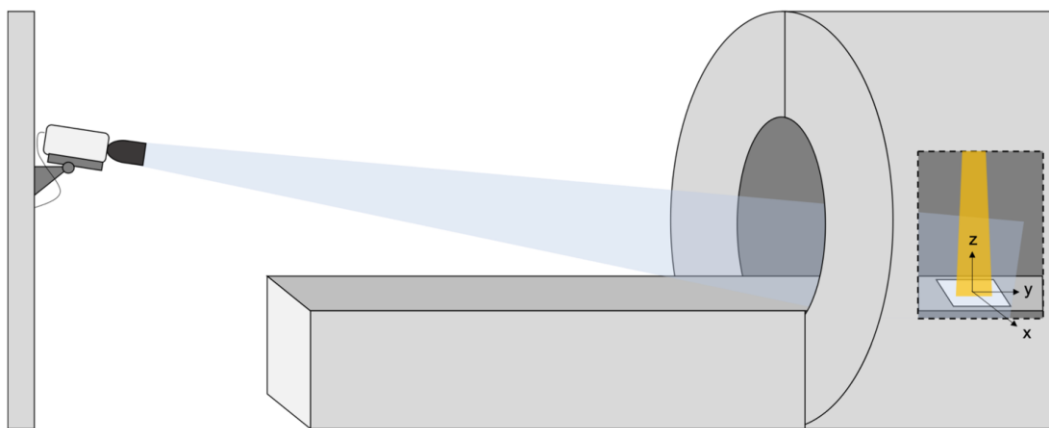


Figure 1. Drawing of the room setup. The camera is mounted on the wall, and the scintillation screen is placed at the beam isocenter and irradiated from above.

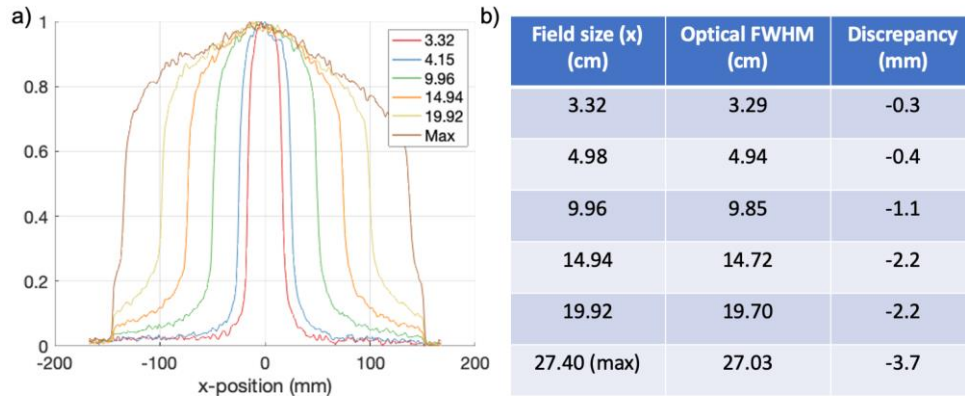


Figure 2. (a) Crossplane profiles measured from the optical data at various field sizes; (b) Table displaying programmed field sizes, field width measured at half maximum of each profile, and the discrepancy between the two.

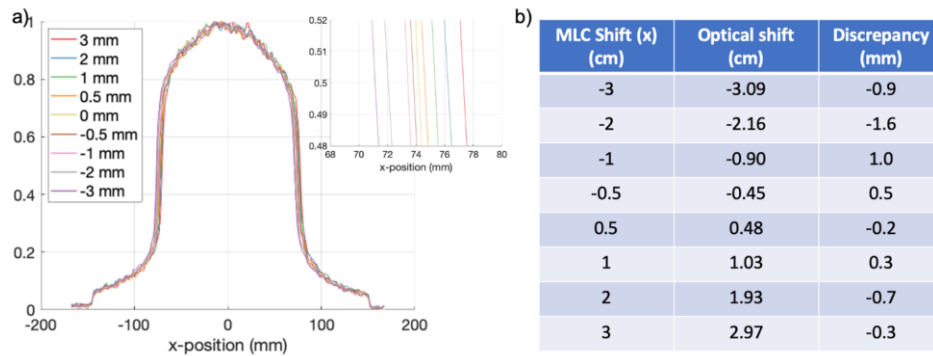


Figure 3. (a) Crossplane profiles measured from the optical data at various x shifts for a 14.94 x 14.94 cm field , with zoomed view ; (b) Table displaying programmed MLC shifts, shifts measured using the optical profiles, and the absolute discrepancy between the two.

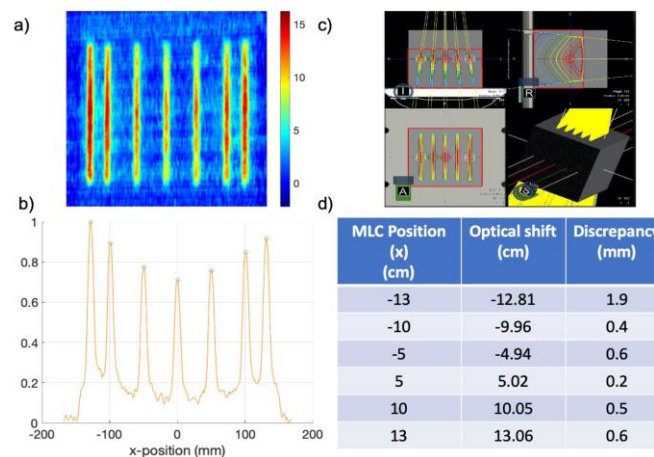


Figure 4. (a) Transformed cumulative optical data from the MLC picket fence test; (b) Lateral profile of optical data integrated along the y direction; (c) TPS view of picket fence plan; (d) Table showing programmed MLC positions, measured positions, and discrepancy between the two.

Validating current-mode operation of the Nested Neutron Spectrometer under high neutron fluence-rates in radiation therapy using a novel passive system with gold foils

Felix Mathew¹, Cornelia Chilian², Logan Montgomery¹, and John Kildea¹

¹*Medical Physics Unit, McGill University, Montreal, QC, H4A3J1, Canada, felix.mathew@mail.mcgill.ca*

²*Department of Engineering Physics, Polytechnique Montreal, Montreal, QC, H3T 1J4, Canada*

Objective: Nested Neutron Spectrometers™ (NNS, Detec Inc., Gatineau, QC) are commercially available Russian-doll type neutron spectrometers that use He-3 counters for thermal neutron detection [1]. These spectrometers are calibrated by the vendor at the Ionizing Radiation Standards Laboratory of the National Research Council of Canada (IRS-NRC) using a reference Am-Be neutron source. During the calibration, akin to the method of Hagiwara et al. 2011 [2], a conversion factor is determined to convert the accumulated charge measured in current-mode operation to the number of neutrons that interacted with the sensitive volume of the He-3 detector. This calibration factor is provided to end-users, typically for determining neutron spectra at a particle accelerator or nuclear power plant environments where neutron fluence-rates are high. However, the accuracy of the conversion factor obtained using the Am-Be source (low neutron fluence-rate) is questionable when the neutron fluence-rates are high and beyond the range of calibration. A direct validation in a high fluence-rate environment is also impossible as the pulse-mode (an operation mode in which the number of neutron pulses is measured directly) fails due to pulse pile-up. Therefore, in this study, we sought to indirectly validate the current-mode of the NNS in a high fluence-rate environment using passive gold-foil neutron detectors.

Materials and methods: We developed a novel passive-NNS by replacing the He-3 detector with a gold-foil disc (8 mm radius, 0.1 mm thick and 19.3 g cm⁻³ density) placed between two cylindrical inserts (Figure 1). The gold activation foil was positioned horizontally at the geometric center of the moderators of the NNS. Unlike the original active-NNS, the passive version does not suffer from pulse pile-up when used under high neutron fluence-rates. Hence, we used both the active and passive NNS to determine and compare the neutron spectra generated by the 15 MV beam of a Varian TrueBeam STx linac at the location of measurement (1 m away from the isocenter along the treatment-couch axis at the isocenter height) in a radiotherapy bunker of the McGill University Health Centre (MUHC) as shown in Figure 2.

The spectral measurement procedure for the active NNS is well established [3]. The electrometer connected to the He-3 detector of the NNS measures the total charge accumulated in the He-3 detector during the irradiation. Using the vendor-provided response functions, calibration factor and an input guess spectrum the raw data are unfolded into a neutron fluence-rate spectrum using the modified MLEM-STOP algorithm [4]. The passive NNS on the other hand requires more elaborate pre-processing steps to obtain unfoldable raw data. Gold-foils get activated via the neutron capture reaction in a neutron field. The activated gold isotope (Au-198) radiates a characteristic photon of energy 412 keV with a half-life of 2.7 days. With a suitable gamma-ray spectrometer, the characteristic photon can be identified and the

saturation activity of the foil can be determined. In our study, we used a High Purity Germanium (HPGe) detector at the SLOWPOKE neutron activation analysis laboratory of Polytechnique Montreal.

The response functions of the passive NNS that were needed to unfold the foil saturation activity data—to obtain the neutron fluence-rate spectra—were generated through Monte Carlo simulations of the spectrometer in Geant4 (version 10.4. patch-2). The passive NNS with gold-foils was modelled accurately and its neutron interactions were simulated using the QGSP_BIC_HP physics model in Geant4. The response, defined as the ratio of the number of neutron capture reactions to the neutron fluence, was thus obtained and used to unfold the foil saturation activity data using the modified MLEM-STOP algorithm as for the active NNS.

Results: The response functions of the passive system with gold foil, as obtained from the Monte Carlo simulations in Geant4 for different moderator shell configurations, are shown in Figure 3. Figure 4 shows the neutron fluence-rate spectra obtained at the location of measurement during the irradiation of the 15 MV beam in the radiotherapy bunker using both the active and passive NNS. The histograms plotted show the spectra obtained with the average of three repeated measurements with both spectrometers and the shaded region is the standard uncertainty of each neutron spectrum. The spectra agreed reasonably well within uncertainties.

Conclusion: In this study, a passive NNS with gold-foils was successfully developed and a functional workflow to use the spectrometer for neutron spectral measurements was established. The neutron fluence-rate spectrum at a location of interest was determined using the active NNS in its current-mode and with the passive gold-foil-NNS and compared. The spectra agreed reasonably well within uncertainties validating the accuracy of the use of the active NNS with He-3 detector in its current-mode under high neutron fluence-rate environments such as in radiotherapy.

Relevance to CIRMS: This work was done by the first author as part of his master's thesis. Through the validation of the current-mode of the active NNS, we brought the calibration from the standards lab to the end-user at high neutron fluence-rates. It is now plausible for any user to confidently perform neutron spectral measurements using this spectrometer under high neutron fluence-rates. Hence this research is relevant to the CIRMS mission. The first author, now a Ph.D. candidate, is continuing the use of this spectrometer to gain more insight into neutron-induced carcinogenic effects consistent with the mission of his research group.

References

1. Dubeau J, Hakmana Witharana SS, Atanackovic J, Yonkeu A, Archambault JP. A neutron spectrometer using nested moderators. *Radiat Prot Dosimetry*. 2012;150: 217–222.
2. Hagiwara M, Sanami T, Iwamoto Y, Arakawa H, Shigyo N, Mokhov N, et al. Shielding Experiments at High Energy Accelerators of Fermilab (III): Neutron Spectrum Measurements in Intense Pulsed Neutron Fields of The 120-GeV Proton Facility Using A Current Bonner Sphere Technique. *Progress in Nuclear Science and Technology*. 2011. pp. 52–56. doi:10.15669/pnst.1.52
3. Maglieri R, Licea A, Evans M, Seuntjens J, Kildea J. Measuring neutron spectra in radiotherapy using the nested neutron spectrometer. *Medical Physics*. 2015. pp. 6162–6169. doi:10.1118/1.4931963
4. Montgomery L, Landry A, Al Makdessi G, Mathew F, Kildea J. A novel MLEM stopping criterion for unfolding neutron fluence spectra in radiation therapy. *Nuclear Instruments and Methods in Physics Research Section A: Accelerators, Spectrometers, Detectors and Associated Equipment*. 2020. p. 163400. doi:10.1016/j.nima.2020.163400



Figure 1. The He-3 detector and its positioning inside the nested moderators of the NNS (left). The picture of the two cylindrical inserts with the gold foil in between and its positioning inside the moderators to have a passive NNS(right).



Figure 2. The passive NNS with gold foil in one of its moderator configurations at the location of measurement in the radiotherapy bunker during irradiation.

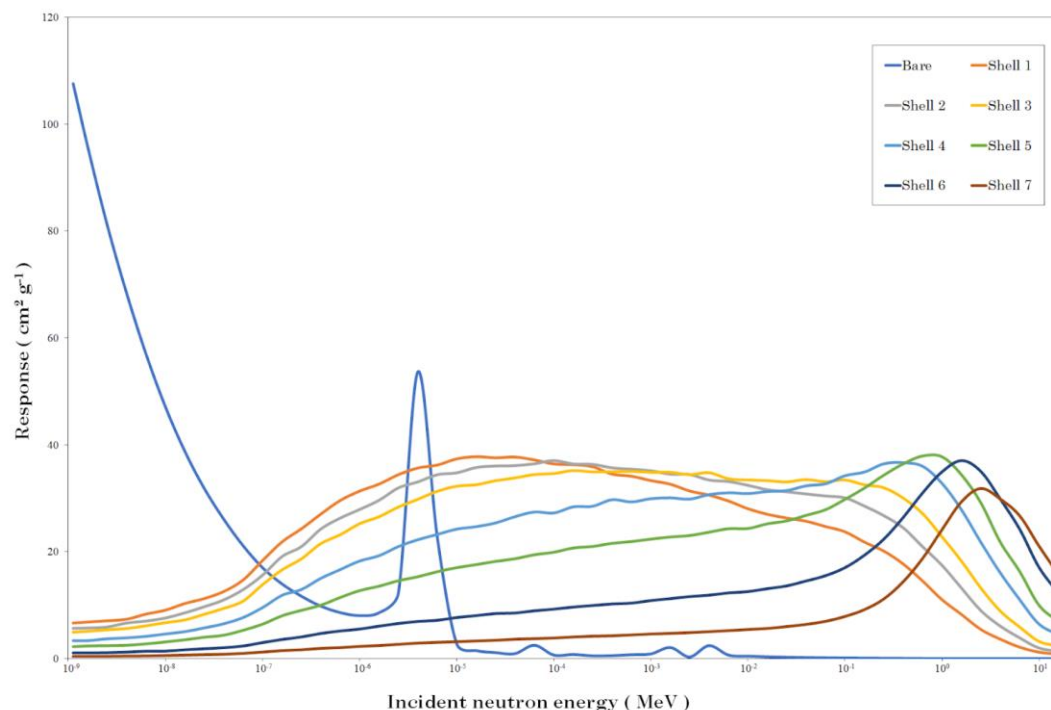


Figure 3. The response functions of the passive NNS generated via Monte Carlo modelling in Geant4. Bare represents the model when only the gold-foil with the cylindrical inserts are used and Shell 'X' corresponds to the moderator configuration in which all the moderators up to the 'X't h one are used in the model.

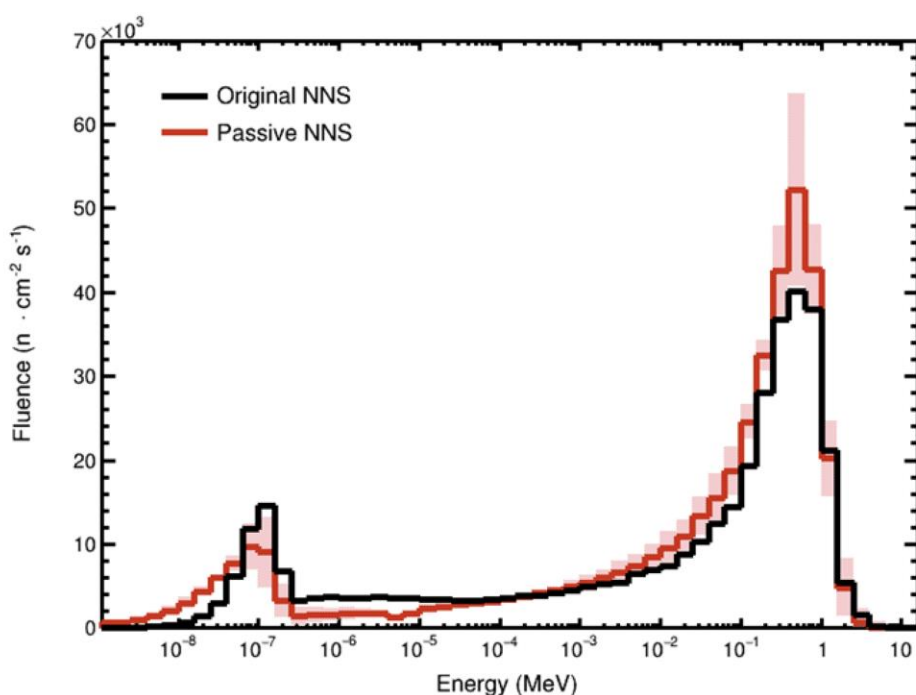


Figure 4. The neutron fluence-rate spectra obtained using the Original (active) NNS with He-3 detector and using the Passive NNS with gold-foils.

Measurements of a new Xofig Axxent source model using an A26 microionization chamber

Autumn E. Walter and Larry A. DeWerd

Department of Medical Physics, School of Medicine and Public Health, University of Wisconsin-Madison, Madison, WI, gewalter2@wisc.edu

Objective: Dosimetric characterization of electronic brachytherapy (eBt) sources has been a challenge in the field of radiation therapy due to bremsstrahlung perturbations and fluctuations in dose rate that are not present for traditional brachytherapy sources. Thus, NIST has implemented an air kerma rate standard for these sources [1,2] instead of the use of the air kerma strength standard. The implementation of this standard requires a modified dosimetry formalism [2]. Previously, implementation of this standard for the S7500 model of the Xofig Axxent electronic brachytherapy source (San Jose, CA) was done [3]. A new S7600 Axxent source model has been produced and utilizes a Galden coolant material, which has a density of 1.72 g/cc, and has an increased thickness of the anode. These changes to the source require a new air kerma rate standard to be implemented as well as measurement of the modified TG43 parameters. The previous characterization of these sources has utilized TLD-100 microcubes, as they provided high dose resolution and the most precise measurements of these miniature x-ray tubes when compared to ionization chamber or film measurements. Historically, microionization chambers with volumes suitable for these measurements have had a steep energy dependence within the range of tube potentials of these sources due to high-Z collectors, variable responses over time, and significant polarity and ionic recombination effects [4,5]. The Exradin A26 microionization chamber (Standard Imaging, Middleton, WI) has been shown not to have these issues. Thus, the focus of this work was to evaluate the use of this ionization chamber to measure some modified TG43 parameters for the S7600 source.

Methods: Air kerma rate was measured using the Attix Free Air Chamber (FAC) at the UWMRRC [6] for six S7600 Axxent sources. Charge readings were also taken in Standard Imaging HDR1000+ well chambers (Middleton, WI) with a previous NIST calibration for the S7500 sources. The FAC was used to determine source-specific calibration coefficients, as a standard has not currently been implemented for these new source models. A tentative calibration coefficient was then assigned to the well chambers from these measurements.

Measurements were then made in water with an Exradin A26 microionization chamber. An acrylic phantom (Figure 1) was used to place the active volume of the chamber at distances of 1 cm to 4 cm away from the source anode [7]. Charge readings were taken at two points separated by 180° for each of the distances. These charge readings were corrected for temperature, pressure, and electrometer and had a UW M50 calibration coefficient applied. The dose rate at each distance was calculated and used in Equation 1 to calculate the radial dose function as,

$$g(r) = \frac{\dot{D}(1 \text{ cm}, 90^\circ)}{\dot{D}(r, 90^\circ)} \frac{G(r_0, \theta_0)}{G(r, \theta_0)} \quad (1)$$

where r indicates the radial distance. The geometry function, $G(r, \theta)$ can be simplified to a point source approximation and acts as a correction for dose fall off. Additionally, the Dose Rate Conversion Coefficient, χ , can be calculated from these measurements as,

$$\chi = \frac{\dot{D}_{1 \text{ cm}}}{\dot{K}_{50 \text{ cm}}} \quad (2)$$

where $\dot{D}_{1 \text{ cm}}$ is the dose rate measured at 1 cm with the A26 chamber and $\dot{K}_{50 \text{ cm}}$ is the air kerma rate at 50 cm, determined from the FAC. Additionally, these measurements were simulated using the EGSnrc user code `egs_chamber` following the methods of Simiele [3].

Results: The tentative calibration coefficients for the well chambers for the S7600 sources were approximately 17% lower than those for the S7500 sources. This result emphasizes the need for an air kerma rate standard for the S7600 sources. The measured values for the radial dose function agreed within 2% of the simulated values. These results are shown in Table 1 and are plotted as a function of radial distance in Figure 2. Additionally, the DRCC, measured with the A26 chamber was 9.36 ± 0.212 cGy/hr per $\mu\text{Gy/min}$ and agreed within 0.9% of the simulated value of 9.44 ± 0.294 cGy/hr per $\mu\text{Gy/min}$.

Conclusion and Significance: This study successfully showed the feasibility of using an A26 microionization chamber for measurement of a subset of modified TG43 parameters for the S7600 Axxent source model. The aim of future work will be to utilize NIST traceable air kerma rate values to determine the measured values following the implementation of a standard. Additionally, these results will be used to benchmark Monte Carlo models using the TOPAS user code.

Relevance to CIRMS: This work is a subset of the doctoral work pursued by the first author to dosimetrically and biologically characterize the S7600 Axxent source model. This work relates to the CIRMS mission as these values rely on a NIST traceable standard to ensure accuracy of dose calculation for patient treatments. Additionally, the work will aid in implementation of consensus values to be used by all clinical users for patient treatment. CIRMS will help the first author achieve her goal of working as a clinical medical physicist by providing the tools and resources to conduct radiation metrology research now and in the future.

References

- 1) Ravinder Nath et al. "Dosimetry of interstitial brachytherapy sources: recommendations of the AAPM Radiation Therapy Committee Task Group No. 43". In: Medical physics 22.2 (1995), pp. 209–234.
- 2) Larry A DeWerd et al. "A modified dose calculation formalism for electronic brachytherapy sources". In: Brachytherapy 14.3 (2015), pp. 405–408.
- 3) Samantha J. Simiele. "Advancements in electronic brachytherapy dosimetry methods". PhD thesis. University of Wisconsin-Madison, 2017.
- 4) Jessica R. Miller, "Characterization and optimization of microionization chambers". PhD thesis. University of Wisconsin-Madison, 2013.
- 5) Jessica R. Miller et al. "Polarity effects and apparent ion recombination in microionization chambers." In: Medical physics 43 (2016), pp 2141-2152.
- 6) JG Coletti, DW Pearson, and LA DeWerd. "Mammography exposure standard: Design and characterization of free-air ionization chamber". In: Review of scientific instruments 66.3 (1995), pp. 2574–2577.
- 7) Tina L. Pike. "A dosimetric characterization of an electronic brachytherapy source in terms of absorbed dose to water". PhD thesis. University of Wisconsin-Madison, 2012.

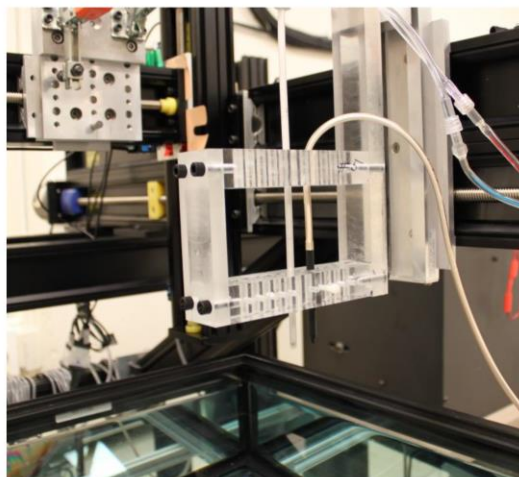


Figure 1. Acrylic phantom used to position the A26 and Axxent source [7].

Table 1. Comparison of measured and simulated radial dose function values

| <i>Radial Distance (cm)</i> | <i>A26, $g(r)$ (%)</i> | <i>MC, $g(r)$</i> | <i>Ratio (A26/MC)</i> |
|-----------------------------|-----------------------------------|------------------------------|-----------------------|
| 1 | 1.000 ± 0.002 (0.2) | 1.000 | 1.00 |
| 2 | 0.645 ± 0.002 (0.3) | 0.632 | 1.02 |
| 3 | 0.475 ± 0.003 (0.6) | 0.465 | 1.02 |
| 4 | 0.361 ± 0.005 (1.4) | 0.360 | 1.00 |

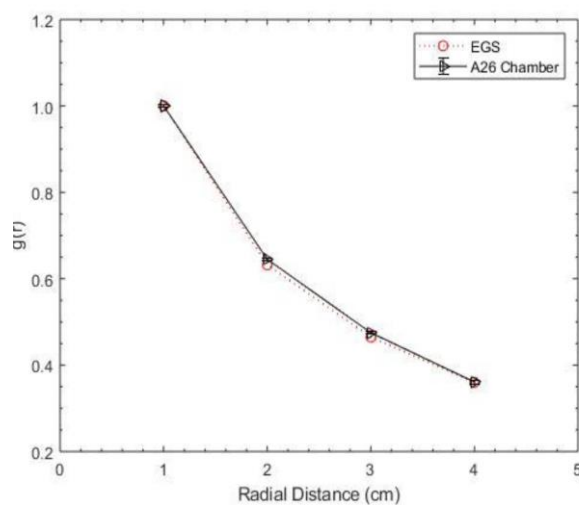


Figure 2. Simulated and measured values for the radial dose function

Junior Investigator Symposium (2021 awardees)

(junior investigator awardee underlined)

Uncertainty analysis of radiochromic film dosimetry at orthovoltage energy - TG-51 vs TG-61 approach

Drew Carlton and Quan Chen

Department of Radiation Medicine, University of Kentucky, Lexington, KY,
drew.carlton@uky.edu

Objective: Current AAPM protocol for x-ray beam dosimetry in radiobiology recommends the use of calibrated air-filled ionization chambers. Though effective for calibration setup, the experimental setup for radiobiological research is often geometrically very different than these ideal conditions. EBT3 radiochromic film offers a dosimetry technique that is very flexible in cell and small animal irradiation conditions. Most researchers calibrate EBT3 film with the same orthovoltage irradiator. The delivered dose of the orthovoltage irradiator is determined following AAPM TG-61. However, TG-61 calibration requires the use of an ion chamber calibrated by the ADCL for the kV beam quality of the orthovoltage irradiator, which is not often available at the local institution. On the other hand, most institutions have radiation therapy programs and have multiple ion chambers calibrated at MV energy. The objective of this work was to explore the feasibility of establishing EBT3 film dosimetry for use in orthovoltage irradiators with MV calibration and application of an energy correction factor. The uncertainties in EBT3 film dosimetry using kV calibration and MV calibration were analyzed and compared.

Materials and Methods: A Precision XRAD-225 was calibrated with an ionization chamber following TG61 in-air calibration procedures and then converted to surface dose. For measurements made on the XRAD-225 irradiator, two different beam qualities were used. This included the use of a 0.3 mm Cu filter and a 2.0 mm Al filter. EBT3 films were irradiated at 50cm SSD under full back scatter conditions on top of solid water blocks to establish a calibration curve (*TG61*). Films were also irradiated under a 6MV linear accelerator at d-max to establish a separate calibration curve (*TG51*). Energy responses of the film were determined from Hammer et al. (2018), together with the uncertainty value. Films were irradiated with the same exposure under kV or MV beam to characterize the variations in optical density (OD). The uncertainty of the film dosimetry was estimated following the formalism used by Marroquin et al. (2016). The relationship between dose and optical density was modeled using the form:

$$D = a \cdot netOD + b \cdot netOD^n \quad (1)$$

where a, b, and n are fitting parameters. The fitting procedure also reports the uncertainty of the fitting parameters (SD_a , SD_b). n was fixed after the initial fitting, thus $SD_n = 0$.

The dose uncertainty (relative) due to the uncertainty in net optical density reading is given as:

$$SD_{exp}(\%) = \frac{(a + n \cdot b \cdot netOD^{n-1}) \cdot SD(netOD)}{D} \cdot 100 \quad (2)$$

The dose uncertainty (relative) due to uncertainties in fitting parameters a, b is given as:

$$SD_{fit}(\%) = \frac{\sqrt{netOD^2 \cdot SD_a^2 + netOD^{2n} \cdot SD_b^2}}{D} \cdot 100 \quad (3)$$

The total uncertainty from the response curves and fitting procedures is then given as:

$$SD_{film} = \sqrt{SD_{exp}^2 + SD_{fit}^2} \quad (4)$$

However, this uncertainty analysis assumes that the dose delivered to the film has no uncertainty. In reality, absolute dose calibration of orthovoltage irradiators following TG-61 protocol has an associated uncertainty of 3.5% and absolute dose calibration of linear accelerators following TG-51 protocol has an associated uncertainty of 1%. A complete uncertainty analysis of both film calibration techniques must include these absolute dose calibration uncertainties, as in Eq. (5):

$$SD_{tot} = \sqrt{SD_{film}^2 + SD_{abs\ dose}^2} = \sqrt{SD_{exp}^2 + SD_{fit}^2 + SD_{abs\ dose}^2} \quad (5)$$

Results: For the calibration curves created with the X-RAD 225 Precession X-ray irradiator and the linear accelerator, the collected data as well as the calibration curves are displayed in Figure 1. The determined energy correction factor agreed with values previously reported by Hammer et al. (2018), suggesting that film calibration with a MV linac followed by the application of published energy correction factors is a viable alternative to orthovoltage film calibration.

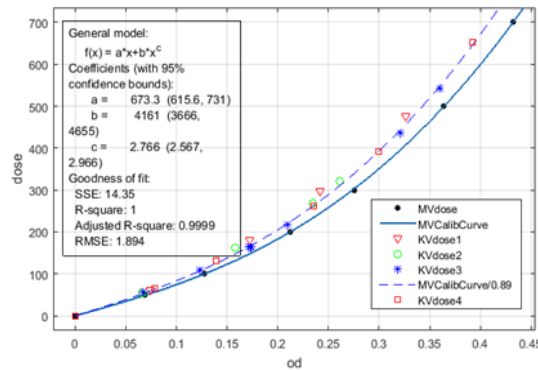


Figure 1. Comparing the calibration curve created with a 6X Linac and the XRAD-225. KVdose1 was created using the XRAD-225 with a 2.0mm Al filter. KVdose2-4 were created using the XRAD-225 with a 0.3 mm Cu filter. Energy correction factors of 0.89 for XRAD-225(Cu) and 0.88 for X-RAD-225(Al) fits our data well.

The uncertainty associated with the measured net optical density of the film was added in quadrature with the uncertainty associated with the calibration curve fitting of the film to get a film calibration uncertainty value for both techniques using Eq. (2), Eq. (3), and Eq. (4). However, these film calibration uncertainty calculations neglect the absolute dose calibration uncertainties associated with TG-61 and TG-51 which were added following Eq. (5). For MV calibration, additional uncertainties from the energy conversion factor and beam quality differences must also be added for calculation of total uncertainty.

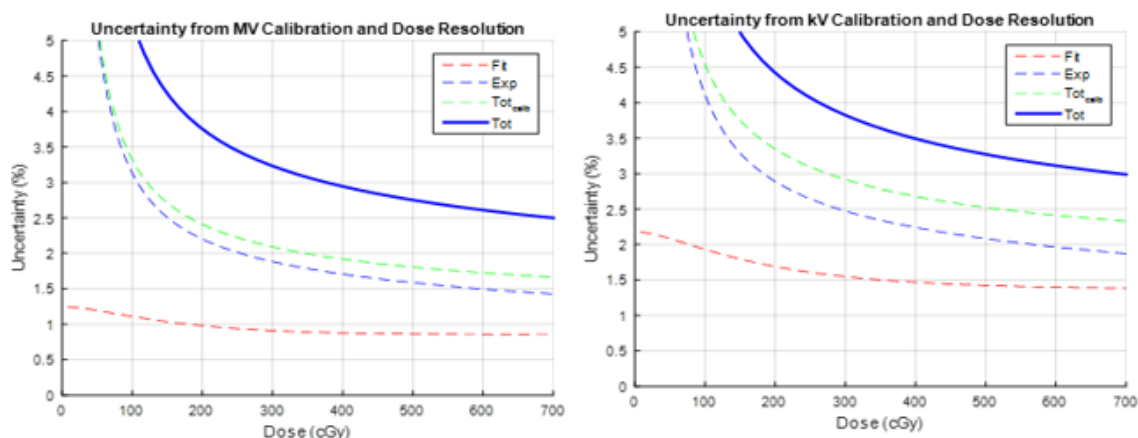


Figure 2. The dose dependence of the uncertainty associated with the calibration curve fitting (red-dashed), net optical density (blue-dashed), calibration OD measurements (green-dashed), and the OD uncertainty in actual dose measurement (solid-blue) for both the MV and KV calibration techniques.

Film calibration through TG61 was determined to have an associated total uncertainty of 5.2% at a dose of 300 cGy and film calibration through TG51 followed by the application of Hammer (2018) energy correction factor was determined to have an associated total uncertainty of 3.7% at a dose of 300 cGy.

Table 1. Dosimetric uncertainty estimation at 300 cGy.

| KV Calibration 3 | Uncertainty (%) | MV Calibration 1 | Uncertainty (%) |
|---------------------------------------|-----------------|---------------------------------------|-----------------|
| Response Curves and Fitting Procedure | 3 | Response Curves and Fitting Procedure | 2.1 |
| Dose Resolution of the System | 2.5 | Dose Resolution of the System | 2.5 |
| TG61 Absolute Dose Calibration | 3.5 | TG51 Absolute Dose Calibration | 1 |
| | | Energy Conversion Factor | 1.1 |
| | | Beam Quality Differences | 1 |
| Total Uncertainty | 5.2 | Total Uncertainty | 3.7 |

Conclusions and Significance: This work suggests that the use of film calibrated with a MV accelerator for use with orthovoltage irradiators is preferred despite the extra uncertainty from the energy conversion step. This new practice can reduce dosimetric uncertainty by 30%.

Relevance to CIRMS: The findings of this work recommend a change to current ionizing radiation dose measurement procedures in the radiobiology research setting. Accurate radiation dose reporting is critical to meaningful research in radiobiology and these findings have the potential to improve this aspect in the field. As a therapeutic medical physicist in training, the advancement of radiation therapy in the clinical setting is dependent on accurate research in the pre-clinical setting.

References

1. Almond, P. R., Biggs, P. J., Coursey, B. M., et al. (1999). AAPM's TG-51 protocol for clinical reference dosimetry of high-energy photon and electron beams. *Medical Physics*. 26(9), 1847-1870.
2. Chair, C. -M. Ma., Coffey, C. W., DeWerd, L. A., et al. (2001). AAPM Protocol for 40-300 kV x-ray beam dosimetry in radiotherapy and radiobiology. *Medical Physics*. 28 (6), 868-893.
3. Hammer, C. G., Rosen, B. S., Fagerstrom, J. M., et al. (2018). Experimental investigation of GafChromic EBT3 intrinsic energy dependence with kilovoltage x rays, ^{137}Cs , and ^{60}Co . *Medical Physics*. 45 (1), 448-459.
4. Marroquin, E. Y. L., Gonzalez, J. A. H., Lopez, M. A. C., et al. (2016). Evaluation of the uncertainty in an EBT3 film dosimetry system utilizing net optical density. *Journal of Applied Clinical Medical Physics*. 17(5), 466-481.

Volume determination of a commercially available ionization chamber

Emily J King and Larry A DeWerd

Department of Medical Physics, School of Medicine and Public Health, University of Wisconsin-Madison, Madison, WI, eking24@wisc.edu

Objective: Known-volume ionization chambers are predominantly limited to use at primary standards laboratories due to the difficult nature of fabricating and verifying the volumes of the chambers. This work investigates using micro-CT imaging techniques to precisely quantify the volumes of commercial ionization chambers.

Methods: Two Exradin A3 ionization chambers were imaged using a Siemens (Munich, Germany) microCT/microPET hybrid scanner with 50 μm resolution. The raw DICOM data was analyzed in MATLAB to determine the ISO50 threshold of the wall surfaces. The ISO-50% method is a global method of surface determination based on a static threshold value [1]. This method is used commonly in additive manufacturing quality assurance. It addresses the problem of the partial volume effect where material and background partially overlapping receive an intermediate grey value which gives the appearance of blurring. The ISO50 value is the sum of the average material grey Hounsfield Unit (HU) value and the average background grey HU value divided in half. This value is used as a threshold where every HU value above the threshold is considered material and every HU value below is considered background. The ISO-50% method is used in this work to define the inner and outer walls of the ionization chamber to determine the physical volume and wall thickness of the chambers. To properly determine the physical volume, the surfaces of the collecting electrode and the guard were also defined. Contours of the chambers were then created with the ISO50 thresholds in the Siemens Inveon Research Workplace imaging software, as shown in Figure 1.

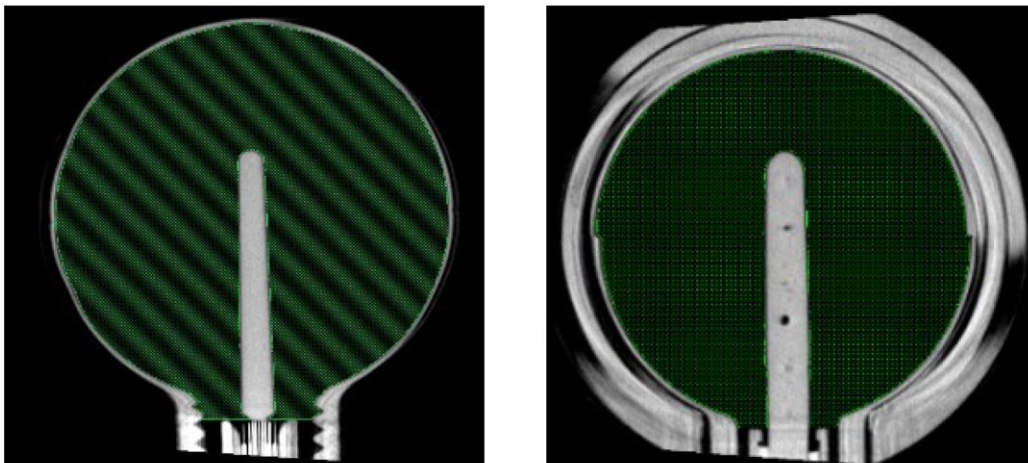


Figure 1. MicroCT images of the two Exradin A3 ionization chambers used for this project with their volume contours shown in green

The collecting volume of the ionization chambers differ from the physical volumes due to a portion of the electric field terminating in the guard instead of the collecting electrode. The electric field was modeled in COMSOL Multiphysics to quantify this discrepancy [2], as shown in

Figure 2. The area under the curve where the electric field still reaches the collecting electrode, rather than the guard, was converted to a volume by rotating the area around the collecting rod. This assumes the electric field is symmetric about the collecting rod. The equation for rotating the area around the collecting rod is

$$V = 2\pi \int_a^b r \cdot f(r) dr,$$

where a is the radius at the collecting rod, b is the radius at the stem, r is the radius of each bin and $f(r)$ is the height of the electric field at each bin. This volume was then subtracted from the physical volume determined by the contours. To account for magnification in the CT images, a magnification factor was calculated and applied. A validation of these volumes was done by comparing them to the volumes calculated by a Co-60 air kerma calibration. The volume of an ionization chamber is calculated from its exposure calibration coefficient with the following expression:

$$V = \frac{1}{\rho N_X},$$

where ρ is the density of air and N_X is the exposure calibration coefficient.

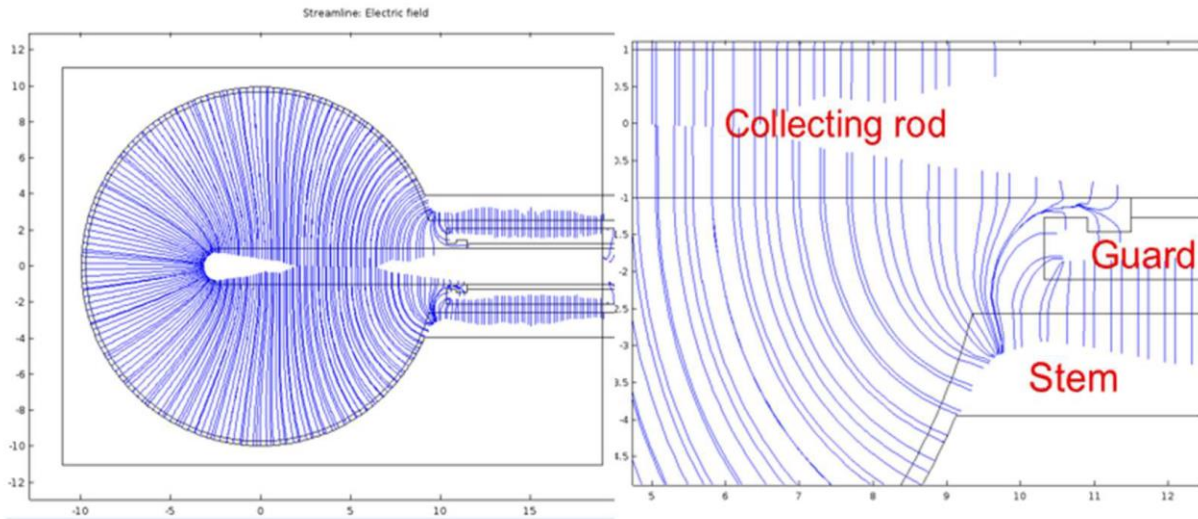


Figure 2. COMSOL model of the electric field in an Exradin A3 ionization chamber (left). The same COMSOL electric field model focused on the area of interest near the guard (right).

Known-volume chambers require correction factors for the walls, stopping powers, air attenuation, radiation yield and humidity. These correction factors were calculated with various EGSnrc (Electron Gamma Shower, National Research Council of Canada) user codes and NIST values. Table 1 shows a definition of each correction factor and how it was calculated. Verification that the known-volume chambers were measuring air kerma accurately was done by taking measurements of radioactive sources and standard x-ray beams and comparing them to calibrated, NIST-traceable ionization chamber measurements.

Table 1. Correction factor descriptions and calculation method for the known-volume chambers.

| Correction factor | Description | Calculation method |
|---|--|--------------------|
| $\left(\frac{L}{\rho}\right)_{air}^{wall}$ | Spencer-Attix collision mass stopping power for the wall material to dry air | SPRRZnrc |
| $\left(\frac{\mu_{en}}{\rho}\right)_{wall}^{air}$ | Ratio of mass energy absorption coefficients averaged over the spectrum for dry air to the wall material | NIST values |
| k_h | Humidity correction | 0.997 |
| k_{wall} | Corrects for attenuation and scatter in the chamber wall | CAVSPHnrc |
| k_{an} | Corrects for axial nonuniformity due to the point source nature of the beam | Assumed to be 1 |
| k_{comp} | Corrects for nonuniform nature of the wall material | Assumed to be 1 |
| k | Any other corrections needed | |

Results: Through these imaging techniques, volumes of 3.55 cm³ and 3.40 cm³ were determined for the first and second chambers, respectively. The comparison of the imaging volumes to the volumes calculated from the air kerma calibration and physical measurement are shown in Table 2 and the uncertainty budget for the volumes is shown in Table 3.

Table 2. Comparison of imaging volumes to calibration and physical measurement

| | Imaging volume [cm ³] | Calibration volume [cm ³] | Volume by physical measurement [cm ³] | Within % of each other |
|---------------------------|-----------------------------------|---------------------------------------|---|------------------------|
| Chamber 1 (S/N: XR191680) | 3.55 ± 0.90% | 3.52 ± 1.5% | 3.53 | 0.85% |
| Chamber 2 (S/N: 256) | 3.40 ± 0.90% | 3.36 ± 1.5% | 3.37 | 1.20% |

Table 3. Uncertainty budget for the volumes of the ionization chambers

| Volume uncertainty | | | |
|----------------------------------|------------|----------------------|----------|
| Quantity | Type A (%) | Type B (%) | Comments |
| Resolution of CT | | 8.4×10 ⁻⁶ | 1 |
| ISO50 surface determination | | 0.89 | 2 |
| COMSOL electric field correction | | 0.13 | 3 |
| Magnification factor | | 0.04 | 4 |
| Standard Uncertainty (k=1) | | 0.90 | |
| Expanded Uncertainty (k=2) | | 1.80 | |

1. Resolution of CT is 50 μm. Rectangular distribution assumed.
2. Standard deviation of ISO50 value. Triangular distribution assumed and higher uncertainty between the two chambers used to be conservative.
3. Standard deviation of subtracted volumes due to the shape of the electric field. Rectangular distribution assumed and higher uncertainty between the two chambers used to be conservative.
4. Standard deviation from taking multiple caliper measurements of the phantom used to calculate the magnification factor. Rectangular distribution assumed.

Figure 3 shows the correction factors for standard, NIST-matched x-rays beams, Cs-137, and Co-60. Finally, the comparison of air kerma measurements with the standard M250 x-ray beam, Cs-137, and Co-60 measurements are shown in Table 4.

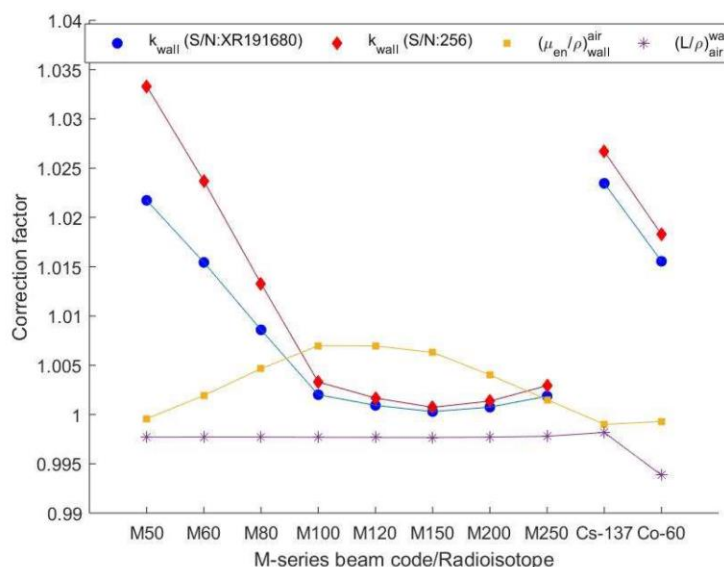


Figure 3. Correction factors for the known-volume chambers. The increase in the wall correction for Cs-137 and Co-60 is due to the introduction of a buildup cap.

Table 4. Comparisons of air kerma measured with the known-volume chambers to NIST-traceable, calibrated ionization chambers

| M250 x-ray beam | Chamber 1 S/N: XR191680 | Chamber 2 S/N: 256 | A3 S/N: XR022483 |
|-----------------------------|----------------------------|-----------------------|---------------------|
| Air kerma rate [mGy/s] | 1.642 | 1.644 | 1.634 |
| Percent difference from A3 | 0.50% | 0.63% | -- |
| Cs-137 | | | A12 S/N: XA060332 |
| Air kerma rate [mGy/s] | 0.1732 | 0.1733 | 0.1732 |
| Percent difference from A12 | 0.005% | 0.026% | -- |
| Co-60 | | | A12 S/N: XA060332 |
| Air kerma rate [mGy/s] | 16.79 | 16.76 | 16.83 |
| Percent difference from A12 | 0.23% | 0.43% | -- |

Conclusions and Significance: It has been shown that known-volume ionization chambers can be developed from commercial ionization chambers using micro-CT and common surface determination techniques with relatively low uncertainty. With the necessary correction factors, air kerma can be measured to an accuracy within the uncertainty of the volumes.

Relevance to CIRMS: This work is a portion of the doctoral work performed by the first author involving the development of absolute dosimeters. This work relates to the CIRMS mission as NIST maintains many primary standards for radiation measurement, including known-volume ionization chambers. The first author's goal is to become a clinical/academic medical physicist and currently works in a laboratory focused on metrology.

References

1. F. Borges de Oliveira et al., "Experimental investigation of surface determination process on multi-material components for dimensional computed tomography", *Case Studies in Nondestructive Testing and Evaluation*. 6, 93 – 103 (2016)
 2. C. K. Ross, "Comments on 'Ionization chamber volume determination and quality assurance using micro-CT imaging,'" *Phys. Med. Biol.* 54, 23– 27 (2009).
-

Towards primary and secondary standards for dosimetry in Flash radiotherapy

Alexandra Bourguoin, Andreas Schueller, and Ralf-Peter Kapsch

Physikalisch-Technische Bundesanstalt (PTB), Bundesallee 100, 38116 Braunschweig, Germany, alexandrabourguoin@cmail.carleton.ca

Objective: The development of code of practice (CoP) for new radiotherapy modalities are usually based on existing dosimetry protocols (AAPM TG51 or IAEA TRS-398) which are modified for the specificity of the modality. The Flash radiotherapy is a new modality in which the prescribed dose is delivered with ultra-high dose rate [1]. Although in the early stage of development, it has already shown advantage over treatments using conventional dose rate as the adverse dose effect on healthy tissue is reduced. The challenge with dosimetry for Flash modality is that the use of ionization chambers as secondary standards is not suitable due to high level of ion recombination, it can be larger than 50% [2]. In addition, the dependence of the ion recombination is not linear with the dose per pulse. To be obtained, it requires extensive measurements and intra-type variation between ionization chambers can be in the 2-5% range. The lack of precise accurate measurements and accurate theoretical model of the ion recombination hampers the progress of the Flash modality. The UHDPulse project is an EMPIR funded collaboration [3] to develop reliable dosimetry methods for Flash modality and guidance for CoPs.

Materials and Methods: The response of different types of detectors has been measured in an ultra-high dose per pulse 20 MeV electron beam provided by the research accelerator at PTB Braunschweig [4]. To monitor the beam, a non-destructive Integrating Current Transformer [5] (ICT) is integrated in the beamline. The detectors used are plane-parallel chambers (Advanced Markus, PPC40, PPC05), alanine pellets and a probe-type graphite calorimeter. The ion collection efficiency of ion chambers has been obtained for a range of 0.5 to 2 Gy-per-pulse.

Results: The dependence of the ion collection efficiency is not linear with the dose per pulse for all types of detectors and intra-type variations in the 2-5% range have been observed as illustrated in Figure 1. In Figure 2, the depth dose measurement with calorimeter and ion chamber compared to Monte-Carlo calculation is shown. The half-value depths in water R_{50} obtained from measurement and simulation agree within 1 mm.

Conclusions and Significance: Although the project is still in early stage, calorimetry is showing promising results for absorbed dose measurements both at National Metrological Institutes and in Clinics. Calorimetry gets simpler at Flash dose rate as the dose delivery is in a few seconds or less. The preliminary results show that advanced thermal insulation of the calorimeter is not required, nor the use of a heat lost correction factor. For relative measurement, also other types of dosimeters such as plastic scintillators, diodes, or diamond detectors are under investigation to determine the best option. In this presentation, preliminary results of the investigation of calorimeter and ionization chambers will be shown.

Relevance to CIRMS: Although at the early stage, Flash is a promising treatment modality which will need a standard for dosimetry. Also, the findings in this project, especially for ionometry, can be used for the development of CoPs for dosimetry at Intraoperative radiation therapy (IORT) which is already implemented in clinics.

Acknowledgement: This project 18HLT04 UHDpulse has received funding from the EMPIR programme co-financed by the Participating States and from the European Union's Horizon 2020 research and innovation programme.

References

1. V. Favaudon *et al.*, Ultrahigh dose-rate flash irradiation increases the differential response between normal and tumor tissue in mice, *Science Translational Medicine* 6 (2014), DOI: 10.1126/scitranslmed.3008973
2. K. Petersson *et al.*, High dose-per-pulse electron beam dosimetry - A model to correct for the ion recombination in the Advanced Markus ionization chamber. *Medical Physics*, 44(3), 1157–1167. DOI: 10.1002/mp.12111.
3. Schüller *et al.*, The European Joint Research Project UHDpulse – Metrology for Advanced Radiotherapy Using Particle Beams with Ultra-High Pulse Dose Rates. *Physica Medica*, vol. 80, Dec. 2020, pp. 134–50, DOI: 10.1016/j.ejmp.2020.09.020.
4. Schüller *et al.*, The Metrological Electron Accelerator Facility (MELAF) for Research in Dosimetry for Radiotherapy, *IFMBE Proceedings* 68 (2018) 589-593. DOI: 10.1007/978-981-10-9023-3_109
5. Schüller *et al.*, Traceable charge measurement of the pulses of a 27 MeV electron beam from a linear accelerator, *JINST* 12 (2017) P03003. DOI: 1088/1748-0221/12/03/P03003

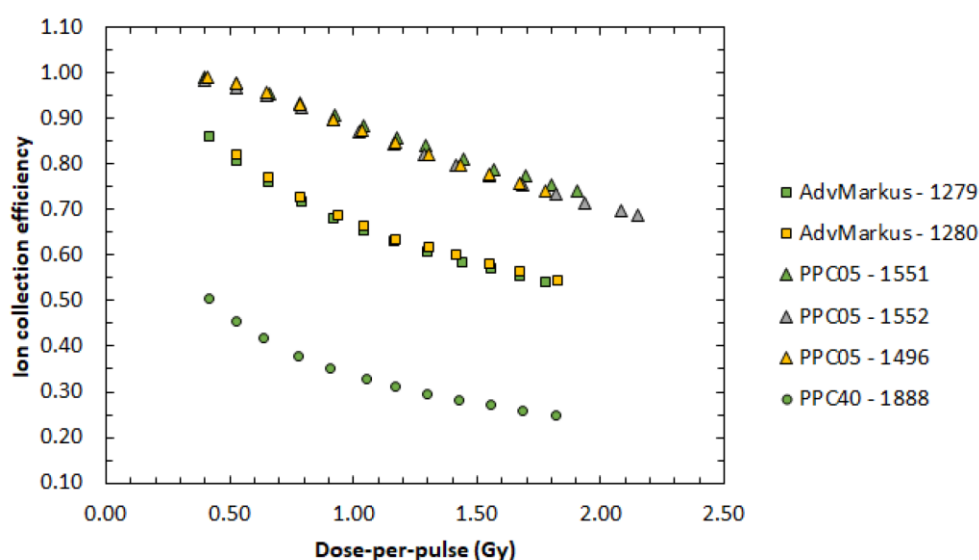


Figure 1. Ion collection efficiency in ultra-high dose per pulse electron beams

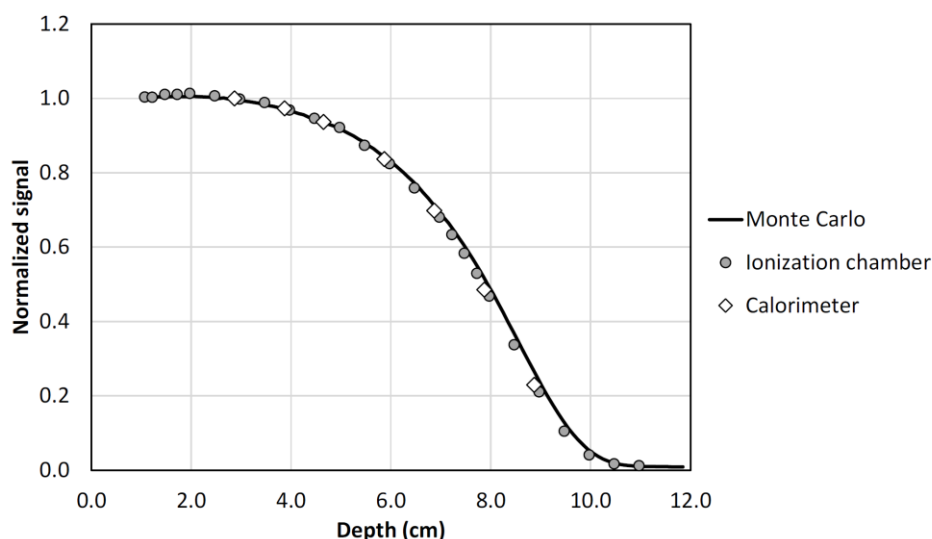


Figure 2. Depth dose measurement in water with calorimetry and ionometry compared to Monte Carlo simulation.

Tuesday, April 27, 2021

Medical Applications Subcommittee

Applications of plastic scintillation dosimetry for radiation oncology: A startup founder perspective

François Therriault-Proulx

Medscint, Quebec City, QC, Canada, francois.tp@medscint.com

Plastic scintillation detectors were shown to be useful for multiple applications in radiation oncology research since the first pioneer work in the field during the late 80s. With their water equivalence and energy independence over 100 keV, small size, real-time and multi-point capability, robustness to radiation damage, angular independence, independence to magnetic field, and linearity over a wide dynamic range of dose rates, plastic scintillation detectors show great promises from both a research and clinical perspective. External beam radiation therapy using linear accelerators (photons and electrons), brachytherapy (HDR and LDR), proton therapy, FLASH radiation therapy and stereotactic radiosurgery are among the radiation therapy modalities that can benefit from plastic scintillation detectors. Veterinary radiation oncology and pre-clinical cell and animal studies are also gaining interest for this technology. Potential applications range from fundamental research to machine QA and treatment plan verification, to real-time *in vivo* measurements. With the number of publications involving scintillation detectors rising rapidly, and first products becoming commercially available, it is fair to state that scintillation dosimetry in radiation oncology is entering a new era. In this presentation, the CEO and co-founder of Medscint Inc. (Quebec City, QC, Canada) will share his experience going from PhD to entrepreneur in this field and discuss with the audience his vision about the challenges that were overcome in the last decades, and where he sees the field moving forward from both an academic and commercial perspective.

Evaluation of proton dose accuracy improvements with dual-energy CT

Sina Mossahebi^{1,2}, Pouya Sabouri³, Maida Ranjbar⁴, Joshua Strauss⁵, Matthew O'Neil⁶, Jainil Shah⁷, Jerimy C. Polf^{1,2}

¹University of Maryland School of Medicine, Baltimore, MD, sinamossahebi@umm.edu

²Maryland Proton Treatment Center, Baltimore, MD

³Miami Cancer Institute, Miami, FL

⁴University of Maryland-Baltimore County, Baltimore, MD

⁵Vanderbilt University, Nashville, TN

⁶Associates in Medical Physics, Lanham, MD

⁷Siemens Healthineers, Cary, NC

Purpose: Uncertainties in stopping-power ratio (SPR) limit plan robustness in proton therapy. A main part of these uncertainties arises from limitations in the clinically accepted method for SPR calculation using single-energy CT (SECT) calibration curves. This study investigates the potential improvements in proton dose calculation accuracy using dual-energy CT (DECT) scans of biological and non-biological samples.

Methods: SECT and DECT scans of 11 animal tissue samples consisting of sheep-lung, cow-lung, cow-liver, cow-brain, pork-liver, and pork-foot were acquired on a Siemens SOMATOM Definition Edge CT scanner. Similarly, DECT and SECT scans for 18 non-biological tissue surrogate plugs and 3 breast implants were acquired. SPR images were constructed from relative electron densities and effective atomic numbers generated by DECT scans. For each sample, the SECT and DECT calculated SPR values were compared with multi-layer ionization chamber measurements. Treatment plans with identical objectives were optimized and recalculated on each image set. Plans were delivered and point dose comparisons and planar dose 2D gamma analysis (3%/3mm) were performed for TPS calculated dose distributions on both scans.

Results: For all lung tissue samples, DECT-derived SPR values agreed with the measurements within $\pm 8\%$ for sheep and 0.54% for cow compared to 38% from SECT. For the pork-foot, SPR measurement was within 1% agreement with DECT-calculated values in comparison to 7% difference for SECT. However, no relevant difference was observed for other biological tissue. For non-biological tissue samples, DECT-calculated SPRs were within 3% agreement of the measurement, while SECT computed values deviated by as much as 15%. Higher gamma-passing rates were consistently obtained when using DECT images for all plugs and breast implants.

Conclusion: Our study suggests that DECT can improve the accuracy of SPR predictions for biological and non-biological tissues. The utilization of DECT in proton therapy can lead to significant reduction of range uncertainties.

Challenges in multi-center quantitative imaging for TRT dosimetry

Eric C. Frey

Radiopharmaceutical Imaging and Dosimetry, LLC and Johns Hopkins University Department of Radiology, efrey@jhmi.edu

Targeted radiopharmaceutical therapy TRT for cancer, and especially using alpha particle emitting radionuclides is a promising and rapidly developing modality. TRT has the advantage that it is lethal and thus immune to resistance mechanisms. In addition, knowledge of the micro- and macroscopic effects of radiation on tumors and normal combined with the ability to image the *in vivo* distribution of the TRT via nuclear medicine imaging methods provides the potential for therapy planning using dosimetry. Regulatory approval of TRT agents and clinical adoption of dosimetry-based treatment planning require multi-center clinical trials. Numerous clinical trials of different agents using a variety of radionuclides are currently under way and in various stages of planning. Standardization and harmonization of quantitative imaging and dosimetry of these TRTs across multiple sites often involving different imaging systems and dose meters from a variety of manufacturers, are essential for successful trials. Often, the radionuclides used are novel, and standard methods and settings for activity measurement using clinical dose meters are not available. Similarly, methods for quantitative reconstruction of images of these radionuclides are not available from system manufacturers, and methods provided with the scanners give rise to inaccurate estimates of the activity distributions with site-to-site and patient-to-patient variations in accuracy. These variations give rise to variability in the values of dosimetric quantities and can obscure dose-response relationships. This talk will review the requirements for dosimetry of TRTs, with a focus on quantitative single-photon emission computed tomography of the radionuclides commonly used in TRT. It will present data indicating the need for measures for standardizing and harmonizing this quantitative imaging across multiple centers having imaging systems from different camera manufacturers.

Industrial Applications Subcommittee

Current solutions and needs in dosimetry for radiation processing applications

Mike Pageau

GEX Corporation, mpageau@gexcorp.com

The presentation examines the commercial dosimetry systems in use around the world and the needs of the industries that use them in irradiation applications including medical device sterilization, decontamination in food and pharmaceutical packaging, food irradiation, phytosanitary irradiation of fruits and vegetables, blood irradiation, polymer modification, and more.

Chip-scale, integrated photonics for radiation dosimetry and calorimetry

Nikolai N. Klimov, Zeeshan Ahmed, Ileana M. Pazos, Lonnie T. Cumberland, Fred Bateman, Ronald E. Tosh, and Ryan Fitzgerald

National Institute of Standards and Technology, Gaithersburg, MD, nikolai.klimov@nist.gov

The last few decades have witnessed an exponential growth in photonics, driven in part by improvements in micro-electronics fabrication techniques and by increasing adoption of photonics components by the telecommunications industry. One potential application of photonic sensors is ionizing radiation dosimetry. At present, primary standards for absorbed dose are based on large (m^3) water calorimeters used to link the absorbed energy from a large uniform radiation beam to the temperature rise in a $\sim 0.5\text{-mm}$ sized thermistor probe. The realization of this standard requires radiation-beam uniformity on the order of centimeters. On the other hand, rapidly evolving medical and industrial applications involving less-uniform fields would greatly benefit from a deployable solution capable of resolving absorbed dose with millimeter to micrometer precision. To address this need, the National Institute of Standards and Technology (NIST) has recently started a program to develop nanofabricated absolute and relative dosimetry devices that will leverage nano-photonics and frequency metrology to provide a field-deployable solution with micrometer-scale spatial resolution. Our radiation sensors are based on high-Q silicon photonic resonators such as ring resonators and photonic crystal cavities. We have recently demonstrated that these sensors can withstand 1 MGy absorbed dose in ca. 1 MeV gamma-irradiations with negligible degradation of device performance. In this presentation we will give an overview of the NIST photonic dosimetry program and its most recent developments. We will explain design, nanofabrication, packaging, and interrogation of our devices. We will also show our preliminary results on real-time photonic calorimetry measurements in on/off cycles of the electron beam provided by a Van de Graaff accelerator at nominal dose rate of kGy/min. Comparison of the device response with the output of finite-element modelling of heat transport and dose measurements obtained by co-irradiated alanine pellets (analysed via EPR) will also be discussed.

Recent advances towards a deployable emergency response dosimetry system (ERDS)

Jason Campbell

National Institute of Standards and Technology, Gaithersburg, MD, jason.campbell@nist.gov

This presentation will discuss the NIST's recent efforts to realize a deployable emergency response dosimetry system which has been designed to augment the triage process in the aftermath of a no-notice mass exposure nuclear event. The ERDS system is designed to sort large populations by using an electron spin resonance-based 'reader' to rapidly measure the received dose in dosimetric materials embedded in ubiquitous artifacts (government issued ID cards). The 'reader' is composed of custom designed permanent magnets, a non-resonant transmission line ID card probe, and a highly sensitive microwave interferometric detection scheme. This approach leads to environmentally robust deployable system capable of rapid self-discrimination at the $2 \text{ Gy} \pm 0.5 \text{ Gy}$ level.

Radiation Safety and Security Subcommittee

Performance testing samples in radioactivity analysis: What they are and how to choose the appropriate ones

Evgeny Taskaev

Eckert & Ziegler Analytics, Inc., 1380 Seaboard Industrial Blvd., Atlanta, GA 30318,
evgeny.taskaev@ezag.com

Current regulatory environment (ISO 17025, 17034, 17043, MARLAP etc.) and good laboratory practices require Radioanalytical Laboratories to develop or select appropriate analytical methods, verify and validate them, and establish metrological traceability. All mentioned activities will require the use of Reference Materials (RM), Calibration standards, Laboratory QC samples, Daily Check Sources for the instrument's checks, etc. These also will require participation in Proficiency Testing (PT) programs and performing analysis of PT Samples.

ISO standards 17034 and 17043 describe in generic terms requirements for Reference Material (RM) producers and implementation of PT programs respectively. Laboratory input in transforming generic standard requirements to specific actions is critical. Defining traceability requirements and sources' metrological parameters can be especially challenging. Development of laboratory emergency response capabilities adds even more requirements to the PT plans.

In the past, vast majority of RMs were produced by the National Metrological Institutions (NMI) like NIST, NPL, PTP etc. Last decade the capability of the NMI to produce RMs, substantially diminished, leaving the users with limited choices.

Eckert & Ziegler Analytics, Inc. (EZA) is an established commercial provider of calibration standards, PT schemes and samples, RMs for radioactivity analysis. To address demand and reduce manufacturing costs, we started shifting from preparation of "traditional" RM towards lab/project specific, highly commutable (fit for purpose) RM/PT samples. This includes concept of whole sample use, where RM or PT sample will be used as "a whole" without subsampling or division.

Each source (PT sample/Reference Material) can be characterized by four major parameters: activity concentration with stated uncertainty, homogeneity of activity distribution, stability of the parameters over time, and commutability. Commutability is less known parameter and it reflects suitability of the source/material for the intended use in the analytical process. In general, the tighter the parameters (lower uncertainty, better homogeneity, etc.) the higher cost of manufacturing can be expected.

It is essential that participating laboratory thoroughly evaluates their needs for RM/PT and gets involved in the design of the RM/PT samples and schemes, helping optimize parameters and cost. After all it is the laboratory responsibility to design appropriate PT program, that satisfy regulatory and accreditation bodies.

Some examples of specific PT samples are discussed.

A new technology that will help radiation labs be more productive and safer

Robert L. Jones, Olga Piraner, and Ge Xiao

Centers for Disease Control and Prevention, Atlanta, GA 30341, RLJ0@cdc.gov

After a national radiological or nuclear incident, CDC may have tens to hundreds of thousands of clinical samples to rapidly analyze to enable a dose assessment for medical management or follow-up. If the incident involved Sr-90 for example, this would require extensive staff involvement with vacuum box extraction of the Sr-90 for Liquid Scintillation Counting (LSC). This is a very labor-intensive process involving the use of concentrated acids. For over 15 years, CDC has been looking for an alternative to the pre-analytical vacuum box system to eliminate the extensive manual labor process (automation) and a safer environment versus using concentrated acids with a vacuum box for a response that may last for weeks or months requiring 24/7 sample processing.

The “organic” analytical laboratories at CDC have been using pre-analytical processing systems for over 20 years. In talking to these vendors and stating our needs for the use of concentrated acids, they have told us for years that their systems cannot handle or use acids (dilute or concentrated).

About three years ago a company that produces autosamplers for ICP-MS systems informed us that they had a system that could be used for the pre-analytical processing using concentrated acids. We were able to acquire a custom-made system, and the system worked well with the exception of the throughput due to a single sample introduction probe. Upon discussion with the equipment manufacturer they were able to design and we acquired a “five” probe system that significantly increased throughput. In addition, we found that we could use the Sr-90 extraction “resin” (e.g. custom DGA columns) multiple times versus a onetime use of Sr resin cartridges with the vacuum box system.

We also found that the system is safer for the lab staff as acids are contained in bottles and all bottles are in a secondary containment system in a closed cabinet.

This system has been developed for both Sr-90 and Pu-239, we are in the development of a Np-237 method, and this will be applied to other radionuclide analytical methods requiring a vacuum box extraction system.

We will also report our recent improvements, new methods, new technologies incorporated and future plans for CDC’s Rapid Radionuclide Screen (bioassay) for responding to a major radiological or nuclear incident to assess the public’s radiation dose for medical management decisions.

Disclaimer: The findings and conclusions in this study are those of the authors and do not necessarily represent the views of the U.S. Department of Health and Human Services or the Centers for Disease Control and Prevention. Use of trade names and commercial sources is for identification only and does not constitute endorsement by the U.S. Department of Health and Human Services or the Centers for Disease Control and Prevention. The authors declare that they have no competing financial interest.

Additional Abstracts

Proffered Abstracts from 2020 Meeting (canceled due to COVID-19 pandemic)

Measurement and modeling of the radioactivity of neutron-irradiated jade

Richard A. Livingston¹ and Heather Chen-Mayer²

¹*Materials Science & Engineering Dept, University of Maryland, College Park, MD,
rliving1@umd.edu*

²*Materials Measurement Laboratory, National Institute of Standards and Technology,
Gaithersburg, MD*

Prompt gamma neutron activation (PGAA) is a promising method for elemental analysis of jade artefacts. However, museum curators are hesitant to apply it to their collections because of concern over neutron-induced radioactivity that could impose restrictions on their post-irradiation public display or storage. To evaluate the extent of this problem, residual activities from some representative samples of nephrite jade after standard PGAA measurement were analyzed. These samples included three geological specimens from different regions in Asia and one from Wyoming. Their gamma ray activities were measured three times: before irradiation, immediately after irradiation and 110 days after irradiation. Only the Wyoming sample had detectable pre-irradiation activity, $19 \text{ Bq} \pm 18 \text{ Bq}$ due to ^{235}U . Radionuclides detected immediately post-irradiation included: ^{24}Na , ^{27}Mg , ^{28}Al , ^{49}Ca and ^{56}Mn . By 110 days these short-lived radionuclides had died away and the gamma spectrum showed peaks for ^{46}Sc , ^{51}Cr , ^{59}Fe , ^{60}Co and ^{65}Zn . The presence of Sc and Co was unexpected since these elements have not typically been included in conventional analyses of nephrite composition. However they dominated the total activity, which at 110 days ranged from $12 \text{ Bq} \pm 22 \text{ Bq}$ to $2,906 \text{ Bq} \pm 117 \text{ Bq}$. The activities were certified as “exempt quantities” by Health Physics, and the samples have been returned to their owners. The future decay of the activity over time was modeled for the three and after 5-6 years only the ^{60}Co (half-life 5.27 yr) activity was significant. To put this into perspective for the curator, it can be compared with the natural radioactivity of ^{40}K (half-life $1.25 \times 10^9 \text{ yr}$) of porcelain objects. The specific activity of porcelain is about 0.045 Bq/g . Consequently, the activity of the Wyoming sample after 5 years equals about 4.8 kg of porcelain which is approximately the mass of one medium size vase.

Characterization and inter-calibration of laboratory irradiation sources used for multiple solid-state dosimetry modalities

Ryan O'Mara and Robert Hayes

North Carolina State University, Raleigh NC, rbhayes@ncsu.edu

In response to an increasingly nuclearized world, more efforts should be devoted to the development of technologies that can ensure reliable, low-impact monitoring of nuclear activities. Solid-state, retrospective dosimetry has the ability to record the historical radiation environments of materials long after the radiological source material has been removed. This capability is becoming increasingly more attractive as nuclear technology is becoming more ubiquitous around the world. In general, luminescence dosimetry methods have been applied to inorganic insulating materials while electron spin resonance dosimetry has found applicability in organic materials. The benefit of having a standard for comparison between these modalities is assumed to be understood. This work demonstrated intercalibration between independent systems made traceable to various national metrology institutes. These systems consisted of a commercial OSLD medical physics reader by Landauer, a DTU thermoluminescence and optically stimulated luminescence reader and a Bruker EPR spectrometer using alanine pellets. Measuring each system's calibrated responses relative to the other systems in an inter-comparison enables reliable cross measurement sufficient for quality retrospective dosimetry applications.

Proficiency testing for interlaboratory comparison of dosimetry systems

Sandra Eva Pawlak, Diego Martin, Pablo Salatino, Ailin Carreon, Juan Garrido

Comisión Nacional de Energía Atómica (CNEA)- Avda. Del Libertador 8250 (C1429BNP) CABA, Argentina, pawlak@cae.cnea.gov.ar

Introduction: An interlaboratory comparisons with the requirements of ISO / IEC 17043:2010, have been planned to carry out a set of activities whose provision, also align give opportunity for participants to demonstrate their technical competence and ensure, as far as the scope of these arrive, the quality and traceability of their measurements.

Purpose: Give participants the opportunity to demonstrate their competence and help to identify problems (if any) related to the performance of personnel, equipment calibration and adequacy of methods.

This exercise is developed to evaluate two aspects:

Part 1: The ability of participants to meet pre-set dose values (target dose).

Part 2: The ability of the participants to measure doses actually applied.

Parameter to measure:

The test items are alanine dosimeters irradiated only with gamma radiation.

Part 1: The parameter to be determined is the dose delivered to the dosimeters.

The items were irradiated at: 1 kGy, 5 kGy, 10 kGy, 25 kGy.

Part 2: The parameter to be determined is the dose measured by each participant.

Conclusions:

Part 1: Parameter z: Of the results obtained in the statistical treatment, it is observed that the performance of the participants has been very good. No unacceptable results were obtained.

Part 2: Parameter En: From the results obtained in the statistical treatment it was observed that the uncertainty value of some participants should be reviewed. Some of the reported uncertainty values are lower than the reference laboratory.

Development of a fast neutron spectroscopic/imaging system using a Ga₂O₃-based scintillator

Noel A. Guardala¹, Stanley D. Hunter², J. Derek Demaree³, Marko Tjader⁴

¹*George Washington University, Washington D.C., nguardala76@gwu.edu*

²*NASA/GSFC, Greenbelt MD*

³*Army Research Laboratory, Aberdeen, MD*

⁴*Naval Research Laboratory, Washington D.C.*

We have performed a number of preliminary measurements related to the basic response of n-doped Ga₂O₃ (provided by NRL) in scintillator mode to a variety of ionizing radiation sources including Spontaneous Fission neutrons from both ²⁵²Cf source, and Depleted Uranium, DU and 14.3 MeV neutrons from a D-T neutron generator Using the NRL grown Ga₂O₃ characteristic spectra using a very simple detector arrangement with four rectangular crystals each 600 microns thick were obtained. Based on these results it is proposed that n-doped Ga₂O₃ can be effectively used in systems designed to be either fast neutron spectrometers or Omni-Directional fast neutron imagers. These crystals were also found to be insensitive to gamma radiation for photons with energies greater than 40 keV. Potential applications for both the spectroscopic and imaging systems will be discussed as they pertain to a number of conditions where fast neutrons are emitted.

Development of advanced materials for the extraction of uranium from seawater

Mohamad Al-Sheikhly

*Department of Materials Science and Engineering, University of Maryland, College Park, MD,
mohamad@umd.edu*

The amount of dissolved uranium in seawater far exceeds the amount available in terrestrial ores. In addition to contributing additional uranium to the nuclear fuel cycle, retrieving uranium from seawater greatly reduces the technological complexity and environmental impact associated with conventional uranium mining and milling. Although several methods of extraction have been developed and tested over the past several decades, significant interest has been generated in developing adsorbent fabrics using radiation-induced polymerization after over a kilogram of uranium was obtained by Japanese groups using similar methods. Despite their success, a need remains to develop more efficient adsorbents to make this technology commercially viable.

Advanced adsorbent materials are being developed using polymeric substrates with high chemical stability, excellent degradation resistance and improved mechanical properties. Fabrics include polypropylene, nylon and advanced Winged Fibers™ from Allasso industries featuring extremely high surface areas for improved grafting density. Using the University of Maryland's 100 kCi Co-60 gamma source and 1-10 MeV electron beam linear accelerator, the various fabrics have been irradiated over a wide range of dose rates, total doses and temperatures and subsequently analyzed with EPR for determination of free radical concentration.

Also being utilized are innovative vinyl phosphonate monomers with high distribution coefficients and selectivity for uranium with excellent potential for free radical polymerization. Optimization of the grafting procedure involves precise control over reaction temperature, duration and methodology. Attachment of the chelating adsorbent to the substrate polymer is maximized by use of high monomer concentrations and quantified by determination of the grafting density of the sample. Grafted samples are subsequently analyzed for uranium adsorption with ICP-AES. Preliminary results with the new adsorbent fabrics have yielded grafting densities up to 54% with high fractions of uranium removed from solution with significant potential for improvement. These results were obtained with real ocean water doped with approximately 10 mg/L uranium introduced in the form of uranyl acetate.

Current work includes optimization of irradiation conditions in addition to material characterization on the molecular level and analysis of the sample microstructure. Further testing in real seawater will be conducted to compare the selectivity of the adsorbent fabric towards uranium compared to that of other species, in addition to determining the loading and adsorption rates under various conditions such as pH, temperature and salt concentration. Experiments in seawater will also be performed to characterize the effects of organics on the adsorbent materials, test for durability and reusability and determine kinetics and efficiency of the uranium extraction as a function of the time of exposure to seawater in order to study the degradation of the sorbent in realistic environments.

Performance of 2nd-generation FNTD reader in neutron-dose measurements

V. Fomenko¹, J. Harrison¹, M. Moscatel², M. Kirr², M. Akselrod¹

¹Landauer, Division of Fluke Health Solutions, Stillwater, OK, vfomenko@landauer.com

²Landauer, Division of Fluke Health Solutions, Glenwood, IL

Neutron dosimeters based on the Fluorescence Nuclear Track Detector (FNTD) technology, have repeatedly demonstrated good metrological performance [1]. Commercially available FNTD readers are based on the principle of confocal laser-scanning fluorescent microscopy.

Recently, a prototype of 2nd generation FNTD reader, utilizing laser line excitation and parallel multipixel fluorescence readout has been developed. The instrument demonstrated an improved image quality and a 30-time increase in the readout speed, compared to the speed of the 1st generation commercial FNTD reader. The fluorescent imaging of 32 mm² FNTD area takes about 3 min and provides the sensitivity of 21 tracks/mm²/mSv for the Am-Be neutrons.

Two types of FNTD packages have been used for the presented tests: large-area dosimeters with area per converter of 21 mm² and the standard Radwatch dosimeters providing 8.2 mm² of the detector area under a polyethylene converter. The dosimeters in both configurations have been irradiated either to only Am-Be fast neutrons or to Am-Be fast neutrons with M30 X-ray photons.

The neutron dose readout results were compliant with the ISO-14146 standard (2017-08-09 draft), as presented below.

References

1) M. Akselrod and J. Kouwenberg, *Fluorescent nuclear track detectors - Review of past, present and future of the technology*, Radiat. Meas. (2018) **117** 35-51

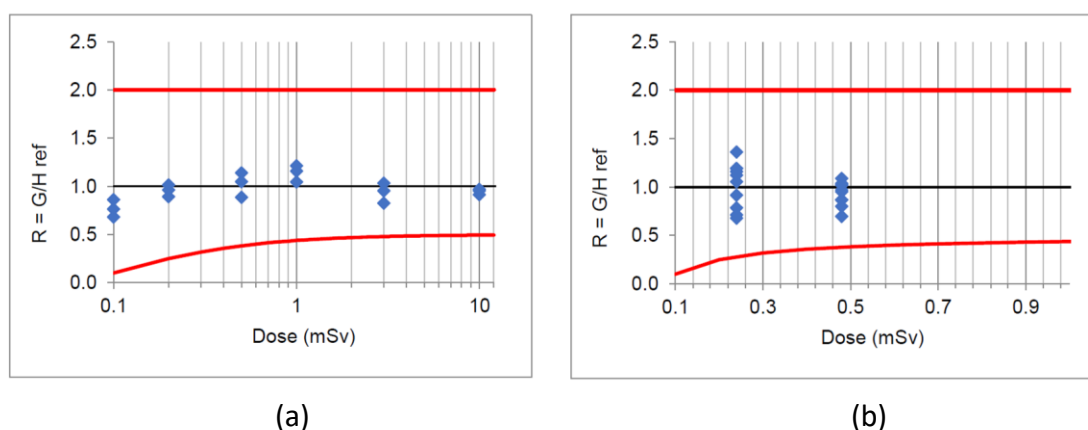


Figure 1. Normalized response of FNTDs to delivered Am-Be neutron dose measured with the new reader: (a) calibration measurements with large-area detectors; (b) Blind test results after mixed neutron and M30 photon dose irradiations of FNTDs in standard packages. Red lines correspond to the performance limits of ISO-14146.

Space-based ionosonde receiver and visible limb-viewing airglow sensor (SIRVLAS): A CubeSat instrument suite for enhanced ionospheric charge density measurements

Sujay Swain, Benjamin Cohen, Ryan He

Math Science and Computer Science Program, Montgomery Blair High School, Silver Spring, MD,
sujay.swain@blair3sat.com

blair3sat is a high school student-run 501(c)(3) organization based in Montgomery County, Maryland. blair3sat works to engage students in Montgomery County to participate in STEM by solving real world problems in the aerospace industry. blair3sat is currently developing an instrument suite for the mapping of atmospheric electron density through the correlation of optical and radio frequency instrumentation. The satellite will include the instrument suite SIRVLAS, which contains two instruments, an optical instrument and an RF instrument. The objective of the mission is to prove that instruments like SIRVLAS can generate a three-dimensional mapping of ionospheric electron density. The optical instrument will measure 1380 nm, 2700 nm, and 844.6 nm emissions in the lower ionosphere. Because 844.6 nm is emitted from the radiative recombination reaction of O^+ and e^- , local electron densities may be calculated. These electron densities will be used as a reference for the data processing of RF signals. Specifically, correlation is done through constrained optimization of known ray-tracing PDEs. The measurements of 2700 nm and 1380 nm will both be used for the absorption spectroscopy of CO_2 and H_2O concentrations. The optical instrumentation will be a set of three similar compartments. Each compartment will use a small aperture for focusing and lowering the FOV for higher spatial sensitivity. The compartments will also contain a set of high pass and bandpass filters to home in on the specific wavelength being measured. Lastly, there will be a set of focusing optics to send the light into a photodiode detector array. Measurements of electron density in the ionosphere allow for a better understanding of many radio applications, including radar and missile tracking. Correlating greenhouse gas concentrations with these mappings allows for the validation of models such as the HACCM model.

The primary standard for neutron emission rate at the National Research Council Canada

John Paul Archambault

National Research Council Canada, Ottawa, ON, JohnPaul.Archambault@nrc-cnrc.gc.ca

The absolute emission rate of neutron sources is an important quantity required in the calibration of neutron detectors used for radiation protection purposes. The National Research Council of Canada (NRC) has recently re-established the capability to determine emission rates for Canada. The approach taken, which is similar to other National Metrology Institutes, is based on the manganese bath system and considered a primary standard for determining absolute emission rate. The manganese bath at the NRC consists of a large spherical chamber filled with a manganese sulfate solution. A radio-nuclide neutron source is placed at the center of the chamber and the emitted neutrons are thermalized by the water in the solution with approximately half eventually captured by the manganese. The capture of a neutron leads to an excited state of manganese which decays by the release of an 847 keV gamma-ray. Detection of the characteristic gamma-ray and subsequent determination of the amount of activated manganese in the bath from neutron capture can be related through established methods to the emission rate of the neutron source. Care must be taken to account for neutrons that escape the bath or that get absorbed by other components of the manganese sulfate. The manganese bath system at the NRC will be described, the method used to estimate neutron losses presented and a description of the calibration of the gamma detector given. Finally, results of recent measurements of the emission rate of three americium-beryllium sources and one californium-252 source will be presented.

Equivalency of an X-Ray and a ^{137}Cs irradiator - It's more than just comparing energy spectra

Mark K. Murphy¹ and Jacob Kamen²

¹*Pacific Northwest National Laboratory, Richland, WA, mark.murphy@pnnl.gov*

²*Mount Sinai Hospital, New York, NY*

Irradiators utilizing radioactive cesium-137 (^{137}Cs) or cobalt-60 (^{60}Co) gamma-ray sources have been used for biological applications for many decades. This includes the irradiation of much of the nation's blood supply, and radiation biology research. Today there are increased security requirements for these devices, such as constant surveillance, controlled access, and personnel background checks. As a result, organizations considering purchasing a gamma-ray irradiator for the first time, or to replace an existing one due to radioactive decay, are now looking into alternative technologies -- the main alternative being an X-ray irradiator. To make an educated decision on whether a particular type of X-ray irradiator is of sufficient equivalency to a particular type of ^{137}Cs irradiator for specific, one has to rely on relevant published comparison studies from other researchers, or perform the comparison studies on their own. This presentation focuses on the comparison of the radiation physics aspects of two ^{137}Cs irradiator models and three X-ray irradiator models, for the purpose of determining whether the X-ray irradiator models could validly replace the ^{137}Cs irradiator models for certain applications. Our test results indicate that, depending upon the user's dose uncertainty budget and maximum areal density of specimens to be irradiated, the Model RS2000 160 kVp X-ray irradiator, Model XRAD-160 X-ray irradiator, or Model XRAD-320 X-ray irradiator, could successfully replace a ^{137}Cs irradiator. Results also reveal that differences in inherent source geometry, field geometry and irradiation geometry can possibly improve equivalency. It is hoped that this publication can be used as a guide for those considering transitioning to an X-ray irradiator.

Contributions to commissioning of proton centers with new modes of delivery techniques

Gonzalo F. Garcia-Fernandez¹, Roberto Garcí-a-Baonza¹, Eduardo Gallego¹, Alejandro Carabe-Fernandez², Alejandro Bertolet², Jose-Maria Gomez-Ros³, Hector Rene Vega-Carrillo⁴, Karen Arlet Guzmán García⁴, Lenin Estuardo Cevallos-Robalino⁵

¹*Polytechnic University of Madrid, Madrid, Spain, gf.garcia@upm.es*

²*Hospital of the University of Pennsylvania, Department of Radiation Oncology, Philadelphia, PA*

³*Ciemat, Radiation Dosimetry Unit, Madrid, Spain*

⁴*Autonomous University of Zacatecas, Academic Unit of Nuclear Studies, Zacatecas, Mexico*

⁵*Polytechnic University Salesian, Radiation Protection and Nuclear Systems, Guayaquil, Ecuador*

There is great expectation in the new techniques of treatment with protons, such as arc-therapy, flash-therapy or minibeam-therapy, among others, which are in the development and experimentation phase. From the point of view of commissioning and radiation protection, it is necessary to study the fields of dispersed radiation generated with these new modalities, mostly neutrons and gamma radiation, with the aim of implementing operational measures and adequate shielding designs from the early phases of construction of new centers. This is also important in adapting existing proton therapy centers so that they can apply the new proton delivery techniques safely.

The aim of this work was to design the operational radiological protection in proton therapy centers starting with the shielding design and selecting the radiation detection devices and the REM-meters for high energy neutrons, as well as its location in the center, to develop the radiological monitoring of the area, with full guarantee and compliance of the limits of doses for professionals, clinical staff and the general public. Several models of the radiation sources and materials of the facility were simulated, starting from a conservative assumption, followed by more realistic models.

Evenly, the neutron fields and spectra present in the installation were characterized by selecting the most appropriate radiation measurement device in each location.

This work is part of Contributions to Shielding and Dosimetry of Neutrons in CPTC, a multinational project developed by researchers from USA, Mexico, Ecuador, Peru and Spain, with the objective of implementing new proton centers in South American countries.

Validating $^{48}\text{VO}(\text{acac})_2$ synthesis through *in vivo* and *in vitro* studies

Brittany A. Broder¹, Mohammed P. Bhuiyan¹, Hannah J. Zhang², Richard Freifelder¹, Hsiu-Ming Tsai², Anna Kucharski¹, Lara Leoni¹, Samuel Mitchell¹, Darwin Boder¹, Chien-Min Kao², Chin-Tu Chen¹

¹University of Chicago, Chicago, IL, bbroder@uchicago.edu

²Department of Radiology, University of Chicago, Chicago, IL

Objective: ^{48}V -labeled vanadyl (VO_2^+) chelate bis(acetylacetonato) oxovanadium(IV) ($\text{VO}(\text{acac})_2$) is a promising new dual-modality radiotracer for cancer detection: previous research has shown it has enhanced uptake in tumor in magnetic resonance imaging (MRI) [1] and that it enhances cancer detection in positron emission tomography (PET) by increasing ^{18}F -deoxyglucose uptake [2]. However, assessing this compound is challenging – standard radiotracer purity tests such as high-performance liquid chromatography and thin-layer chromatography have been inconclusive, even for the cold compound or standard. Traditional methods of assessing cold $\text{VO}(\text{acac})_2$ in bulk quantities rely on visual analysis, which is infeasible with the femtogram quantity of compound present in tracer synthesis, or carbon-hydrogen-nitrogen (CHN) and inductively coupled plasma (ICP) mass spectrometry analysis, which cannot be performed with a radioactive compound. In this work, we investigate a methodology for validating the integrity of this compound in terms of isotopic purity, chemical composition, and uptakes and kinetics in *in vitro* and *in vivo* studies.

Materials and Methods: Natural titanium foils were bombarded via the $^{nat}\text{Ti}(\text{p},\text{n})^{48}\text{V}$ reaction at 40 μA in an 18 MeV IBA cyclotron and left to decay to mitigate short-lived isotopes. The target was dissolved and prepared as $^{48}\text{VO}(\text{acac})_2$ in a series of radiochemical steps [3-5]. The compound was reconstituted in dimethyl sulfoxide to prepare the dose for cell and animal studies. It was then analyzed via gamma-ray spectrometry and half-life assessment to confirm isotopic purity. In a separate synthesis, bulk chemistry was done to confirm the validity of the last step of the synthesis [5] and analyzed offsite with CHN and ICP analysis to confirm that the compound was produced. HCA-7 cells were grown in McCoy's 54 medium with 10% FBS (fetal bovine serum). For *in vitro* experiments, 28 dishes were plated with 5×10^5 cells each and incubated in 0 to 8 μCi of ^{48}V - $\text{VO}(\text{acac})_2$ solution at 37 °C for 2 hours, washed, and assayed via gamma-ray spectrometry. For *in vivo* studies, athymic nude mice were inoculated with $1 - 5 \times 10^6$ HCA-7 cells and tumors allowed to grow to 90-2300 mm^3 . For imaging, mice were injected with 20-90 μCi of tracer in 50% DMSO and 50% saline and imaged for 4 hours via Molecubes microPET/CT. After imaging and sacrifice, tumor and muscle tissues were excised and analyzed via gamma ray spectrometry. Uptake data was compiled into kinetic uptake curves for tissues of interest for each animal and compared to previously known uptake dynamics.

Results: 87 hours of irradiation yielded 31.6 mCi. The yield after radiochemical synthesis was 1.49 mCi, corresponding to 17% with decay corrections. The energy spectrum from the sample is shown in Figure 1. With a scale factor of 2.15, the three marked peaks correspond approximately to the energies expected of ^{48}V : 511 keV, 984 keV, and 1312 keV [6]. Results from ICP and CHN analysis of the last step of the synthesis are shown in Table 1. The small percent differences (within 1%) indicate the last step produces the desired compound. A cell uptake curve for the compound with HCA-7 cells is shown in Figure 2. The plateau after 4 μCi

indicates the maximum activity that can enter the cell is below 4 μCi . An uptake curve of one mouse image is shown in Figure 3. The uptake in tumor is approximately 1% throughout the duration of the scan, increasing marginally around 2 hours. This is distinguishably higher than muscle tissue from the opposing leg.

Conclusions and Significance: In the synthesis phase, the correct isotope appears to have been produced: Figure 1 shows energy peaks characteristic of ^{48}V . However, it is difficult to conclude if the correct compound is produced without ICP analysis. While confirming parts of the process is a good indicator, we must assume that all steps leading up to that point are correct. The uptake in Figure 2 indicates the cell line is taking up the compound; this cell line was also shown to take up the cold compound in other unpublished studies from our collaborators. However, in the animal studies, a higher tumor-muscle ratio would be expected based on previous studies. [1] Overall, while these assessments indicate the compound is correct, further testing would be needed to confirm.

Relevance to CIRMS: This work is a part of the doctoral work by the first author on novel radiotracer synthesis and kinetic analysis. This project applies to the Medical Subcommittee, which has Radioactivity Standards and Techniques for Nuclear Medicine as a primary area of interest. When a compound eventually becomes approved for use in the clinic, it must pass rigorous tests to ensure that it is the same compound each time it is produced. Reproducibility helps ensure the radiotracer will behave predictably for each patient – that it will be taken up, retained, or released similarly and in a predictable fashion. This also prevents the patients from receiving excessive, unforeseen dose or toxicity if the incorrectly synthesized tracer were to go somewhere in the body it shouldn't or be retained for a long time, rendering a large dose. The first author aims to become a research scientist investigating novel radiotracers such as these with the eventual goal of clinical implementation.

References

- 1) Mustafi D, Peng B, Foxley S, Makinen MW, Karczmar GS, Zamora M, Ejnik J, Martin H. New vanadium based magnetic resonance imaging probes: Clinical potential for early detection of cancer. *J Biol Inorg Chem* 2009;14:1187-1197.
- 2) Makinen, MW., Bamba, R., Ikejimba, L., Wietholt, C., Chen, CT., Conzen, SD. "The vanadyl chelate bis(acetylacetonato)oxovanadium(IV) increases the fractional uptake of 2-(fluorine-18)-2-deoxy-D-glucose by cultured human breast carcinoma cells." *Dalton Trans*, Vol. 42, 11862-11867, 2013.
- 3) Bonardi, M., Rizzio, E., Gallorini, M., Groppi, F., Mainardi, H. Improved radiochemical separation of no-carrier-added vanadium-48 from proton irradiated titanium target. *Journal of Radioanalytical and Nuclear Chemistry*, 23-28. 2005.
- 4) Selim, SA., Philip, CA, and Mikhail, RS. " THERMAL DECOMPOSITION OF AMMONIUM METAVANADATE." *Thermochemica Acta*, 287-297, 1980.
- 5) Bryant, B. E., Fernelius, W. C. Vanadium (IV) Oxy(Acetylacetonate) Procedure B - Direct Preparation from Vanadium(V) Oxide. In T. Moeller, *Inorganic Synthesis* (pp. 113-116). McGraw-Hill. 1957
- 6) NuDat, National Nuclear Data Center, <https://www.nndc.bnl.gov/nudat2/decaysearchdirect.jsp?nuc=48V&unc=nds>

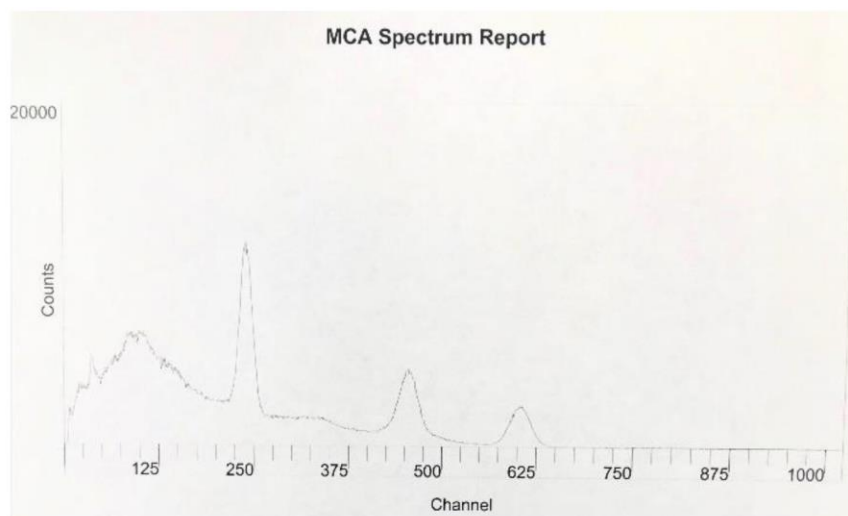


Figure 1. Gamma Ray Spectrometry Analysis

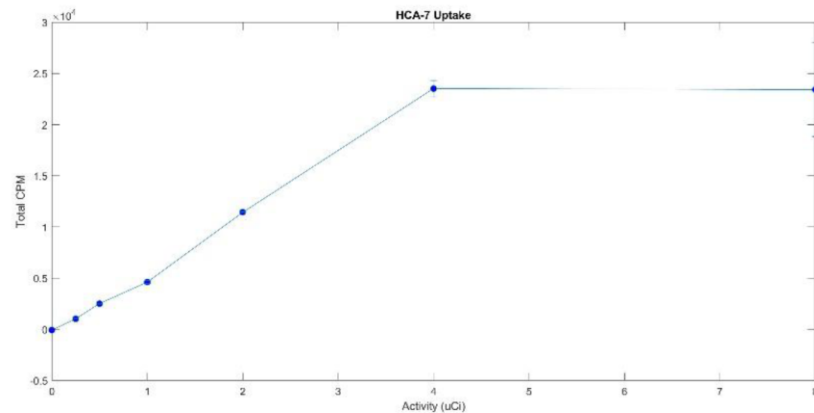


Figure 2. Cell Uptake Curve, HCA-7

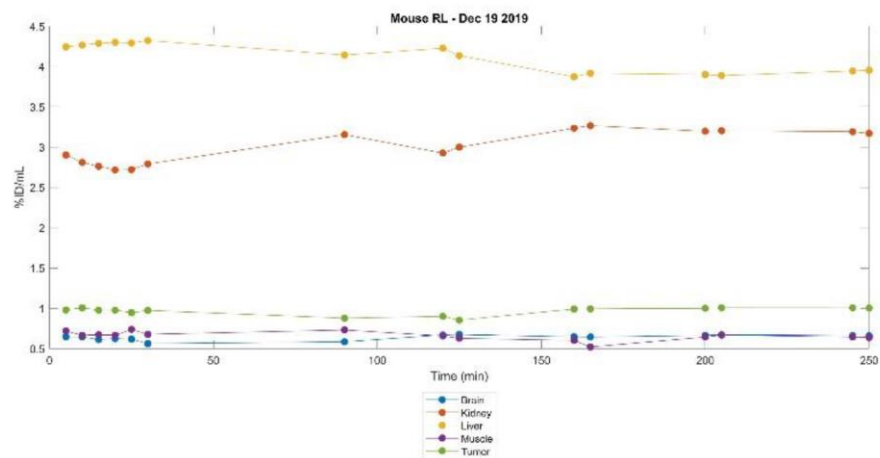


Figure 3. Uptake Curve, Mouse Study

Table 1. ICP and CHN Analysis 1

| Element | Theoretical | Run 1 | | Run 2 | |
|---------|-------------|-------|--------------|-------|--------------|
| | | Found | <i>Diff.</i> | Found | <i>Diff.</i> |
| C | 45.0% | 44.8% | -0.1% | 44.7% | -0.3% |
| H | 6.0% | 5.4% | -0.7% | 5.2% | -0.9% |
| V | 19.1% | 18.6% | -0.5% | | |

Imaging dose in breast radiotherapy by X-ray CT calibration of Cherenkov light

R. L. Hachadorian¹, P. Bruza¹, M. Jermyn^{1,4}, D. J. Gladstone^{1,2,3}, B. W. Pogue^{1,2,3,4}, L. A. Jarvis^{2,3}

¹*Thayer School of Engineering, Dartmouth College, Hanover, NH,*
rachael.l.hachadorian.th@dartmouth.edu

²*Dartmouth-Hitchcock Medical Center, Lebanon, NH*

³*Norris Cotton Cancer Center at Dartmouth Hitchcock Medical Center, Lebanon, NH*

⁴*DoseOptics LLC, Lebanon, NH*

Objective and Background: Until Cherenkov imaging systems became available for research use in 2014, it was not possible to see the beam treating the patient, nor if the deposited dose was consistent each treatment fraction [1]. Despite nearly unlimited ability to measure the transmission of the beam through tissue, there has never been a way to quantify the radiation dose deposited directly, though this work presents the first possibility. Noninvasive, remote ways to measure the absorbed dose in tissue would add a critically important layer to patient safety and management [2].

Perhaps the most unique feature of Cherenkov light is that it is linear to dose, though this linearity is convoluted and difficult to discern in patient tissues due to differences in *in vivo* absorbers, such as blood content or tissue density [3,4]. In this study, the observed Cherenkov light from whole breast radiation therapy treatments is corrected for different patient tissue optical properties using a calibration between Cherenkov light intensity and correlated CT number (HU). This involves correcting for the nonlinearity in absorption such as adipose versus fibro-glandular content, which ultimately yield substantial variation in optical absorption and scattering [4,5]. This particularly relevant correction takes advantage of the ability to measure breast tissue densities from the available patient treatment plans. This work presents the first major step in a multi-part solution to the most limiting aspect of *in vivo* dosimetry, using Cherenkov light.

Materials and Methods: A time-gated intensified camera (C-Dose Research, DoseOptics LLC, Lebanon, NH) was used to image the Cherenkov light emitted during radiotherapy treatments of thirteen patients over the course of this IRB-approved study. The camera was equipped with a 50 mm f/2.8 lens (Nikon Inc, NY), and mounted on the ceiling at IEC 61217 spatial coordinates of (x=-1288, y=1066, z=-687) mm from the linac isocenter.

Results: In Figure 1a, the CT scan of Patient 3 shows the presence of dense, fibroglandular tissue throughout the majority of the breast. Pictured adjacent are Cherenkov images from ten sequential fractions, normalized with respect to the prescribed breast surface dose from the treatment plan, shown as an intensity map in photons·Gy⁻¹. In Fig 1b, a CT scan of Patient 8 shows a contrasting example of predominantly adipose tissue. Consequently, the corresponding dose-normalized Cherenkov images to the right exhibit much higher optical signal as compared those in Figure 1a. In Figure 1c, the median Cherenkov intensities $I_{uncorr,D}(E)$, normalized by dose (denoted with subscript *D*) is plotted with respect to the patient average radiodensity (HU) in the subsurface tissue for 6 MV beams, and (Figure 1d), 10 MV beams.

$$\bar{I}_{uncorr,D}(E)$$

The dose-normalized Cherenkov median intensities, $\bar{I}_{corr,D}(E)$, were corrected using a normalization from the fits in Figure 1c and 1d,

$$\bar{I}_{corr,D}(E) = \bar{I}_{uncorr,D}(E) \cdot c(HU, E) = \bar{I}_{uncorr,D} \cdot \left[\frac{(m(E) \cdot (-135) + b(E))}{(m(E) \cdot HU + b(E))} \right], \quad (1)$$

where $\bar{I}_{uncorr,D}(E)$ is the median intensity of the recorded Cherenkov field in units photons per one Gray of dose delivered (γ Gy⁻¹), and $m(E), b(E)$ are the slope and intercept derived from each fit. Error bars throughout Figure 1 are represented using the root mean square error of $\bar{I}_{uncorr,D}(E)$.

To test the increased linearity of the relationship between calibrated Cherenkov light and absorbed dose, a final evaluation of the correlation was carried out on all corrected image data sets, using all fractions imaged (Figure 2). Circular ROI's were used to relate uncorrected and corrected Cherenkov images $I_{uncorr}(E)$ to dose ($D(E)$), using a simple linear relationship with slope $m_{corr}(E)$,

$$\overline{I_{corr}}(E) = m_{corr}(E) \cdot D(E). \quad (2)$$

Mean values were estimated from these ROI's in the regions of corrected and uncorrected Cherenkov images, avoiding highly absorbing areas. These results are plotted in Figure 2a, uncorrected Cherenkov emission intensity, $\overline{I_{uncorr}}(E)$, and Figure 2b, corrected Cherenkov emission intensity $\overline{I_{corr}}(E)$.

Conclusions and Significance: This study presents the first known approach to non-contact imaging of optical light signal that is linearly correlated to radiation dose in human tissues, offering a relevant step toward absolute radiation dosimetry by non-contact imaging during the treatment procedure. It is entirely passive, requiring no interference to the patient's treatment workflow or the patient care team.

Relevance to CIRMS: This study described about is the most recent output from the first-author's doctoral work, currently in review with Nature Communications. The author earned a CAMPEP-accredited MS degree in 2017 and is currently pursuing a PhD in Medical Physics with the intent of making it her professional career. As stated, CIRMS "has constructed a unique open forum for dialog on all aspects of ionizing radiation," where measuring dose, *in vivo*, may serve as an exciting new paradigm shift in the way radiation dose is measured, by introducing the ability to measure the deposited dose directly in the tissue.

References

- 1) Klein, E.E., et al., Task Group 142 report: quality assurance of medical accelerators. Med Phys, 2009. 36(9): p. 4197-212.
- 2) Jarvis, L.A., et al., Cherenkov video imaging allows for the first visualization of radiation therapy in real time. Int J Radiat Oncol Biol Phys, 2014. 89(3): p. 615-22.
- 3) Zhang, R., et al., Superficial dosimetry imaging based on Cerenkov emission for external beam radiotherapy with megavoltage x-ray beam. Med Phys, 2013. 40(10): p. 101914.
- 4) Zhang, R., et al., Beam and tissue factors affecting Cherenkov image intensity for quantitative entrance and exit dosimetry on human tissue. J Biophotonics, 2017. 10(5): p. 645-656.
- 5) Boyd, N.F., et al., Mammographic density. Breast Cancer Res, 2009. 11 Suppl 3: p. S4.

- 6) Yaffe, M.J., Mammographic density. Measurement of mammographic density. Breast Cancer Res, 2008. 10(3): p. 209.
- 7) Alonzo-Proulx, O., R.A. Jong, and M.J. Yaffe, Volumetric breast density characteristics as determined from digital mammograms. Phys Med Biol, 2012. 57(22): p. 7443-57.
- 8) Boyd, N., et al., Breast-tissue composition and other risk factors for breast cancer in young women: a cross-sectional study. Lancet Oncol, 2009. 10(6): p. 569-80.
- 9) Boyd, N.F., et al., Mammographic density and the risk and detection of breast cancer. N Engl J Med, 2007. 356(3): p. 227-36.

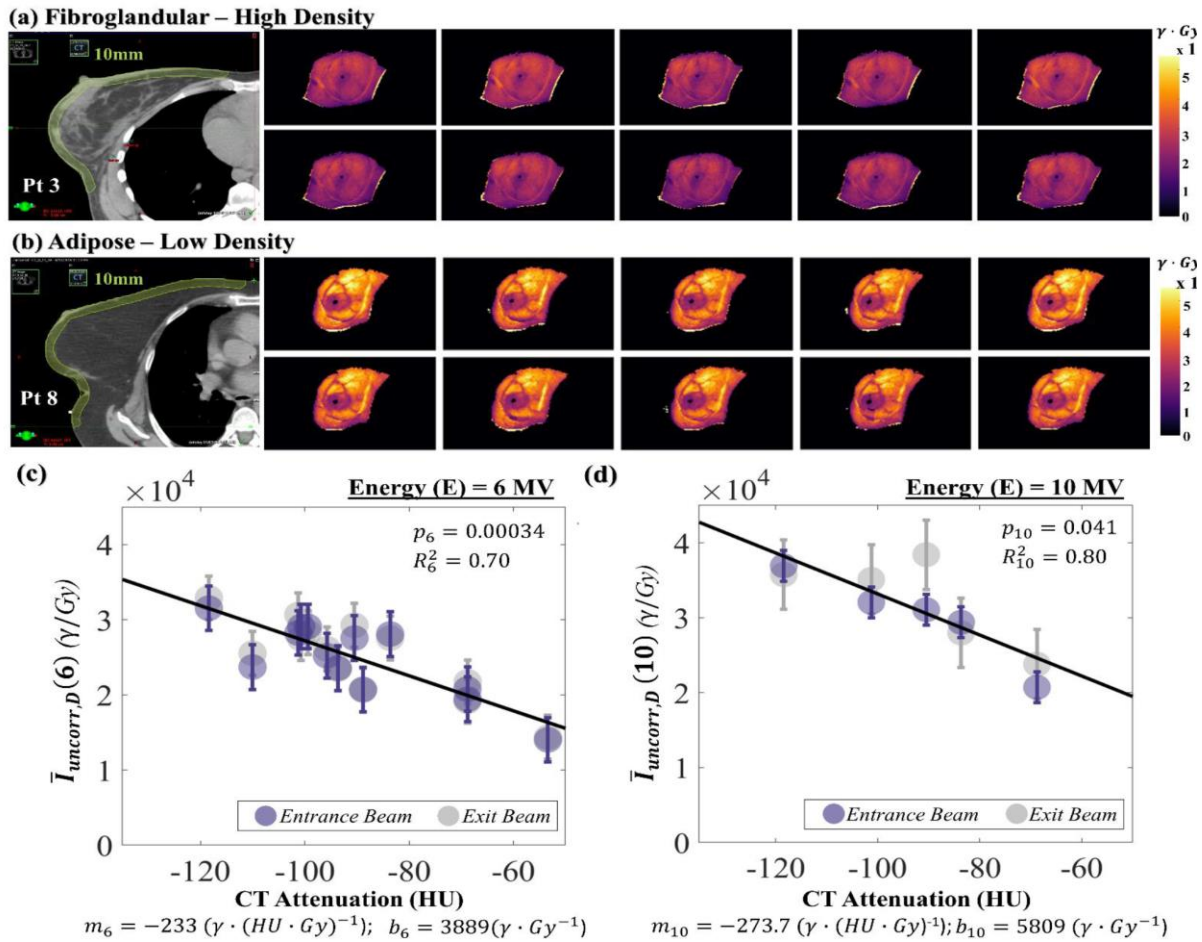


Figure 1. Variability in Cherenkov intensity with fibroglandular and adipose tissue content. In (a), the CT scan of Patient 3 shows dense, fibroglandular content throughout the breast volume. Ten fractions of Cherenkov imaging are pictured (units photons γ), each normalized with respect to dose (Gy) as shown beside this. In (b), the CT scan of Pt 8 is characterized by largely adipose tissue, resulting in a much brighter appearance of Cherenkov images as compared those in (a). Subfigures (c), (d) illustrate the linear correlation between HU and the median Cherenkov counts per unit delivered dose. Subfigure (c) maps this relationship for all thirteen patients treated with 6MV beams, and (d) for the five patients treated with 10X beams. Each point shown is averaged over all fractions for each patient.

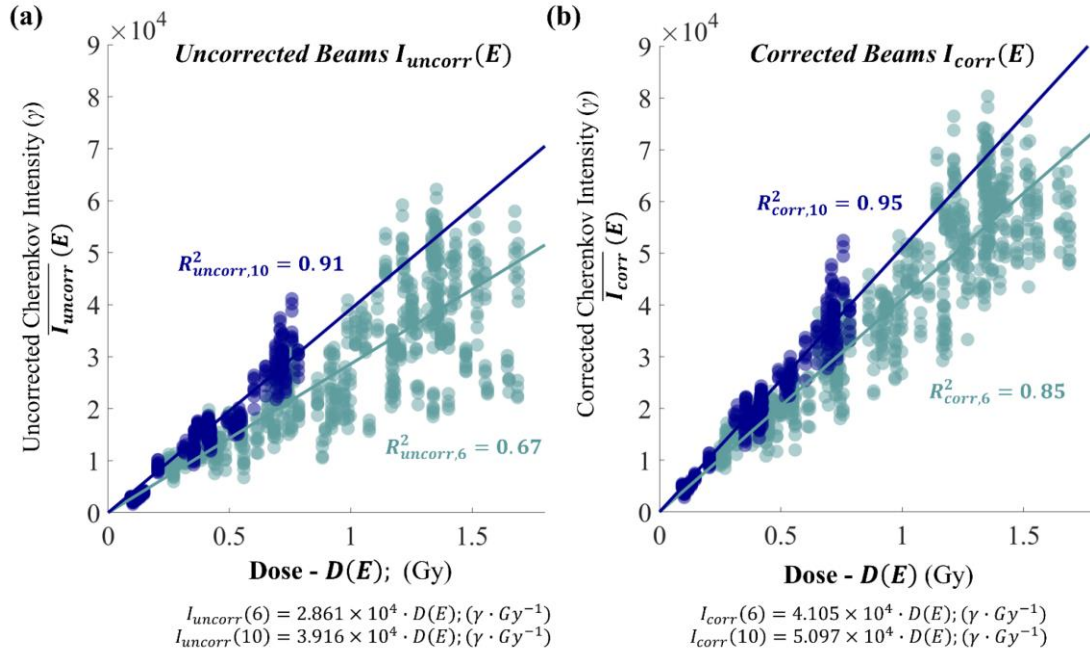


Figure 2. The HU correction increases linearity between Cherenkov light and dose. The median Cherenkov intensities from uncorrected images (a) are plotted against corresponding ROI's from the predicted dose in the treatment plan. The median Cherenkov intensities from the corrected images are then plotted in the adjacent plot (b) for both 6 V and 10 MV beams. The y-intercepts have been constrained to cross at the origin, which yields an uncorrected 6X beam regression $R_{uncorr,62} = 0.67$, which exhibits the largest spread of data. The HU-corrected 6X beam regression is improved by .18, to $R_{corr,62}$ of 0.85. The linear regression of the 10X beams are improved slightly by 4%, from 0.91 to 0.95.

Quantifying uncertainty in microdosimetric measurements for carbon ion radiotherapy

Shannon Hartzell¹, Fada Guan¹, Paige Taylor¹, Oleg Vassiliev¹, Christine Peterson², Stephen Kry¹

¹*Department of Radiation Physics, The University of Texas MD Anderson Cancer Center, Houston, TX, shartzell@mdanderson.org*

²*Department of Biostatistics, The University of Texas MD Anderson Cancer Center, Houston, TX*

Objective: Microdosimetry is a technique which allows the systematic analysis of energy deposition patterns on a microscopic platform to provide track information that is essential in understanding radiotherapy beam characteristics [1]. This is accomplished with the concept of lineal energy, which is the sum of all energy deposits in a microscopic volume (i.e. $\sim 1 \mu\text{m}$). Dosimetric assessment of energy deposition within sites of this magnitude are crucial as this is the scale at which biological effects occur, such as DNA damage from radiation therapy [2]. Microdosimetry is a particularly important tool in the developing area of carbon radiotherapy, a technique that involves acceleration of carbon nuclei to nearly 75% the speed of light to provide highly localized tumor dose. Carbon radiotherapy utilizes microdosimetric quantities to describe its biological effectiveness as compared to reference radiation (RBE). RBE is used in patient treatment plans and requires measurement-based verification to ensure accurate implementation and subsequent patient dose delivery.

Various detectors can be used to make microdosimetric measurements, with the most common being the Tissue-Equivalent Proportional Counter (TEPC). TEPC measurements, as any physical measurements, are subject to various inherent sources of uncertainty resulting from detector design and beam setup. Of particular interest is the effect of these uncertainty sources on the three fundamental microdosimetric quantities that describe energy deposits and biological effect, including frequency weighted ($\bar{y}F$), dose weighted ($\bar{y}D$), and saturation corrected dose mean lineal energy (y^*). This work quantifies the measurement-based uncertainty in lineal energy measurements made by a commercial TEPC in a therapeutic carbon beam.

Methods: Geant4 Monte Carlo was used to simulate microdosimetric spectra of a standard carbon beam incident on a water tank for five monoenergetic beams spanning a typical clinical beam range (146 to 424 MeV/u). An additional weighting scheme was created to define spectra for spread-out Bragg Peaks (clinically relevant dose distributions) of 5 cm, 7 cm, and 10 cm in length. From each of these simulated spectra, lineal energy values were calculated as a function of depth in water.

In order to assess the impact of measurement based uncertainty on the simulated spectra, the ICRU Report 36 on Microdosimetry was used to identify eight sources of uncertainty expected to affect TEPC measurements, including counting statistics, mean chord length, gain instability, electronic uncertainty, low energy cutoff, W-value and calibration, pulse pile-up, and wall effects. Each of the eight sources had associated random uncertainty, while the last four sources contained additional systematic components. A MatLab code was written to simulate the effect of each independent source of uncertainty on microdosimetric spectra by perturbing the default frequency and dose weighted spectra over a series of 200 iterations. The magnitude of the perturbation was quantified according to the anticipated effect of the source based on detector properties and clinical beam setup. For each perturbed spectrum the respective lineal energy values were recalculated. The standard deviation across the 200 perturbed values for each depth and beam provided error bars at

the 1σ level for each uncertainty source. For sources that included systematic components, bias was additionally quantified by the percent difference between the default lineal energy values and the average of the perturbed values, yielding a shift in addition to the standard deviation about that shift.

Results: The variance introduced by random noise in both $\bar{y}F$ and $\bar{y}D$ values averaged 4.7% and 5.0%, respectively, and did not exceed 5.6%. As noise in the Monte Carlo simulation was highest with $\bar{y}D$ values, elevated uncertainty in this value may be of less consequence. Variance in y^* values were notably lower, averaging just 3.3% across all beam energies. The impact of the bias typically ranged from 0.01-5.0%, with the lowest magnitude also seen in y^* , averaging 3.6% across all simulated beams. The largest contributing source to the bias was pulse pileup, which is driven by the dose rate of the beam. While the maximum dose rate that can be used to create reasonable error was used in this assessment, this rate can typically be mechanically tuned down to reduce bias by 40-70%.

Conclusions and Significance: These values provide an uncertainty analysis for the clinical use of microdosimetric measurements made by a TEPC. The parameter that showed the least uncertainty, y^* , is designed to describe the biological effect and is paramount in current biological modeling. The ability to measure this value within reasonable accuracy is needed to verify the clinical implementation of RBE models and establish consistency in delivered dose. Errors in this value may result in significant reduction in treatment outcome and overall survival among radiotherapy patients as well as a lack of consistency across clinical trials. The results indicate that a commercial TEPC can be used to measure microdosimetric quantities, and subsequent RBE, within reasonable accuracy ($\pm 5\%$) using proper detector and beam setup.

Relevance to CIRMS: Compared to traditional dosimetry, microdosimetry is a novel field that is quickly becoming essential in understanding biological effects in heavy ion radiotherapy. Quantifying underlying uncertainty in clinical measurements, based on a variety of beam and detector setups, is crucial in establishing dosimetry standards in the rapidly developing area of particle therapy. This aligns with the 2020 CIRMS theme of building synergy among labs and end users, as this work will standardize both microdosimetric measurements and RBE implementation to address an area of high uncertainty, and high importance, in heavy ion radiotherapy.

In the field of medical physics, standardization is essential in ensuring accurate and consistent radiation delivery to improve both clinical treatment outcomes and reliability of research techniques. In my professional career, I plan on working in a role that is split between both clinical and research positions, which will require understanding and implementing standardization across all radiation modalities. I hope to use this opportunity at CIRMS to explore various techniques that are both available and being developed for medical applications and radiation protection.

References

- 1) 1983. Microdosimetry. In: Measurements, I. C. O. R. U. A. (ed.) ICRU Report. Bethesda, MD.
- 2) Lindborg, L. & Walker, A. 2017. Microdosimetry: Experimental Methods and Applications, Boca Raton, FL, CRC Press Taylor & Francis Group.

Unstructured mesh unification for MCNP6.2

Peter J. Kowal, Kurt A. Dominesey, Jonathan A. Eugenio, and Wei Ji

Department of Mechanical Aerospace and Nuclear Engineering, Rensselaer Polytechnic Institute, 110 8th Street, Troy, NY, kowalp@rpi.edu

Objective: A critical and often complex part of radiation calculations is defining a proper model. Foremost, the model must be an accurate representation of its physical counterpart. Additionally, the model must be useable by the code performing the radiation calculations. To further complicate things, a variety of modeling methodologies are used in different codes and each code has its own input format nuances. This leads to the scenario where a model of a radiation system exists but cannot be directly used by the code of interest. Consequently, a user may have to start again from scratch for no other reason than incompatible file formats. To avoid these issues, it is necessary to provide model unification between codes. Model unification offers both convenience and the potential for greater coupling between different codes.

An example of this issue can be seen with the Monte Carlo radiation transport code MCNP6.2 and the wide variety of available finite element transport codes, such as Attila [1]. As an extensively validated continuous energy Monte Carlo code, MCNP6.2 is often treated as the gold standard for high fidelity simulations such as those necessary for dosimetry measurements. Finite element codes are typically constrained to multi-group models and are thus lower fidelity than a code like MCNP6.2, but have many existing meshed models. MCNP6.2 can also use unstructured meshes, but is constrained to the Abaqus format which significantly limits the number of available models. To address this issue the Ex2Ab mesh conversion utility was created. Ex2Ab converts the more general use Exodus II mesh into the specific version of the Abaqus format that is usable by MCNP6.2 [2]. By using Ex2Ab, modeling for MCNP6.2 can begin with an existing Exodus II mesh or a meshing program other than Abaqus. An example of this is shown in Fig. 1 where Cubit is used as the meshing program.

Materials and Methods: Ex2Ab provides comprehensive mesh conversion from the Exodus II format to the version of the Abaqus format used by MCNP6.2. The program also provides a few functions such as element type checking and input deck set up to make using unstructured meshes in MCNP6.2 more user friendly.

There are a plethora of 3D element types that can be used in unstructured meshes, but only a small subset of them are MCNP6.2 compatible [3]. Ex2Ab reads the Exodus II file and checks what element type each region of the model is. The mesh will only be converted if all element types are compatible. If there are any incompatibilities, the user will be informed where the problem elements are located.

Using unstructured meshes in MCNP6.2 requires a specialized setup of the MCNP input deck. Building an input deck for an unstructured mesh problem is different than for legacy MCNP problems using constructive solid geometry (CSG). For example, the cell and surface cards for an unstructured mesh problem do not explicitly define all facets of the geometry since that information comes from an external mesh file. A special set of data cards is also required for MCNP6.2 to properly reference the mesh file. Due to these differences, it is convenient to automatically generate these parts of the input file for the user. Ex2Ab generates this “skeletal

input” that only includes the unstructured mesh related sections of the full input file. It is used to streamline the creation of the full input file and cannot be run on its own.

Reflecting boundaries are an important model feature that allow the model size to be minimized when symmetry is present. This feature is supported in MCNP6.2, but is not totally straightforward with unstructured meshes. When using unstructured meshes, the mesh based geometry becomes a series of pseudo-cells (a specialized subset of MCNP cells) within a universe [3]. This universe, which contains the entire mesh model, is bounded by an outer surface. For CSG problems, this outer boundary surface can be made reflecting. For unstructured mesh problems, making the universe boundary a reflecting surface will cause errors [3]. This becomes problematic when the model requires reflecting boundaries on all sides. This issue can be solved by creating a second surface offset slightly from the universe boundary. Ex2Ab is able to handle this for the user provided that the desired reflecting surfaces from the model are indicated. To designate a reflecting boundary, the user must define a node set on the chosen surface of the model.

Results: Ex2Ab operates successfully on meshes using first and second order hexahedral and tetrahedral elements (these are all of the applicable element types that may be generated in Cubit). The reflecting boundary feature also functions as expected for planar boundaries on the exterior of the model. Additionally, the element type checks reliably prevent conversion of meshes using elements that are incompatible with MCNP6.2. The terminal output from a successful conversion of a mesh with four material regions and reflecting boundaries is shown in Fig. 2. In Fig. 3, the generated skeletal input file is shown.

Conclusions and Significance: This work has shown that model unification between MCNP6.2 and finite element transport codes with the Ex2Ab utility is successful. By using an existing unstructured mesh, a MCNP6.2 model can be generated with all of the relevant unstructured mesh cell, surface, and data cards. This provides the user with a convenient method to build MCNP6.2 models based on existing unstructured meshes in the Exodus II format.

Relevance to CIRMS: The primary author has led the development of the Ex2Ab utility as part of their doctoral research and as a component of the NEAMS Workbench project which aims to increase the usability of nuclear engineering codes such as MCNP6.2. Informing scientific codes is a key application of data from standards labs such as NIST. Thus, by enabling users to be more productive with their simulations, the best possible use of high quality lab data is achieved. Additionally, improvements to unstructured mesh capabilities facilitates more detailed modeling of complicated lab systems as may be required for producing standards and benchmarks.

References

- 1) T. A. Wareing, J. M. McGhee, and J. E. Morel, “ATTILA: A three-dimensional, unstructured tetrahedral mesh discrete ordinates transport code,” *Trans Am Nucl Soc*, volume 75, pp. 146–147 (1996).
- 2) P. J. Kowal, K. A. Dominesey, M. N. Dupont, J. A. Eugenio, and W. Ji. “Unstructured Mesh Unification for MCNP6.2 and PROTEUS in NEAMS Workbench,” *Trans Am Nucl Soc*, volume 121, pp. 1541–1544 (2019).
- 3) R. L. Martz, “The MCNP6 Book on Unstructured Mesh Geometry: User’s Guide for MCNP 6.2,” Tech. Rep. LAUR-17-22442, Los Alamos National Laboratory (2017).

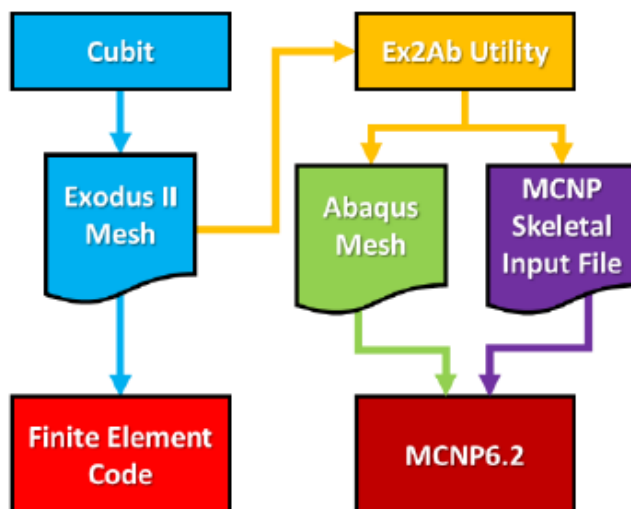



Figure 1. Unstructured Mesh Unification with Ex2Ab Utility.



```
Welcome to the Exodus II to Abaqus Conversion Script!
Mesh Conversion begins
Source Mesh: C:/Users/kowalp/Documents/Research/Ex2Ab/old/4pin_complete.g
Job name: 4pin_complete

4 block(s) were detected
Density attribute was defined for blocks
Cell 1 density: -10.08
Cell 2 density: -0.000178
Cell 3 density: -8.0
Cell 4 density: -0.9986
6 reflecting boundaries will be defined from node sets

skeletal MCNP input has been written

285768 nodes detected, Runtime: 0.07 sec
Block 1 has 95400 HEX8 elements, Runtime: 10.22 sec
Block 2 has 22896 HEX8 elements, Runtime: 13.5 sec
Block 3 has 24168 HEX8 elements, Runtime: 14.4 sec
Block 4 has 130751 HEX8 elements, Runtime: 15.45 sec

The conversion took 21.34 sec
Mesh converted to Abaqus inp format
```

Figure 2. Ex2Ab Terminal Output.


```

c PSEUDO-CELLS
c Each of these cells is one block (element set)
01      1      -1.008E+01  0  u=1
02      2      -1.780E-04  0  u=1
03      3      -8.000E+00  0  u=1
04      4      -9.986E-01  0  u=1
c This is the mesh universe background cell
05      0              0  u=1
c
c LEGACY CELLS
c This cell contains the mesh universe
06      0      -99 -98 -97 -96 95 94 93  fill=1
c This is the space between your UM universe boundary
c and the reflecting boundaries
07      0      -99 -92 -91 -90 89 88 87  #6
c This cell is the space outside the UM universe
08      0      #6 #7

c
c SURFACES
c Additional surfaces for reflecting boundaries were
c defined from side sets. All reflecting surfaces are
c intentionally offset from the UM universe boundary
c
98  P   0.00000E+00  0.00000E+00  1.00000E+00  2.54001E+00
*92  P   0.00000E+00  0.00000E+00  1.00000E+00  2.54002E+00
97  P   0.00000E+00  1.00000E+00  0.00000E+00  1.62561E+00
*91  P   0.00000E+00  1.00000E+00  0.00000E+00  1.62562E+00
96  P   1.00000E+00  0.00000E+00  0.00000E+00  1.62561E+00
*90  P   1.00000E+00  0.00000E+00  0.00000E+00  1.62562E+00
95  P   0.00000E+00  1.00000E+00  0.00000E+00 -1.62561E+00
*89  P   0.00000E+00  1.00000E+00  0.00000E+00 -1.62562E+00
94  P   1.00000E+00  0.00000E+00  0.00000E+00 -1.62561E+00
*88  P   1.00000E+00  0.00000E+00  0.00000E+00 -1.62562E+00
93  P   0.00000E+00  0.00000E+00  1.00000E+00 -1.00000E-05
*87  P   0.00000E+00  0.00000E+00  1.00000E+00 -2.00000E-05
99  SPH 0.00000E+00  0.00000E+00  1.27000E+00  2.65268E+00

c
c DATA CARDS
c These cards link MCNP to the appropriate mesh file
c The number on embed must match the universe number
embed1 meshgeo=abaqus
      mgeo=4pin_complete.inp
      meeout=4pin_complete.eeout
      length=1.0
      background=5
      filetype=binary
      matcell=
        1 1
        2 2
        3 3
        4 4
c
c Please add particle types to the importance card
imp:PICK YOUR PARTICLES 1 6R 0

```

Figure 3. MCNP Skeletal Input from Ex2Ab.

An open-source algorithm to standardize neutron spectra unfolding in radiation therapy

Logan Montgomery¹, Anthony Landry², Georges Al Makdessi¹, Felix Mathew¹, John Kildea¹

¹Medical Physics Unit, McGill University, Montreal, QC, Canada,

logan.montgomery@mail.mcgill.ca

²Department of Radiation Oncology, Dalhousie University, Halifax, NS, Canada

Objective: Secondary neutrons that are produced by medical linacs pose a carcinogenic risk to radiation therapy patients and staff. Because the carcinogenic risk from neutron radiation is believed to vary widely with energy [1], risk assessment requires accurate determination of the neutron fluence spectrum. To this end, specialized detectors like the Nested Neutron Spectrometer (NNS) [2] can be used, although the raw neutron counts-per-second (CPS) data must be deconvolved (i.e. unfolded) with the detector response functions in order to yield the spectrum of interest.

Our group has demonstrated that the iterative Maximum-Likelihood Expectation–Maximization (MLEM) algorithm can be used to unfold NNS measurements in the high dose-rate radiation therapy environment [3]. We previously relied on subjective user experience to terminate the MLEM unfolding both (i) after sufficient spectral convergence and (ii) prior to significant accumulation of spectral noise. To standardize our methodology and improve confidence in our results, we developed an objective stopping criterion that satisfies both of the aforementioned criteria and eliminates user variability.

Many algorithms have been proposed in the literature for unfolding neutron spectra but are often not open source. Thus, implementing others' work based on details in a manuscript alone can be difficult, time-consuming, and error-prone. To foster a culture of standardized practice and collaboration, we invested time into making our code user-friendly and provided it as open-source software on Github [4].

Materials and Methods: The NNS consists of a He-3 proportional counter that is sensitive to thermal neutrons and seven cylindrical high-density polyethylene moderator shells that are assembled in Russian nesting doll fashion. A schematic of the process for unfolding NNS measurements is shown in Fig. 1. To improve precision, each CPS value m_i was an average of three repeat measurements. To estimate spectral uncertainties, the mean and standard deviations of the repeat measurements were used to define Gaussian distributions. Each distribution was sampled 100 times to yield 100 pseudo-measurement sets, which were then unfolded individually. The root-mean-square deviation between the experimental unfolded spectrum and the 100 unfolded pseudo-spectra was taken as the uncertainty.

We developed a stopping criterion based on the published MLEM-STOP method for PET image reconstruction [5], in which unfolding is terminated when an indicator function J^k falls below a threshold value J_t . In the original formulation, J_t is a static value defined to terminate MLEM when the MLEM-reconstructed measurements (q_i^k) are within the Poisson counting uncertainty of the corresponding m_i . However, we found this formulation did not apply well to the wide range of neutron CPS values and corresponding fluence rates ($\sim 10^4$ to 10^6 n·cm⁻²·s⁻¹) that we measured using the NNS in radiation therapy, and thus we derived a new formulation of J_t . This

modified MLEM-STOP method capitalizes on the fact that the rate of MLEM convergence is independent of measurement magnitude without violating the statistical basis of the original formulation.

We applied our new method to two classes of NNS datasets:

- (1) Validation datasets acquired around a Varian Clinac 21EX having known ground-truth spectra (simulated in MCNP) and thus a known ideal number of MLEM iterations.
- (2) Testing datasets acquired around a Varian TrueBeam, for which the ground-truth spectra were unknown due to lack of a Monte Carlo model of the linac.

Results: Figure 2a shows an example of a validation NNS dataset obtained using our modified MLEM-STOP method compared with the spectrum obtained at the ideal number of iterations. Figure 2b shows an example of a testing NNS dataset obtained using our modified MLEM-STOP method compared with spectra obtained at empirical upper and lower iteration limits.

Conclusions and Significance: For all validation datasets, we found that our modified MLEM-STOP spectra agreed with the ideal unfolded spectra within uncertainty. For testing datasets, we observed that our MLEM-STOP spectra are largely free of noise and are significantly different than the spectra that were obtained at empirical upper and lower iteration limits. Thus, our algorithm offers an objective approach to unfold neutron fluence spectra in radiation therapy that does not require subjective user input. Its use increases user confidence in the unfolded spectrum and thus facilitates more accurate assessment of the risk posed to patients by secondary neutrons.

Relevance to CIRMS: Detecting neutrons is conventionally regarded as a challenging and highly uncertain measurement process. In this work, we have eliminated one source of uncertainty by making the unfolding process objective and statistically rigorous. Additionally, we have released our code as open source and hope to foster a culture of collaboration and standardized practice within the neutron spectrometry community. This project is one aspect of our research group's larger goal to reduce the uncertainty associated with characterizing neutrons and their carcinogenic risk in radiation therapy.

References

- 1) Baiocco G, et al. The origin of neutron biological effectiveness as a function of energy. *Sci Rep.* (2016).
- 2) Dubeau J, et al. A neutron spectrometer using nested moderators. *Radiat Prot Dosim.* (2012).
- 3) Maglieri R, et al. Measuring neutron spectra in radiotherapy using the nested neutron spectrometer. *Med Phys.* (2015).
- 4) Montgomery L, et al. Neutron spectrometry. Github repository. <http://dx.doi.org/10.5281/zenodo.3610493>.
- 5) Ben Bouallègue F, et al. A heuristic statistical stopping rule for iterative reconstruction in emission tomography. *Ann Nuclear Med.* (2013).

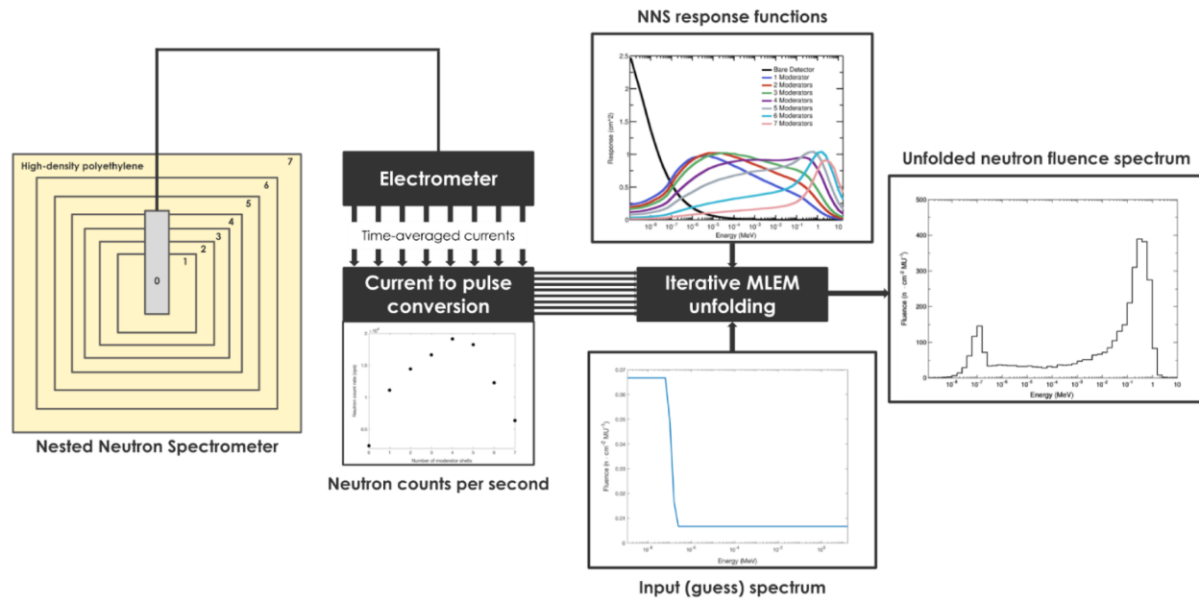


Figure 1. Schematic of the NNS unfolding process. A time-averaged neutron current is measured for each moderator shell configuration and converted to neutron CPS. These neutron CPS are input into the MLEM algorithm along with the NNS response functions and a guess spectrum. The algorithm iterates until terminated, yielding the neutron fluence spectrum.

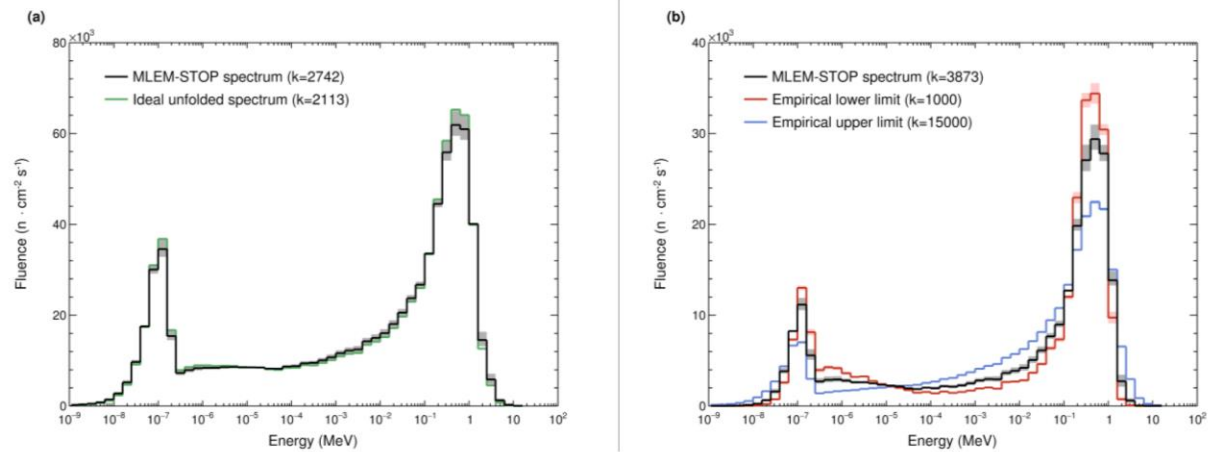


Figure 2. Neutron fluence spectra obtained by unfolding NNS datasets with our modified MLEM-STOP algorithm. (a) A validation dataset (18 MV beam, measured 140 cm from isocenter) compared with the spectra obtained at the known ideal number of iterations. (b) A testing dataset (15 MV beam, measured 100 cm from isocenter) compared with spectra obtained at empirical upper and lower iteration limits. Iteration numbers indicated as k .

Mevex's new radiation transport library for CAD models: an open-source collaboration between Mevex and the Canadian National Research Council

Max Orok^{1,2}, Dave Macrillo², Matt Ronan², Nigel Vezeau², and Lou Thompson²

¹*Department of Mechanical Engineering, University of Ottawa, Ottawa, Ontario, Canada*

²*Mevex Corporation, Stittsville, Ontario, Canada, morok028@uottawa.ca*

Objective: EGSnrc is a widely used Monte Carlo radiation transport code maintained by the Canadian National Research Council (NRC) [1]. It has been in continuous development since the 1960s [2]. Mevex is a linear accelerator manufacturer. Mevex simulates radiation transport using EGSnrc and uses the results to inform product design and aid customer service efforts.

EGSnrc users describe simulations using input files. Before simulations, model geometries must be translated into combinations of EGSnrc geometry primitives and conform to EGSnrc's idiosyncratic input file syntax [3]. This prerequisite translation step is an error-prone barrier to modelling complex geometries and it delays iterative design efforts. For simple geometries like spheres or boxes, the translation step is relatively straightforward. For more complex models, exhaustively describing each shape is onerous.

Designers and engineers think in CAD, so our goal is to directly simulate CAD models in EGSnrc. To that end, Mevex developed a finite-element mesh library for CAD models and contributed it to EGSnrc. The EGSnrc project team is helping Mevex to verify, test and document this new library for use by the entire radiation simulation community.

Methods:

Implementing a new EGSnrc geometry

The EGSnrc geometry interface was designed to be extensible [3]. New geometries are added as child classes in a C++ object-oriented class hierarchy. We implemented a tetrahedral mesh geometry without modifying the underlying physics code. According to the specification [3], new geometries must:

1. Detect if a particle is inside the geometry,
2. Calculate the shortest distance to the geometry along a given direction, and
3. Calculate the shortest distance to the geometry boundary.

We first implemented a single tetrahedron and were able to satisfy the geometry criteria using the well-known geometrical properties of a tetrahedron (volume, surface area, face normal directions, etc.). We then extended our implementation to a large number of connected tetrahedrons, i.e. a tetrahedral mesh.

Tetrahedral meshes allow for accurate modelling of curved surfaces and are relatively simple to generate [4]. Tetrahedral meshes have been implemented in other particle transport codes, notably Geant4 [5, 6]. Tetrahedral mesh geometries were visually inspected for correctness using the EGSnrc visualization tool `egs_view`. Each tetrahedron knows its neighbors, affording rapid particle transport between tetrahedrons. Our code includes a fast nearest-neighbors algorithm for finite-element meshes following Löhner [7]. Our implementation requires the

entire geometry to be discretized. Materials are assigned per volume (box, cylinder, etc.) and then to the volume's constituent tetrahedrons.

Mesh generation and material assignment

We use Gmsh, an open source mesh generator, to generate tetrahedral meshes using an input CAD STEP file (see Figure 1) [4]. We also use Gmsh as a simulation front-end to associate material data with geometries and finally to visualize results (Figure 2). This is an alternative method compared to Pinto and Gonçalves' standalone tool for assigning materials to STEP files for Geant4 [6]. The new tetrahedral mesh geometry is completely general and Gmsh is only one possible path to a suitable mesh.

Results: The new mesh library greatly increases the ability of researchers to simulate evermore complex shapes. Figure 3 compares two car models: one generated "by hand" with an EGSnrc input file and one created in CAD.

At the time of writing, we continue to validate the new mesh geometry library in collaboration with the NRC. Nevertheless, preliminary tests show the mesh library yields comparable results to reference geometries. Table 1 shows energy deposition results for a meshed cube of water. Results for different meshes are compared to a reference value calculated using the pre-existing box geometry. Though each value is relatively similar, there is further work required to understand the resulting variation between different meshes.

Tetrahedral meshes also offer better mesh size control compared to existing rectilinear grids currently implemented in EGSnrc. Unlike the EGSnrc application dosxyznrc where refinement is per-coordinate [8], a generalized mesh allows us to refine local areas of interest without a global resolution increase.

Conclusions and Significance: This work allows researchers to more easily simulate complex CAD designs using the trusted radiation transport code EGSnrc. We tetrahedralize the entire simulation geometry using the mesh generator Gmsh and then simulate transport through each tetrahedron. The EGSnrc mesh geometry is general, and our code could be extended to work with other mesh generators. Our method reduces overall simulation time by removing the error-prone and tedious translation step between CAD models and the EGSnrc geometry input file format. Verification efforts are ongoing with the support of the NRC, but preliminary tests show that results obtained using the new mesh library are comparable to primitive EGSnrc geometries.

Relevance to CIRMS: Mevex implemented a new and useful feature for EGSnrc, thanks to the extensible design of the EGSnrc geometry interface. We are moving forward in collaboration with the NRC to validate and test the new geometry for use by the entire simulation community. This furthers the CIRMS goal of collaboration between standards labs and end users. This work is related to the first author's master's thesis, who aims to become a staff scientist at a national lab.

References

- 1) I Kawrakow, E Mainegra-Hing, DWO Rogers, F Tessier, BRB Walters. "The EGSnrc Code System: Monte Carlo simulation of electron and photon transport". Technical Report PIRS-701, National Research Council Canada (2017).

- 2) Richard L Ford and Walter Ralph Nelson. "EGS code system: computer programs for the Monte Carlo simulation of electromagnetic cascade showers. Version 3" Tech. rep. Stanford Linear Accelerator Center, CA (USA), 1978.
- 3) Kawrakow, I., Mainegra-Hing, E., Tessier, F., Townson, R. & Walters, B. R. B. (2019). The EGSnrc C++ class library. NRC Report PIRS-898.
- 4) C. Geuzaine and J.-F. Remacle. "Gmsh: a three-dimensional finite element mesh generator with built-in pre- and post-processing facilities". International Journal for Numerical Methods in Engineering 79(11), pp. 1309-1331, 2009.
- 5) Gabriel Paiva Fonseca et al. "The use of tetrahedral mesh geometries in Monte Carlo simulation of applicator based brachytherapy dose distributions." Phys. Med. Biol. 59 5921, 2014.
- 6) Pinto, Marco, and Patrícia Gonçalves. "GUIMesh: A tool to import STEP geometries into Geant4 via GDML." Computer Physics Communications 239 (2019): 150-156.
- 7) Löhner, R. (2008). Data Structures and Algorithms. In Applied Computational Fluid Dynamics Techniques, R. Löhner (Ed.).
- 8) Walters, B. R. B. I., Iwan Kawrakow, and D. W. O. Rogers. "DOSXYZnrc users manual." NRC Report PIRS 794 (2005): 1-125.

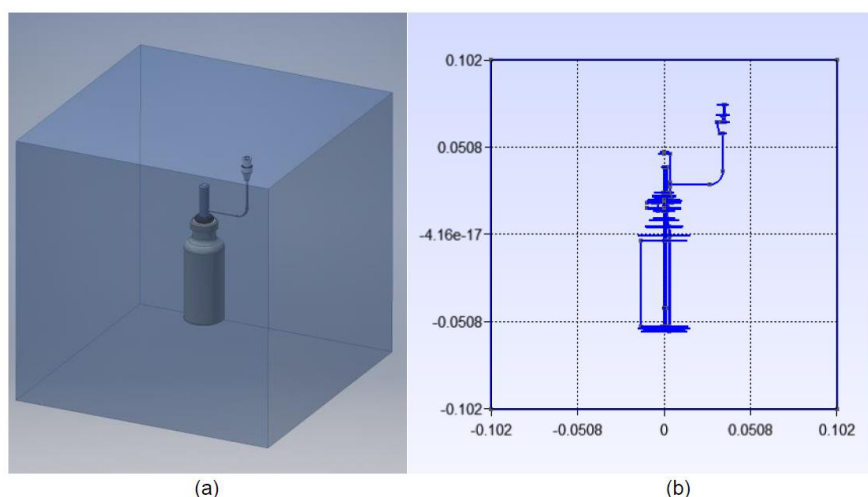


Figure 1. (a) CAD model of sterilization target surrounded by air and (b) the model opened in Gmsh before meshing.

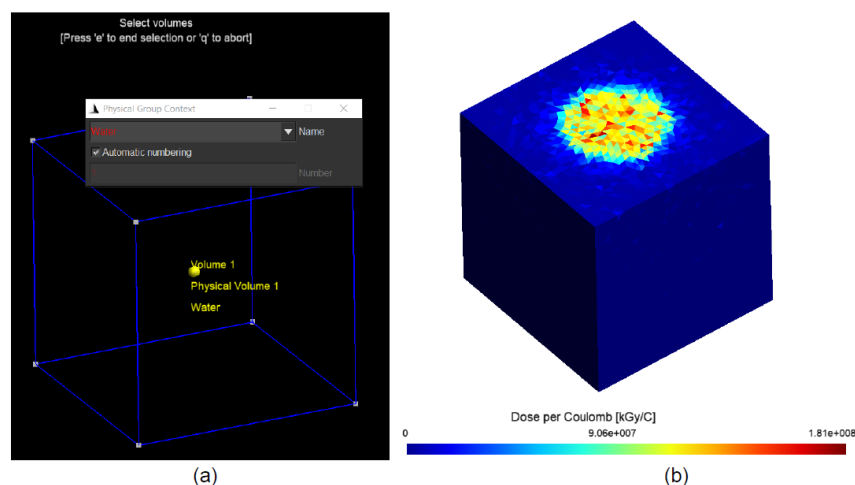


Figure 2. (a) Assigning EGSnrc materials to volumes using Gmsh and (b) visualizing EGSnrc dose deposition results in Gmsh.

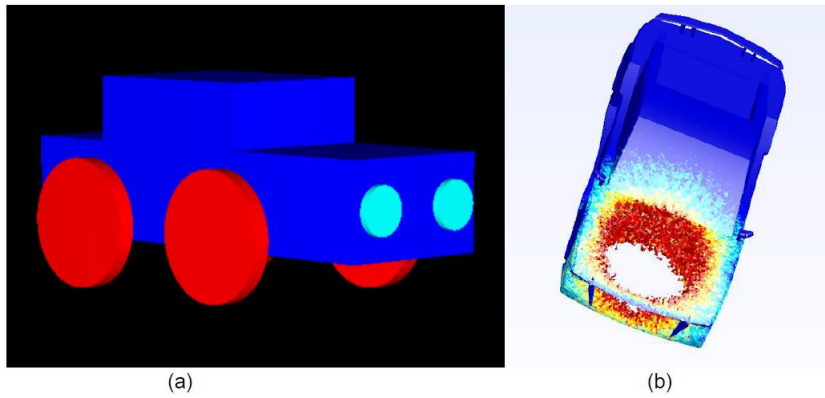
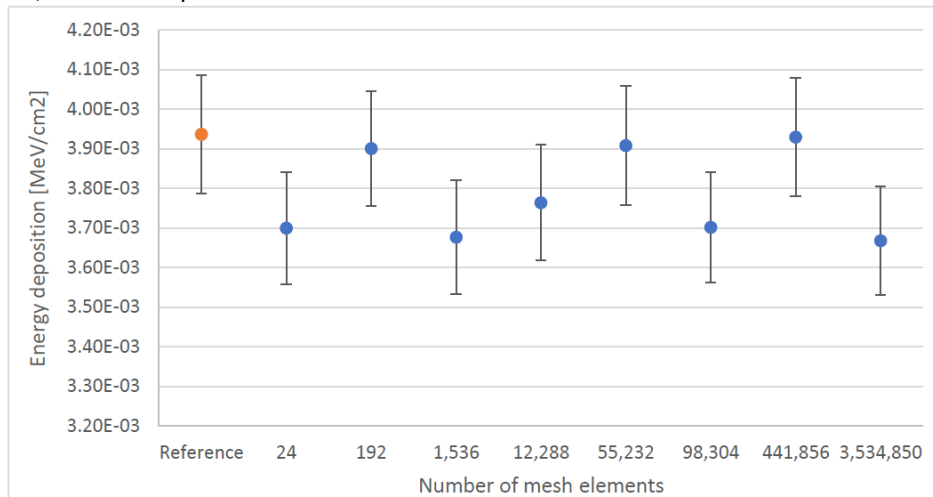


Figure 3. (a) A car built using an EGSnrc input file [3] and (b) a meshed car model's dose distribution after simulation. The car was simulated as if it had a cobalt-60 engine.

Table 1. Energy deposition vs number of mesh elements (66% confidence interval) for 100,000 10 MeV photons incident on a 1cm³ water cube



A statistical analysis of HDR Ir-192 customer well chamber calibrations at an ADCL

Blake R Smith, Larry A DeWerd, and Wesley S Culberson

University of Wisconsin, School of Medicine and Public Health, Department of Medical Physics
Medical Radiation Research Center, bsmith34@wisc.edu

Objective: Careful consideration should be given to maintaining NIST traceability while calibrating well-type ionization chambers used to measure the air-kerma strength, S_K , of brachytherapy sources [1-3]. This is especially true for HDR Ir-192 as NIST does not maintain an S_K measurement standard but recognizes interim standards that are maintained by the Accredited Dosimetry Calibration Laboratories (ADCLs) [4, 5]. Outside of the uncertainty associated with this calibration technique, differences in the production of a chamber model may lead to a variation in a chamber model's calibration coefficient. In an effort to study this variability with respect to the performance of the instrument, previous works have investigated the stability and distribution of absorbed dose-to-water calibration coefficients with reference-class ionization chambers to quantify chamber-to-chamber variability in their K_Q response [6]. In like manner, it was the purpose of this study to present a retrospective analysis of customer well-type ionization chamber calibrations performed at an ADCL to investigate (i) variations in response among well-type ionization chambers of the same model and (ii) stability and constancy among repeated chamber calibrations.

Materials and Methods: The chamber calibration records at the University of Wisconsin Accredited Dosimetry Calibration Laboratory (UWADCL) were retrospectively analyzed for several well chamber models between the calibration dates of 1996 to 2019 and are listed in Table 1. A calibration was only considered in this work if it had been formally disseminated to the customer and followed an accredited calibration protocol.

All data compilation and statistical analysis was performed using MATLAB (version R2018a). The primary quantity studied in this work was the chamber's calibration coefficient. For a given calibration type, the mean and standard deviation of the calibration coefficient (\bar{N}_{S_K} and σ_{S_K} , respectively) were calculated from a population of all chambers of the same model. If a chamber underwent multiple calibrations, then the average calibration coefficient among the chamber's reported calibrations was used.

A chamber's stability was quantified by how subsequent calibration coefficients fluctuate across repeated calibrations. The mean, \bar{R}_{rep} and standard deviation, $\sigma_{R_{rep}}$, from the mean was calculated from repeated calibrations as,

$$R_{rep} = \frac{(N_{S_K})_{new}}{(N_{S_K})_{previous}}. \quad (1)$$

Additionally, the average that a chamber would deviate from its own mean, $\bar{\sigma}_{R_{rep}}$, was determined on an individual basis and averaged among all chambers of the same model.

Results: Table 2 lists the statistical results from the Ir-192 well chamber N_{SK} 's among several chambers. In addition to the basic statistical quantities, the 95 % quantile for a chamber's N_{SK} reproducibility among repeated calibrations, denoted as $Q_{95\%}$, is listed.

The lineage of a chamber model's manufacturing process may also influence the variability in the determined N_{SK} 's of a specific chamber model. Figure 1 illustrates the distribution of measured N_{SK} 's among 2,548 HDR1000 Plus well-type ionization chambers. The relationship between the lineage of a chamber model and the respective N_{SK} 's were assessed by plotting the median-normalized N_{SK} 's as a function of the chamber's manufacturing date.

Air-kerma strength calibration coefficient variability was quantified for each chamber that underwent at least three re-calibrations. The average of each chamber's N_{SK} re-calibration ratio with its prior calibration was assessed for a given well chamber model in addition to the average that a single chamber would vary about its own mean N_{SK} . A chamber's stability was quantified based on its 95 % quantile in addition to the standard deviation.

Conclusions and Significance: Widespread N_{SK} 's among chambers of the same model does not necessarily suggest that a chamber is not a precise instrument. While a chamber's accuracy is maintained through a NIST-traceable calibration, its precision is a factor of the chamber's measurement and calibration repeatability. The well-type ionization chambers studied in this work all showed an average stability to between 0.01 % to 1.05 % of their repeated N_{SK} 's, but the spread about these average values depended on the chamber type; the N_{SK} 's for pressurized chambers showed greater variance between subsequent calibrations than air communicating chambers. A retrospective analysis on the historical account of a well chamber's repeated calibrations show that their stability deviates within 0.2 % and 3.0 % for air-communicating and pressurized chambers, respectively, at the $k=1$ confidence level. However, the histograms and quantile analysis plotted in Figure 2 suggests that the stability of the chambers for a model are also not normally distributed.

While the stability around unity for the HDR1000 Plus well chamber is leptokurtic, resulting in a standard deviation within 0.15 % the expected stability, the tails of this distribution are broader and indicate that 5 % of customer chambers' N_{SK} 's may deviate up towards 0.42 % between calibrations. Thus, assuming that all well chambers retain their calibration coefficients over several years may not necessarily be true and should not be generalized from an instance of a single chamber's behavior, which has been the focus and scope of some works [7].

Project relevance to CIRMS and relevance of CIRMS to professional goals:

This presented work highlights the synergy between the UWADCL and their customers. Establishing NIST traceability is one of the greatest services an ADCL can provide to a clinical physicist to facilitate safe, efficacious medical care. Likewise, the continuing patronage from the clinical physicist towards the calibration services offered by the ADCL results in an archive of information that can be used to better the services from the ADCL and further progress the field of Medical Physics.

CIRMS has been a great venue to present my graduate research to the scientific community and actively participate within a national scientific organization as a student. As a recent graduate,

CIRMS will continue to be an important resource that promotes collaboration with other researchers and shape my research based on the prioritized needs of the scientific community.

References

- 1) W. Butler, W. Bice, L. DeWerd, J. Hevezi, M. Huq, F. Ibbott, J. Palta, M. Rivard, J. Seuntjens, and B. Thomadsen, "Third-party brachytherapy source calibrations and physicist responsibilities: Report of the AAPM Low Energy Brachytherapy Source Calibration Working Group," Medical Physics 35, 3860-3864 (2008).
- 2) R. Nath, L. Anderson, J. Meli, A. Olch, J. Stitt, and J. Williamson, "Code of practice for brachytherapy physics: Report of the AAPM Radiation Therapy Committee Task Group No. 56," Medical Physics 24, 1557-1598 (1997).
- 3) L. DeWerd, G. Ibbott, M. Mitch, M. Rivard, K. Stump, B. Thomadsen, and J. Venselaar, "A dosimetric uncertainty analysis for photon-emitting brachytherapy sources: Report of AAPM Task Group No. 138 and GEC-ESTRO," Medical Physics 38, 782-801 (2011).
- 4) S. Goetsch, F. Attix, D. Pearson, and B. Thomadsen, "Calibration of Ir-192 high-dose-rate afterloading systems," Medical Physics 18, 462-467 (1990).
- 5) B. Rasmussen, S. Davis, C. Schmidt, J. Micka, and L. DeWerd, "Comparison of air-kerma strength determinations for HDR Ir-192 sources," Medical Physics 38, 6721-6729 (2011).
- 6) B. Muir, "Ion chamber absorbed dose calibration coefficients, NDw, measured at ADCLs: Distribution analysis and stability," Medical Physics 42, 1546-1554 (2015).
- 7) S. Vandana and S. Sharma, "Long term response stability of a well-type ionization chamber used in calibration of high dose rate brachytherapy," Journal of Medical Physics 35, 100-103 (2010).
- 8)

Table 1. A list of well-type ionization chambers that have been analyzed in this study across the range of calibration dates.

| Manufacturer | Chamber model | Type | Number | Calibrations | Dates |
|------------------|---------------|-------------|--------|--------------|-----------|
| Nucletron | 077.091 | ventilated | 11 | 27 | 1998-2018 |
| Nucletron | 077092 | ventilated | 17 | 28 | 2010-2019 |
| Standard Imaging | IVB1000 | ventilated | 492 | 2773 | 2000-2019 |
| Standard Imaging | HDR1000 | ventilated | 149 | 541 | 1996-2019 |
| Standard Imaging | HDR1000 Plus | ventilated | 3523 | 13864 | 1996-2019 |
| PRM | WC-2 | ventilated | 27 | 99 | 1996-2019 |
| Sun Nuclear | 1008 | pressurized | 33 | 83 | 1996-2008 |
| Sun Nuclear | 100840 | pressurized | 8 | 53 | 2001-2019 |
| Atomlab | 44D | pressurized | 111 | 547 | 1996-2019 |
| Capintec | BTC/3007 | pressurized | 9 | 23 | 2004-2019 |

Table 2. Statistical results of archived HDR Ir-192 S_K calibrations for well chambers sorted by their air-communication status. Row entries are shaded for pressurized chambers.

| Model | Cham | Number of Cals | RCals | \bar{N}_{S_K} | $\sigma_{S_K}(\%)$ | \bar{R}_{rep} | $\sigma_{R_{rep}}(\%)$ | $\bar{\sigma}_{R_{rep}}(\%)$ | $Q_{95\%}(\%)$ |
|--------------|------|-------------------|-------|-----------------|--------------------|-----------------|------------------------|------------------------------|----------------|
| 077.091 | 11 | 26 | 5 | 1.986 | 0.53 | 0.9996 | 0.17 | 0.14 | 0.50 |
| 077092 | 17 | 27 | 6 | 2.016 | 1.86 | 1.0002 | 0.15 | 0.09 | 0.27 |
| HDR1000 | 120 | 430 | 66 | 1.076 | 3.31 | 0.9997 | 0.27 | 0.13 | 0.44 |
| HDR1000 Plus | 2548 | 7885 | 1278 | 1.000 | 1.72 | 1.0001 | 0.25 | 0.15 | 0.42 |
| IVB1000 | 100 | 324 | 64 | 0.962 | 0.54 | 1.0004 | 0.71 | 0.19 | 0.59 |
| 1008 | 14 | 24 | 5 | 0.302 | 3.32 | 0.9986 | 0.89 | 2.95 | 5.26 |
| 100840 | 5 | 31 | 5 | 0.319 | 7.32 | 1.0024 | 2.04 | 2.40 | 4.18 |
| 44D | 47 | 166 | 32 | 0.312 | 8.43 | 1.0105 | 1.13 | 1.51 | 3.40 |

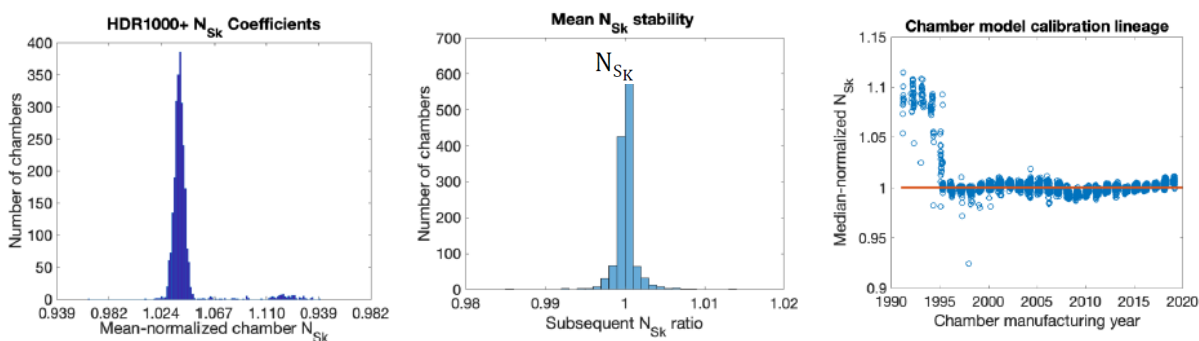


Figure 1. Distributions of median-normalized customer N_{Sk} 's, repeated calibration ratio stability for the HDR1000 Plus well chamber, and the chamber model's calibration trends over time.

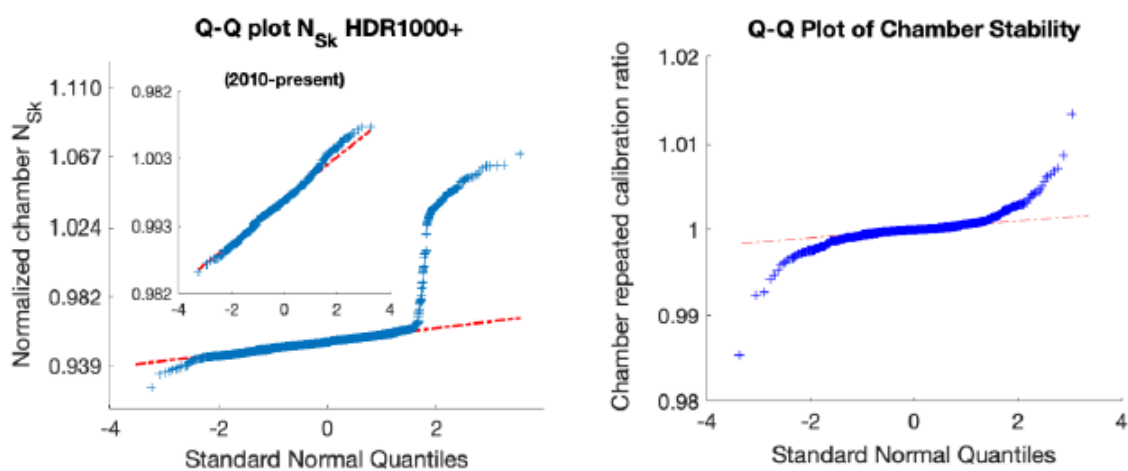


Figure 2. Quantile-quantile plots testing the normality of the customer N_{Sk} 's and stability distributions shown in Figure 1.

Proffered Abstracts from 2021 Virtual Meeting

A compact storage phosphor dosimeter attachable to smart phones for widely deployable radiation monitoring and measurements

Dongyuan He^{1,2} and Zhitao Kang^{1,3}

¹*Georgia Tech Research Institute, Georgia Institute of Technology, Atlanta, GA,*
zhitao.kang@qtri.gatech.edu

²*School of Electrical and Computer Engineering, Georgia Institute of Technology, Atlanta, GA*

³*School of Materials Science and Engineering, Georgia Institute of Technology, Atlanta, GA*

A novel design of radiation dosimeter is accomplished with a storage phosphor plate, a red LED, and a smartphone camera. The storage phosphor material (BaFBr:Eu) is used to capture energy from gamma rays, x-rays, beta particles and even alpha particles. The radiation energy is trapped in the material as excited electrons and then released as near-UV light emission upon photo-stimulation with a red LED. Readout of the radiation signature is accomplished by imaging the emitted light using the smartphone back camera. The near-UV light intensity and persistence time upon red light stimulation both behave as a function of the exposed radiation dosage. As the smartphone captures the emission intensity in real-time as images, these can be used to correlate back to the initial exposed radiation dosage. The energy stored in the storage phosphor will be erased during photo-stimulation so the device can be reset for continued use. The physical sensor can be made at low cost as a compact and discrete attachment for smartphones, such as an integrated sensor inside of a smartphone protection case. Unlike current, commercial active dosimeters for radiation monitoring and measurements, this sensor records radiation exposure continuously without the need of a power supply during monitoring. In comparison to passive dosimeters requiring complicated readout systems, this device achieves instant readout and fast reset once power is supplied from the smartphone or a battery. The sensor can be widely deployable as phone attachments to civilians or soldiers, and the recorded data can be wirelessly transmitted to location-mapped databases for national security and environmental monitoring applications.

Rapid HPGe well detector gamma bioassay of ^{137}Cs , ^{60}Co , and ^{192}Ir method

Jonathan Button and Robert L. Jones

Inorganic and Radiation Analytical Toxicology Branch Centers for Disease Control and Prevention 4770 Buford Highway, Mail Stop S103-1, Atlanta, GA, ndi7@cdc.gov

CDC designed a rapid HPGe Bioassay Method for ^{137}Cs , ^{60}Co , and ^{192}Ir that is suitable for a public health response to a radiological incident where people may ingest or inhale radionuclides. The method uses a short count time, small sample volume, and a large volume detector and well size. It measures a patient's urine sample collected post-incident. The levels of concern are directly related to the Clinical Decision Guide levels recommended in the National Council of Radiation Protection (NCRP) document 161. We describe method details such as analytical instrumentation, instrumentation automation, analytical method parameters, analytical accuracy, precision, range, limits of detection, throughput, and multi-instrument comparisons. This analytical method will be used in a public health response to identify and quantify gamma emitting radionuclides in potentially contaminated persons. These measurements will be used directly in dose calculations and to prioritize medical management based on the NCRP 161 guidance.

High energy X-ray fruit irradiation qualification with Monte Carlo code

Ludovic Eychenne¹, François Vander Stappen², Florent Kuntz³, Frédéric Stichelbaut², Cédric Dossat¹, Nathalie Chatry¹

¹TRAD Tests & Radiations, 907 L'Occitane, 31670 Labège, France, ludovic.eychenne@trad.fr

²IBA: 3 Chemin du Cyclotron, 1348 Louvain-la-Neuve, Belgium

³Aerial: 250 Rue Laurent Fries, 67400 Illkirch-Graffenstaden, France

In nuclear and medical fields, Monte Carlo simulations are commonly used to make validations (radioprotection, radiotherapy, etc.). In this study, we have considered the relevance of using Monte Carlo codes for industrial radiation processing. We carried out a feasibility study for phytosanitary treatment of a pallet of fruits by X-ray irradiation. Monte Carlo simulations were performed, using MCNPX code and RayXpert[®] software. We have determined the dose distribution throughout the irradiated product. Also, we focused on the analysis of the absorbed dose uniformity, by calculating Dose Uniformity Ratios (DUR). We also have studied the impact of the radiation source definition strategy (use of double-sided source or one single-sided source making translation steps and rotation). An experimental dose mapping study of this pallet of fruits was also performed. It determines the dose distribution throughout the product container by placing enough dosimeters in and around the product load. The good agreement between the Monte Carlo simulation results and the dose mappings leads us to consider the use of Monte Carlo codes for the calculation of the dose distribution in an irradiated product in order to qualify the process.

Low-energy, high-production x-ray for food irradiation and sterilization

Michael Fletcher and Sage Schissel

PCT Ebeam and Integration, Davenport, IA, pmfletcher@teampct.com

Food illness and food waste are costly problems that can be solved, in part, through the use of food irradiation. Food irradiation is an effective microbial inactivation process for a variety of solid and liquid foods. Most irradiated food is processed in gamma irradiation facilities. Other technologies, such as ebeam and x-ray, have lagged behind due to gamma irradiation's ability to efficiently process large pallets of material and its establishment in the industry; however, gamma irradiation requires a radioactive source, its regular replenishment, and the process can negatively affect the taste, texture, and aroma of some foods. Low-energy, high-production (L.E.H.P.) x-ray processing is a newly developed option for food irradiation and other applications of microbial inactivation and sterilization. The high throughput of L.E.H.P. (with machine power up to 600 kW) makes it a viable in-line alternative to gamma irradiation, and the process has been shown to leave key nutrients unaffected. Additional benefits and challenges of the L.E.H.P. technology will be presented.

A kinetic model of CH₄ conversion into H₂ and hydrocarbons by electron beam irradiation

Weiyao Gu and Theodore S. Dibble

State University of New York College of Environmental Science and Forestry, Syracuse, NY,
wgu100@syr.edu

We built a chemical kinetic model for the electron beam irradiation of methane and report results of simulations with a dose rate ranging from 2 to 200 kGy/sec at room temperature and 1 atm pressure. The model contains 91 species and 778 gas-phase reactions. We report the time evolution of concentrations of H₂ and hydrocarbons as well as some radicals and ions. G-values of major products are in good agreement with previous experimental results. The dependence of G values on dose rate and time will be discussed. We quantify the extent to which various reactions produce and destroy major products, with multiple reactions are responsible for H₂ production, but only one reaction dominates C₂H₆ production ($\text{CH}_3 + \text{CH}_3 + \text{M} \rightarrow \text{C}_2\text{H}_6 + \text{M}$). Normalized sensitivity coefficients are computed for the production of stable products. We perform a mechanism reduction to rank which chemical steps are most important to the least important. Future work will be focused on the conversion of CH₄/CO₂ mixture into commodity chemicals.

Radiation measurements for dosimetry with ionization chambers and hybrid pixel detectors

Jürgen Roth and Patrik Kramer

PTB, Fachbereich 6.3, Germany, juergen@kaeppner-roth.net

Ionization Chambers have been the proven standard for radiation protection measurements for many years. Discrete measurements of dose are realized at PTB using in-house developed electrometers and measurement routines that allow current measurements down to some femtoamperes. These traditional and well proven current measurements will be compared to the results of recent measurements carried out with hybrid pixel detectors which offer a time resolution of nanoseconds and 55 μm spatial resolution. The confrontation will focus especially on the expanse of information gathered from signals and its technical applicability in continuous and pulsed radiation fields.

Under certain circumstances Ionization chambers can produce linear relationships between the collected charge of ionization events and radiation dose. This can be realized over a broad range of incident radiation energies within the accepted response range of IEC61526. Most of these ICs measure with air at ambient atmospheric pressure and as a result the ionization currents can become very low. The PTB has therefore developed highly sensitive electrometers. These instruments and the limits of certain measurements will be presented.

Nowadays, by the reason of cost and applicability for active dosimeters, many detectors are based on semiconductor technology. The Timepix3 detector is one such detector equipped with an active pixel ASIC capable of detecting up to 40E6 radiation events per second. The capabilities and possibilities for this detector in relation to dose measurements will be shown by exemplary applications.

Dosimetry auditing in the time of COVID: Overcoming border closures through relocation and remote auditor support

Andrew Alves¹, Fayz Kadeer¹, Andrew Cole¹, Maddison Shaw¹, Rhonda Brown¹, Ivan Williams²

¹*Australian Clinical Dosimetry Service, ARPANSA, Melbourne, Victoria, Australia,*
Andrew.Alves@arpansa.gov.au

²*Australian Radiation Protection and Nuclear Safety Agency, Melbourne, Victoria, Australia*

The ACDS provides clinical dosimetry and auditing services to 107 radiotherapy centers (224 linacs) across Australia and New Zealand. These services are essential in testing and maintaining a high level of operational safety for both staff and patients. In many cases, ACDS reports are required in order to participate in clinical trials and perform highly specialized treatment modalities. The COVID pandemic caused border closures and restricted access to health care facilities which created challenges in performing on-site audits. In order to continue providing our services, four staff members spent a combined 10 weeks in isolation and two staff members temporarily moved out of state (Victoria) for four months so that audits could be performed in both Queensland and Western Australia.

ACDS protocol requires at least two staff members to perform an audit on-site, however, with limited access and public exposure a health risk, the ACDS performed audits with one staff member participating via video conferencing. The video conferencing led to some minor inconvenience for the site auditor who was required to perform all manual tasks unaided, however, the benefit of two auditors (checking data entry and in audit process troubleshooting) remained intact with one remote auditor. Additionally, there was a benefit to the remote component in that, audit data was secured to the ARPANSA network with ease by the remote auditor, leaving the on-site staff member to focus on managing the ACDS equipment.

By working with the challenges COVID created, the ACDS performed 86 audits in 2020 (42 OSLD mail-out and 44 on-site). This was almost 77% of the number of audits performed in 2019 (see Figure 1). During this time, the ACDS also implemented a new dose-to-bone and dose-to-lung correction in the audit data analysis, as well as made progress in developing a new motion adaptive auditing program.

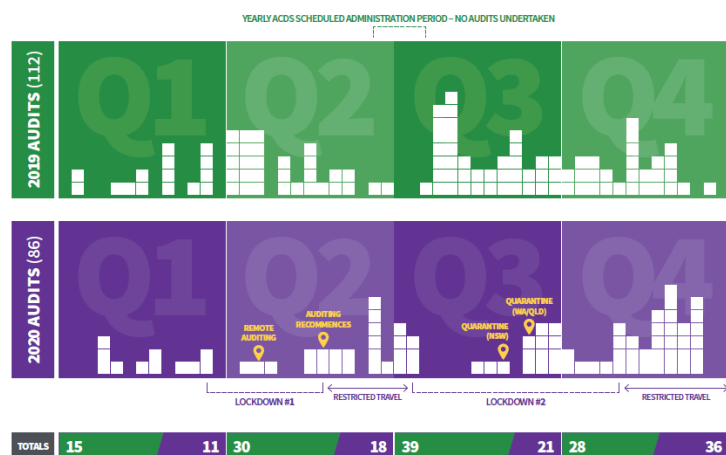


Figure 1. ACDS audit comparison between 2019 and 2020, highlighting the disruption to the on-site audit schedule from Covid-19 lockdowns in Victoria and periods of restricted cross-border travel.

Design of operational radiation protection in commissioning of compact proton therapy centers (CPTC)

Gonzalo F. García-Fernandez¹, Alejandro Carabe-Fernández², Alejandro Bertolet-Reina³, Hector R. Vega-Carrillo⁴, Karen A. Guzman-García⁴, Lenin E. Cevallos-Robalino⁵, Jose M. Gomez-Ros⁶, Eduardo Gallego¹

¹*Departamento de Ingeniería Energética, ETSI Industriales, Universidad Politécnica de Madrid (UPM), Spain, gf.garcia@upm.es*

²*Medical Physics, Hampton University Proton Therapy Institute (HUPTI), Hampton, VA, USA*

³*Physics Research, Massachusetts General Hospital (MGH), Boston, MA, USA*

⁴*Unidad Académica de Estudios Nucleares, Universidad Autónoma de Zacatecas (UAZ), Mexico*

⁵*Grupo de Investigación en Sistemas de Control y Robótica, GISCOR, Universidad Politécnica Salesiana (UPS), Guayaquil, Guayas, Ecuador*

⁶*Centro de Investigaciones Energéticas, Medioambientales y Tecnológicas (CIEMAT), Madrid, Spain*

Proton therapy (PT), the external radiotherapy using proton beams to treat some type of tumors with outstanding benefits, is in continuous ever evolving to improve its performance. Some prominent current trends involve cutting-edge delivery methods or building compact centers. New developments have direct impact in radiation protection of facilities, and compact centers take in specific features to reduce their size while achieving more affordable facilities: usually have one single room and small footprint, higher radiation density, or mix of professional exposed workers (clinical and technical staff), among others.

This work is framed into the research project *Contributions to operational radiation protection and neutron dosimetry in compact proton therapy centers (CPTC)*, which is focused on assessing the operational radiation protection (RP) and commissioning of these facilities. The project has been developed by researchers from six institutions in four countries, Spain, USA, Mexico and Ecuador. Thus, several tasks have been carried out over the last three years in fields as checking shielding, comparing ambient dose yielded by neutrons in several CPTC, analyzing activation in shielding with different types of concrete, characterizing wide range Rem-meters to measure neutron fields, studying new proton delivery techniques and their neutron fields, or assessing personal dosimeters suitable for CPTC.

The main goal of the work is to present the activities developed from 2018 until now, in designing the operational radiological protection of CPTC. The current and new proton delivery methods compared in the yielding of neutron fields were IMPT (Intensity Modulated Proton Therapy), PMAT (Proton Monoenergetic Arc Therapy), and flash-therapy (just simulation). Experimental measurements of stray neutron fields were carried out at the Roberts Proton Therapy Center (RPTC), part of the Abramson Cancer Center at Perelman, Hospital of the University of Pennsylvania, from December 2019 to July 2020. Experimental set-up of measurements is collected in Figure.

Acknowledgements: This work has been developed under the Industrial Doctorate Program, IND2017/AMB-7797, *Contributions to operational radiation protection and neutron dosimetry in compact proton therapy centers (CPTC)*, funded by Madrid Autonomous Region (CM), Spain.

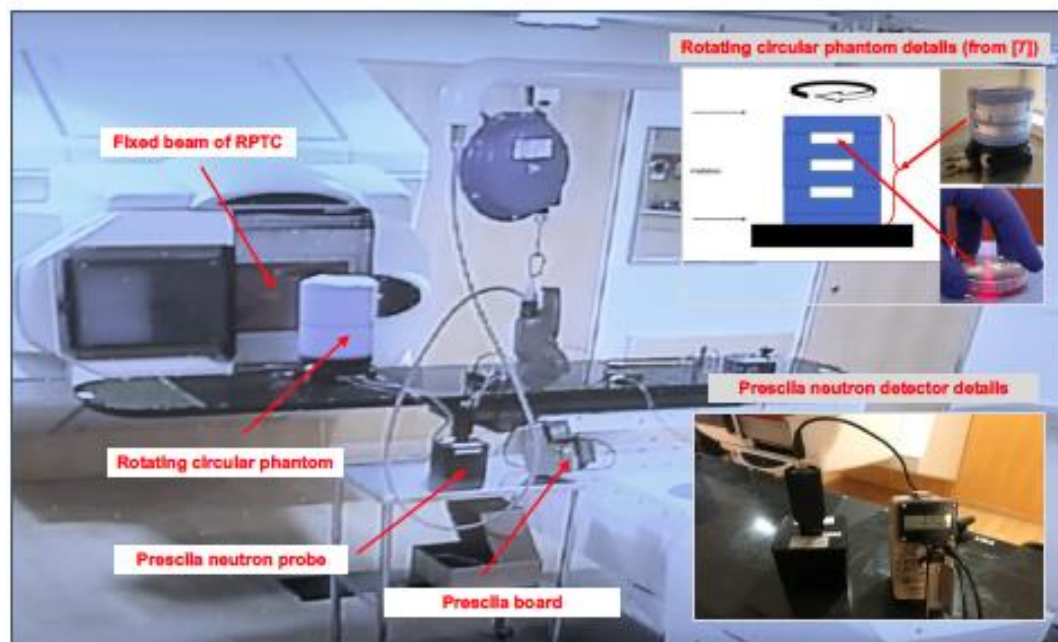


Figure 1. Experimental setup of arc therapy delivery method (PMAT) at Roberts Proton Therapy Center (UPenn)

Ne-22 Ion-beam radiation damage to DNA: From initial free radical formation to resulting DNA-base damage

Melis Kant¹, Pawel Jaruga¹, Erdem Coskun^{1,2}, Samuel Ward³, Alexander D. Stark³, Thomas Baumann⁴, David Becker³, Amitava Adhikary³, Michael D. Sevilla³ and Miral Dizdaroglu¹

¹*Biomolecular Measurement Division, National Institute of Standards and Technology, Gaithersburg, MD*

²*Institute for Bioscience & Biotechnology Research, University of Maryland, Rockville, MD*

³*Department of Chemistry, Oakland University, Rochester, MI, adhikary@oakland.edu*

⁴*National Superconducting Cyclotron Laboratory, Michigan State University East Lansing, MI*

We report on the physicochemical processes and the products of DNA damage involved in Ne-22 ion-beam radiation of hydrated (12 ± 3 H₂O/nucleotide) salmon sperm DNA at 77 K. Free radicals trapped at 77 K were identified using electron spin resonance (ESR) spectroscopy. The measurement of DNA damage by two different techniques of mass spectrometry revealed the formation of numerous DNA products. Results obtained by ESR spectroscopy showed that, as the linear energy transfer (LET) of the ion-beam radiation increases along the beam track, the production of DNA radicals correspondingly increases until just before Bragg peak is reached. Yields of DNA products along the ion-beam track were in excellent agreement with the radical production. This work is the first to use the combination of ESR spectroscopy and mass spectrometric techniques enabling a better understanding of mechanisms of radiation damage to DNA by heavy ion-beams detailing the formation of DNA free radicals and their subsequent products.

Supported By: National Cancer Institute of the National Institutes of Health (Grant RO1CA045424), REF, CBR at OU, the National Superconducting Cyclotron Laboratory (NSCL) at Michigan State University, National Science Foundation under Grant No. CHE- 1920110. The operation of the National Superconducting Cyclotron Laboratory at Michigan State University is supported by the NSF under grant PHY-1565546.

Number of replacement of oxygen atom by sulfur in the phosphate group dictates the directionality of hole transfer between base and backbone

Sergey A. Denisov¹, Samuel Ward², Viacheslav Shcherbakov¹, Renata Kaczmarek³, Dipra Debnath², Taisiya Jacobs², Alexander D. Stark², Dariusz Korczyński³, Anil Kumar², Michael D. Sevilla², Pascal Pernot¹, Roman Dembinski^{2,3}, Mehran Mostafavi³, Amitava Adhikary²

¹*Institut de Chimie Physique, UMR 8000 CNRS/Université Paris-Saclay, Bât. 349, Orsay 91405 Cedex, France*

²*Department of Chemistry, Oakland University, 146 Library Drive, Rochester, Michigan 48309-4479, USA, adhikary@oakland.edu*

³*Centre of Molecular and Macromolecular Studies, Polish Academy of Sciences, Sienkiewicza 112, 90-363 Łódź, Poland*

Investigation of hole transfer processes between the DNA-backbone and -base of phosphorodithioate-modified components were carried out using 5'-O-methoxyphosphorothioyl-2'-deoxyguanosine (G-P(O⁻)=S), dimethylphosphorothioate (DMTP(O⁻)=S), 5'-O-methoxyphosphorodithioyl-2'-deoxyguanosine (G-P(S⁻)=S), and ammonium O,O'-diethyl dithiophosphate (DETP(S⁻)=S) models and employing electron spin resonance (ESR) spectroscopy in homogeneous frozen aqueous solutions, pulse radiolysis in aqueous solution at ambient temperature, and density functional theory (DFT) calculations. Electrophilic addition of Cl₂•⁻ to DMTP(O⁻)=S and to G-P(O⁻)=S leads to the formation of a two-center three-electron $\sigma^2\sigma^{*1}$ bonded adduct radical (-P-S-Cl) along with elimination of Cl⁻. In DMTP(O⁻)=S, -P-S-Cl reacts with a neighboring phosphorothioate to form the $\sigma^2\sigma^{*1}$ bonded disulphide anion radical ([-P-S-S-P]⁻). However, contrary to these ESR results, pulse radiolysis of these compounds shows formation of thiyl radicals (P-S•) and dimerization of these radicals leading to neutral dimer formation thereby correcting the interpretation of a recent laser flash photolysis study (Su and co-workers, *Nucleic Acids Res.*, 2019, 1, doi:10.1093/nar/gkz987). However, ESR, pulse radiolysis and theory show dithiyl radical (P-2S•) formation by one-electron oxidation of DETP(S⁻)=S. DFT calculations showed that spin density is delocalized equally over both sulfurs in P-2S•. The ionization potential of G-P(O⁻)=S was calculated to be higher and that of G-P(S⁻)=S was calculated to be slightly lower than that of guanine in 5'-dGMP. For G-P(O⁻)=S, ESR shows that the (-P-S-Cl) oxidizes guanine at low temperature and pulse radiolysis evidences facile intramolecular one-electron oxidation of guanine by P-S• in sub-nanosecond timescale. ESR and pulse radiolysis confirmed initial formation of G•⁺-P(S⁻)=S. Subsequent thermally activated hole transfer from G•⁺ to P(S⁻)=S led to P-2S• formation on μ s timescale. ESR investigations at low temperatures and higher G-P(S⁻)=S concentrations showed a bimolecular conversion of P-2S• to the $\sigma^2\sigma^{*1}$ -bonded dimer anion radical [-P-2S-S-2S-P]⁻ [ΔG (150 K, DFT) = -7.2 kcal/mol]. However, [-P-2S-S-2S-P]⁻ formation was not observed by pulse radiolysis [ΔG (298 K, DFT) = -1.4 kcal/mol] due to the positive entropy facilitating dissociation of the weak S-S bond. Neither P-2S• nor [-P-2S-S-2S-P]⁻ oxidized guanine base; hence, hole transfer occurs from the backbone (P-(O⁻)=S) to base in phosphorothioate-incorporated DNA and from base to backbone (P-(S⁻)=S) in phosphorodithioate-incorporated DNA. Thus, the directionality of hole transfer between base and backbone is crucially controlled by the number of sulfur substitution in the phosphate group.

Comprehensive beam characterization and feedback for FLASH-RT using radioluminescent dosimeters

M. Ramish Ashraf¹, Mahbubur Rahman¹, Rongxiao Zhang^{1,2,3}, Benjamin B. Williams^{1,2,3}, David J. Gladstone^{1,2,3}, Brian W. Pogue^{1,3,4}, Petr Bruza¹

¹*Thayer School of Engineering, Dartmouth College, Hanover, NH,*

Ramish.Ashraf.TH@dartmouth.edu

²*Department of Medicine, Radiation Oncology, Geisel School of Medicine, Dartmouth College Hanover, NH*

³*Norris Cotton Cancer Center, Dartmouth-Hitchcock Medical Center, Lebanon, NH*

⁴*Department of Surgery, Geisel School of Medicine, Dartmouth College, Hanover NH*

Purpose: High dose-rate conditions make dose characterization for FLASH-RT challenging. Most conventional dosimeters show significant dependence on dose rate at ultra-high dose rate conditions or fail to provide sufficiently fast temporal data for pulse to pulse dosimetry. In this study fast 3D imaging of radioluminescence from a water and quinine phantom was tested for dosimetry of single 4 μ s linac pulses.

Methods: The modified clinical linac delivered a radially symmetric electron FLASH beam of >300 Gy/s to the clinical isocenter. Lateral projected 2D dose distributions for each 4 μ s linac pulse were imaged in a quinine-doped water tank using a gated intensified camera, and an inverse Abel transform reconstruction provided 3D images for on-axis depth dose values. The central axis depth dose values were used to quantify beam metrics for individual pulses and compared against film data. System architecture and timing mechanisms were identified for the embedded controller.

Results: The R_p , D_{max} and the R_{50} measured with film and camera based optical method agreed to within 1 mm for a 1.5 cm circular beam and the beam with jaws wide open. Cross beam profiles for both beams agreed with film data with > 95 % passing rate (2%/2mm gamma criteria). A temporal pulse analysis by the camera revealed a ramp-up period where the dose per pulse increased for the first few pulses and then stabilized.

Conclusions: Optical imaging of radioluminescence was presented as a valuable tool for establishing a baseline for the recently initiated electron FLASH beam at our institution. Currently, a point-based scintillator dosimeter is being evaluated in conjunction with a FPGA-based embedded controller and a gated integrator for providing feedback to the modified clinical linac on a pulse by pulse basis.

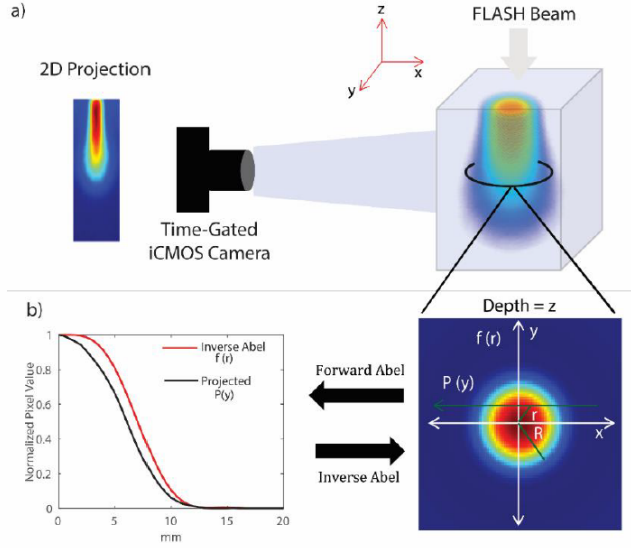


Figure 1 a) Schematic of the experimental setup showing the 1.5 cm beam imaged with the time-gated intensified camera. b) Circular symmetry of the beam at a specific depth z . An inverse Abel transform (equation 2) can be employed to reconstruct the 2D cross-section (equation 1) of the beam at each depth for a 3D volume.

$$P(y) = 2 \int_y^R f(r) \frac{r}{\sqrt{r^2 - y^2}} dr \quad (1)$$

$$f(r) = -\frac{1}{\pi} \int_r^R \frac{dP(y)}{dy} \frac{1}{\sqrt{y^2 - r^2}} dy \quad (2)$$

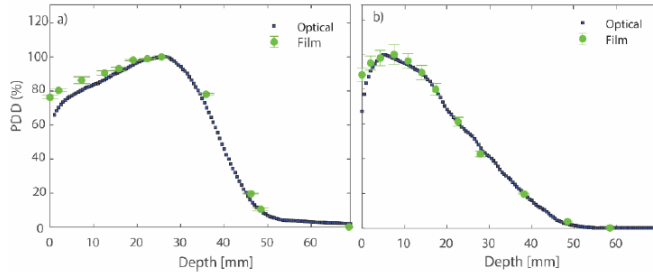


Figure 2 a) and b) Comparison of central axis percentage depth dose (PDD) between optical and film for the broad and small beam, respectively. The error bars on the film data represent standard deviation from three different measurements.

Table 1: Comparison of Depth Dose Characteristics between Optical and Film Data

| | $D_{max}(mm)$ | | $R_{50}(mm)$ | | $R_p(mm)$ | |
|-----------|----------------|----------------|----------------|----------------|----------------|----------------|
| | Optical | Film | Optical | Film | Optical | Film |
| Jaws Open | 25.0 ± 0.3 | 26.0 ± 0.3 | 39.0 ± 0.3 | 40.0 ± 0.3 | 48.0 ± 0.2 | 48.0 ± 0.2 |
| 1.5 cm | 8.0 ± 0.5 | 8.0 ± 0.2 | 26.0 ± 0.9 | 26.0 ± 0.1 | 41.0 ± 0.8 | 40.0 ± 0.1 |

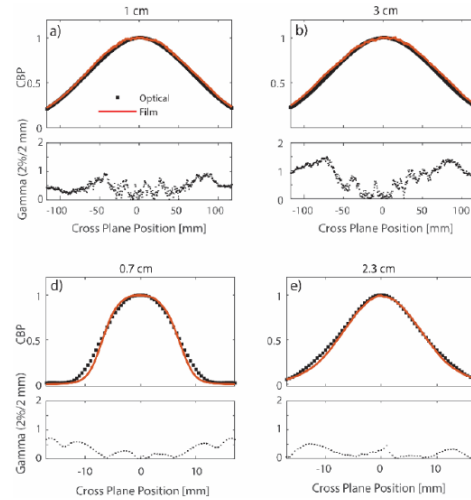


Figure 3) Comparison of optical and film based central axis cross beam profiles at different depths for the jaws wide open and the 1.5 cm diameter field. At each depth, the optical data is compared to film using the gamma criteria of 2%/2mm.

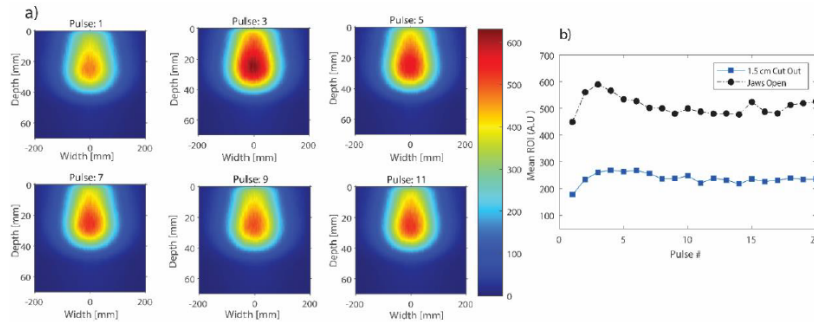


Figure 4. a) 2D projected images of individual linac pulses for the jaws wide open beam. Only 6 pulses are shown here. b) shows the data acquired with a PMT coupled to a fiber optic.) Beam intensity variation for the broad and small beam. The mean pixel value was obtained from a region of interest (ROI) near the point of

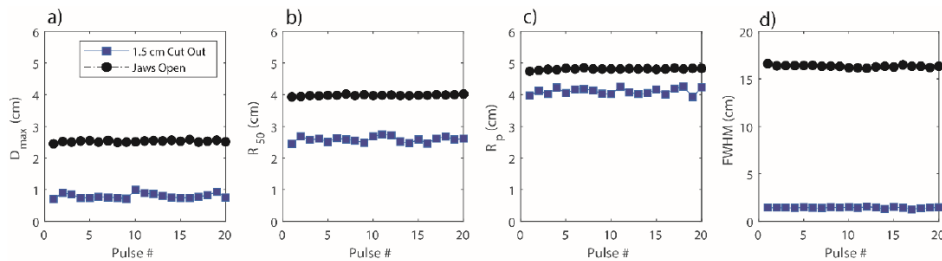


Figure 5. a-d) Variation in D_{max} , R_{50} , R_p and FWHM at D_{max} , respectively for the small and broad beam over the course of 20 pulses.

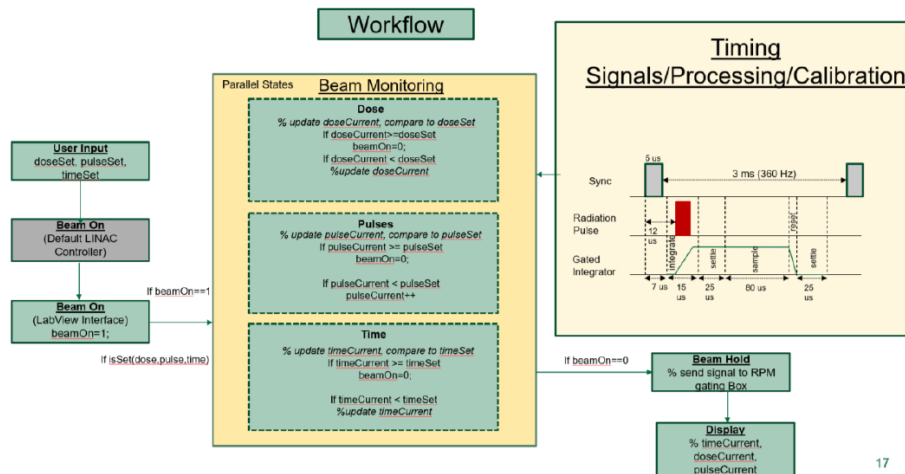


Figure 6) Workflow for the feedback system for the modified linac. The ramp-up period signifies the importance of integrating dose per pulse and not just counting pulses. To this end, a FPGA based controller in conjunction with a point based scintillation dosimeter and gated integrator is being currently investigated. The yellow box denotes the dose-read out scheme for the gated integrator.

Quantifying the effects of beam and tissue properties on reemitted Cherenkov light during external beam irradiation

Savannah M. Decker¹, Daniel A. Alexander¹, Rachael L. Hachadorian¹, Rongxiao Zhang^{1,3,4}, David J. Gladstone^{1,3,4}, Petr Bruza^{1,2}, Brian W. Pogue^{1,2,4}

¹*Thayer School of Engineering, Dartmouth College, Hanover, NH,*
savannah.m.decker.th@dartmouth.edu

²*DoseOptics LLC, Lebanon, NH*

³*Department of Medicine, Geisel School of Medicine, Dartmouth College, Hanover, NH*

⁴*Norris Cotton Cancer Center, Dartmouth-Hitchcock Medical Center, Lebanon, NH*

Purpose: As Cherenkov light is generated within tissue during radiation therapy following the dose build-up, studies have shown that the reemitted Cherenkov light provides a way to visualize treatment delivery in real-time [1–5]. Many factors affect the amount of Cherenkov light that escapes the beam entrance surface of a patient. Understanding the magnitude of these factors can lead to a quantitative calibration to the imaged Cherenkov light as proportional to the superficial dose.

Methods: The reemitted Cherenkov signal was measured as a function of surface dose, dose build-up slope, and tissue optical properties. Diffuse liquid tissue phantoms of various scattering and absorption properties within the range of human tissue were irradiated at 200 MU with 6, 10, and 18 MV x-rays. Each phantom was imaged with a fixed intensified camera, and irradiated top-down at the entrance surface, as well as underneath at the exit surface.

Results: Due to a higher surface dose and steeper dose build-up, a low energy beam yields a greater reemitted Cherenkov signal per unit dose, a ~46% increase at 6 versus 18 MV. However, higher x-ray energies generate more Cherenkov light per dose [6], and this increase in photons resulted in a ~44% increased signal at 18 versus 6 MV. The result of these competing effects was a nearly constant reemitted Cherenkov signal from the surface of the phantoms regardless of beam energy. With different phantoms, the reemitted Cherenkov signal increased ~10% and decreased ~20% with varying scattering and absorption tissue optical properties, respectively.

Conclusions: This study provided an explanation as to why the reemitted Cherenkov signal during radiation therapy is not strongly dependent on beam energy, despite greater Cherenkov photon generation at higher energies. Quantifying the effects of beam and tissue properties is a progressive step towards verifying dose delivery during radiation therapy treatments in real-time.

References

- 1) Black PJ, Velten C, Wang Y-F, Na YH, Wu C-S. An investigation of clinical treatment field delivery verification using cherenkov imaging: IMRT positioning shifts and field matching. *Med Phys.* 2019;46(1):302-317. doi:<https://doi.org/10.1002/mp.13250>
- 2) Hachadorian RL, Bruza P, Jermyn M, Gladstone DJ, Pogue BW, Jarvis LA. Imaging radiation dose in breast radiotherapy by X-ray CT calibration of Cherenkov light. *Nat Commun.* 2020;11. doi:10.1038/s41467-020-16031-z
- 3) Jarvis LA, Zhang R, Gladstone DJ, et al. Cherenkov video imaging allows for the first visualization of radiation therapy in real time. *Int J Radiat Oncol Biol Phys.* 2014;89(3):615-622. doi:10.1016/j.ijrobp.2014.01.04
- 4) Jarvis LA, Hachadorian RL, Jermyn M, et al. Initial Clinical Experience of Cherenkov Imaging in External Beam Radiation Therapy Identifies Opportunities to Improve Treatment Delivery. *Int J Radiat Oncol Biol Phys.* 2020;0(0). doi:10.1016/j.ijrobp.2020.11.013
- 5) Miao T, Bruza P, Pogue BW, et al. Cherenkov imaging for linac beam shape analysis as a remote electronic quality assessment verification tool. *Med Phys.* 2019;46(2):811-821. doi:10.1002/mp.13303
- 6) Glaser AK, Zhang R, Gladstone DJ, Pogue BW. Optical dosimetry of radiotherapy beams using Cherenkov radiation: the relationship between light emission and dose. *Phys Med Biol.* 2014;59(14):3789-3811. doi:10.1088/0031-9155/59/14/37

Characterization of phosphorescent strontium aluminate as a real-time dosimeter

S. Drehmel, D. Mathew, E. Ehler

Department of Radiation Oncology, University of Minnesota, Minneapolis, MN,
drehm014@umn.edu

This research highlights the potential for a low-cost relative dosimeter that could function in real-time during irradiation. Real-time information on the distribution of dose would verify whether the target is truly being treated and areas at risk are being avoided, thus, improving radiation treatment accuracy. The purpose of this study was to characterize the response of phosphorescent strontium aluminate ($\text{SrAl}_2\text{O}_4:\text{Eu}^{2+}\text{Dy}^{3+}$) to high energy x-rays and to subsequently determine how the signal decays with respect to time. The wide range of application and low cost makes it a promising alternative to relative dosimetry. Future work will explore its wide range of potential application in common HDR QA protocols. We have already shown that it can verify light to radiation field coincidence and be reused, dramatically cutting the cost of current film solutions. This could be primarily useful for underfunded clinics such as rural/veterinary cancer centers. Lastly, we intend on further characterizing its dependence on energy, dose rate, and the effect our detector has on the signal.

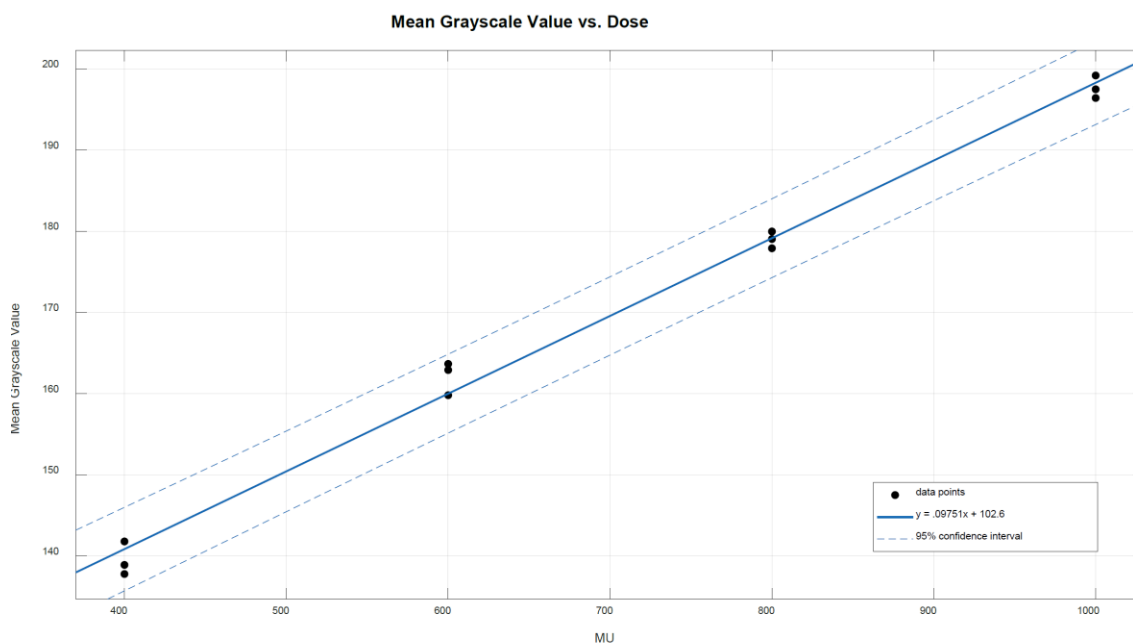


Figure 1. Mean grayscale value (green channel) vs. Dose. Three separate trials are plotted with a linear fit within 95% confidence intervals, and an R-square value of .9922. The dynamic linear range was found to be from 400 to 1000 MU.)

Investigating the accuracy of a general cavity theory through Monte Carlo simulations

Matthew Efseaff¹, Daniel J La Russa¹, Miller MacPherson^{1,2,3}

¹Dept. of Physics, Carleton University, Ottawa, ON, K1S5B7, mefseaff@physics.carleton.ca

²Dept. of Radiology, University of Ottawa, ON, K1N6N5

³Radiation Medicine Program, The Ottawa Hospital, ON, Canada

Purpose: To evaluate the accuracy of a novel general cavity theory that is formulated to explicitly account for the effects of the cavity on the charged particle fluence in the surrounding medium. Of particular interest is the accuracy over the range of incident beam energies and detector configurations where traditional cavity theory formalisms are known to be unreliable.

Methods: The EGSnrc Monte Carlo (MC) code was used to calculate the dose to the cavity of an idealized plane-parallel ion chamber (1-cm radius) free-in-air exposed to incident photon beams. Calculations were performed for various incident photon beam energies, chamber wall materials, cavity sizes (0.1 to 10 mm cavity heights), and threshold energies for creating and tracking charged particles (1 to 10 keV) which, together, form a set of benchmark calculations that serve as the basis for comparison. Using a consistent set of interaction cross-sections, stopping powers, and transport parameters the EGSnrc code was also used to calculate charged particle spectra in homogeneous media and chamber-dependent charged particle energy deposition functions as input into the general cavity theory formalism. The integrals associated with this formalism were computed with robust integration techniques.

Results: Cavity doses predicted by the general cavity theory formalism agree well with full MC simulations. For a transport cutoff of 1 keV and a 1.25 MeV beam incident on a chamber with copper walls, the largest difference from full MC simulations was 0.13% over all cavity heights. All other general cavity theory predictions were better than, or equal to, Spencer-Attix cavity theory predictions. Formalism calculations required a fraction of the computing time of the full cavity dose ratio calculations.

Conclusion: A general cavity theory can be formulated to accurately predict ion chamber cavity doses over a broad range of physical conditions where traditional formalisms are considered inapplicable.

Dosimetric characterization of individual electron FLASH beam pulses from a LINAC using radioluminescence and Cherenkov imaging

Mahbubur Rahman¹, M. Ramish Ashraf¹, Rongxiao Zhang^{1,2,3}, David J. Gladstone^{1,2,3}, Xu Cao¹, Benjamin B. Williams^{1,2,3}, P. Jack Hoopes^{1,2,3,4}, Brian W. Pogue^{1,3,4}, and Petr Bruza¹

¹Thayer School of Engineering, Dartmouth College, Hanover, NH,
mahbubur.rahman.th@dartmouth.edu

²Department of Medicine, Radiation Oncology, Geisel School of Medicine, Dartmouth College Hanover, NH

³Norris Cotton Cancer Center, Dartmouth-Hitchcock Medical Center, Lebanon, NH

⁴Department of Surgery, Geisel School of Medicine, Dartmouth College, Hanover NH

Purpose: Spatiotemporal beam profiling for electron FLASH radiation via Cherenkov emission and radioluminescence imaging was investigated using intensified CMOS cameras.

Material & Methods: Cameras gated to LINAC pulses, imaged radioluminescence and Cherenkov emission signals incited by single pulses of ultra-high dose rate (UHDR, >40 Gy/s) 10 MeV electron FLASH irradiation delivered from a clinical linear accelerator at the treatment room isocenter. One camera imaged the entrance Cherenkov emission from a solid water phantom surface or scintillation from a screen on top of the phantom. A second camera imaged the projected depth profile from a tank filled with water and quinine sulfate solution with and without a 450 nm peak bandpass filter. The optical results were compared to lateral dose profiles measured by Gafchromic film at the surface and different depths.

Results: Following ~5-7 ramp-up pulses, the per pulse beam output, from Cherenkov imaging, agreed with the photomultiplier tube (PMT) Cherenkov output to within 3%. Compared to film measurements, Cherenkov emission and scintillation images were linear with dose ($R^2=0.987$, 0.995 , respectively) and showed dose rate independence to at least 300 Gy/s. The surface dose distribution from film agreed more with scintillation than Cherenkov emission imaging (3%/3mm gamma pass rate of 98.9% and 88.8% respectively). Using a 450 nm bandpass filter, the quinine sulfate-based water imaging of the projected depth optical profiles and projected film dose agreed within 5%.

Conclusion: The dose distribution of the UHDR beam was resolved with a single pulse (60 Hz) temporal and 1mm spatial resolution. The agreement of scintillation screen imaging with film measured dose suggests it can accurately verify the consistency of daily beam quality assurance parameters. The cross-validation of Cherenkov images with PMT temporal profile of each pulse suggest it can monitor beam output but required its optical filtering to acquire accurate dose via quinine sulfate-based water imaging.

Acknowledgements

This work was supported by the Norris Cotton Cancer Center seed funding through core grant P30 CA023108 and through seed funding from the Thayer School of Engineering, as well as support from grant R01 EB024498.

References

- 1) Ashraf MR, Bruza P, Krishnaswamy V, Gladstone DJ, Pogue BW. Technical Note: Time-gating to medical linear accelerator pulses: Stray radiation detector. *Med Phys*. Published online December 14, 2018. doi:10.1002/mp.13311
- 2) Birks JB. *The Theory and Practice of Scintillation Counting*. 1st ed. Pergamon; 1964.
- 3) Favaudon V, Lentz J-M, Heinrich S, et al. Time-resolved dosimetry of pulsed electron beams in very high dose-rate, FLASH irradiation for radiotherapy preclinical studies. *Nucl Instrum Methods Phys Res Sect Accel Spectrometers Detect Assoc Equip*. 2019;944:162537. doi:10.1016/j.nima.2019.162537
- 4) Glaser AK, Zhang R, Gladstone DJ, Pogue BW. Optical dosimetry of radiotherapy beams using Cherenkov radiation: the relationship between light emission and dose. *Phys Med Biol*. 2014;59(14):3789-3811. doi:10.1088/0031-9155/59/14/3789
- 5) Helo Y, Rosenberg I, D'Souza D, et al. Imaging Cerenkov emission as a quality assurance tool in electron radiotherapy. *Phys Med Biol*. 2014;59(8):1963-1978. doi:10.1088/0031-9155/59/8/1963
- 6) Rahman M, Bruza P, Langen KM, et al. Characterization of a new scintillation imaging system for proton pencil beam dose rate measurements. *Phys Med Biol*. Published online May 19, 2020. doi:10.1088/1361-6560/ab9452
- 7) Rahman M, Ashraf MR, Zhang R, et al. Electron FLASH Delivery at Treatment Room Isocenter for Efficient Reversible Conversion of a Clinical LINAC. *International Journal of Radiation Oncology*Biophysics*. Published online January 2021. doi:10.1016/j.ijrobp.2021.01.011
- 8) Zlateva Y, Muir BR, Seuntjens JP, El Naqa I. Cherenkov emission-based external radiotherapy dosimetry: II. Electron beam quality specification and uncertainties. *Med Phys*. 2019;46(5):2383-2393. doi:10.1002/mp.13413

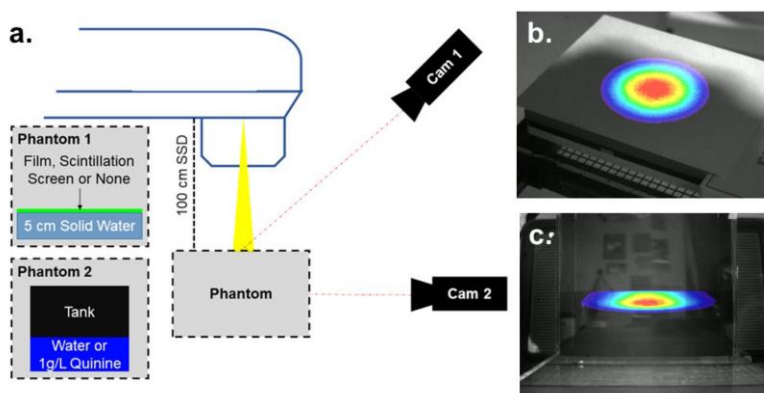


Figure 1. a. Experimental set up for imaging beam profiles using a time-gated intensified cameras and example single frame images acquired with b. camera 1 for cross-beam profile imaging and c. camera 2 for view of projected depth profiles. Scintillation screen was composed of $\text{Gd}_2\text{O}_2\text{S:Tb}$.

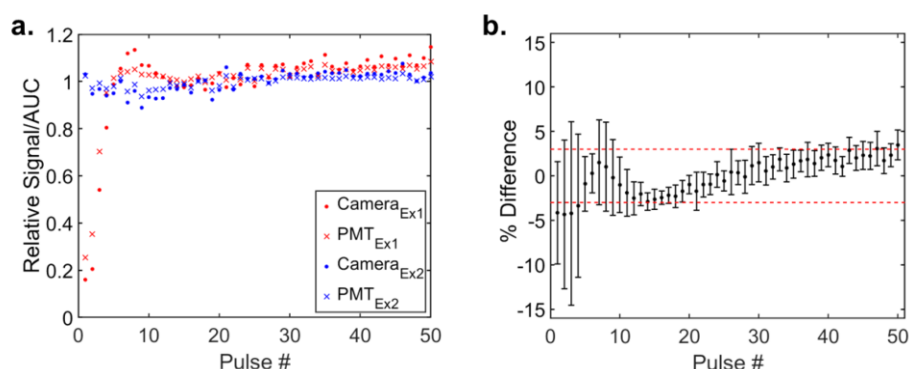


Figure 2. Per pulse beam output measured by the Cherenkov emission from the camera and from a fiber coupled to a photomultiplier tube, normalized to the mean of the 50 pulses a. Two acquisitions demonstrating very different beam ramp-up characteristics during the first few pulses of the beam delivery, b. Percent relative difference between camera and PMT signal based on 15 acquisitions.

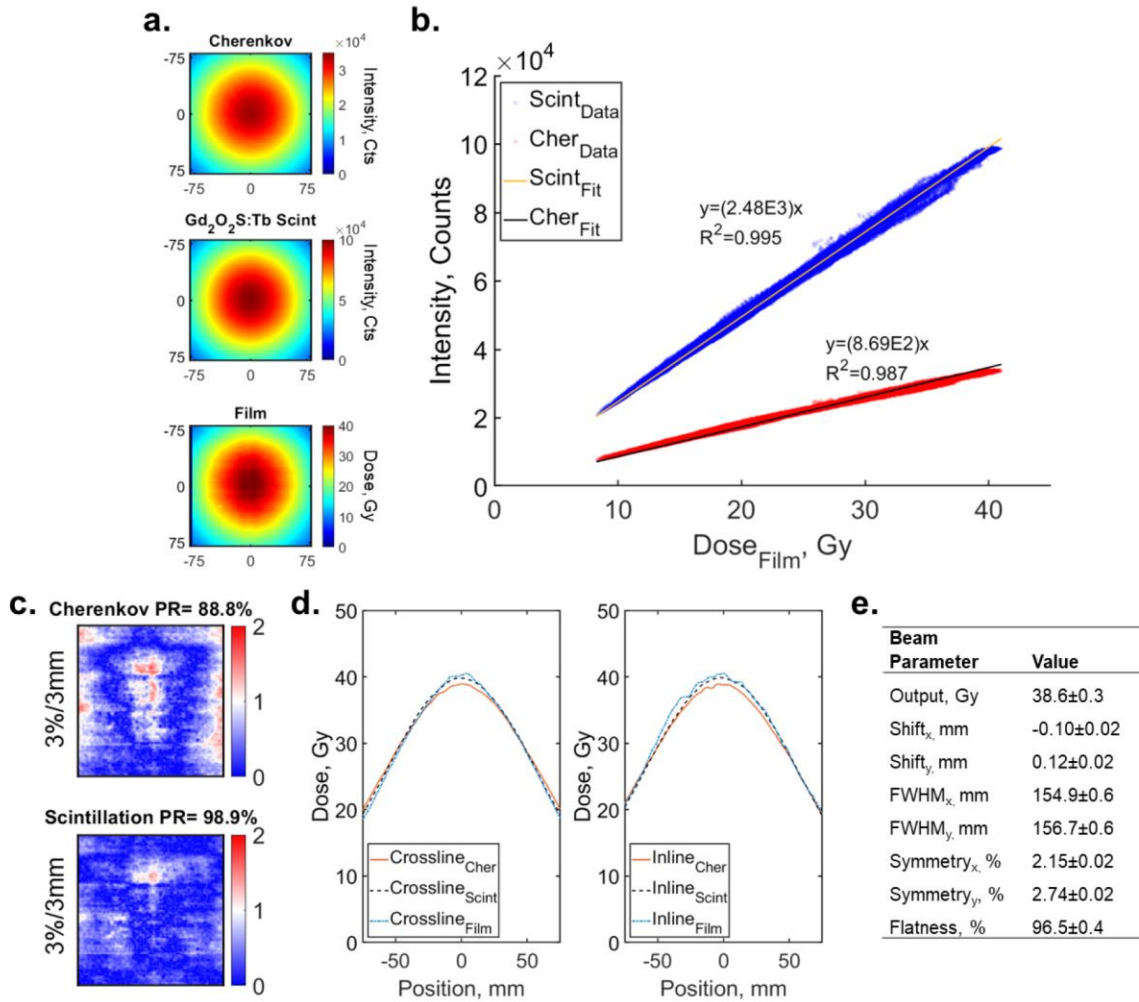


Figure 3. **a.** Surface beam profile at isocenter from solid water produced Cherenkov, scintillation screen, and EBT-XD Gafchromic film (1x1 mm² pixel resolution, 160x160 mm² field of view). Optical images were transformed to beam's eye view **b.** A highly linear correlation of Cherenkov and scintillation intensity to the film dose values in each pixel are demonstrated. Comparison of surface profiles measured by Cherenkov and scintillation screen to film using **c.** 3%/3mm gamma analysis with a 10% threshold and **d.** lateral profile views. **e.** Beam surface profile characteristics based on scintillation imaged dose profile. Output was from an ROI mean of 2x2 cm² at the center of the beam. Shift and FWHM determined via a 2D gaussian fit, flatness was defined as $100 \times \frac{D_{max}-D_{min}}{D_{max}+D_{min}}$ within an

area of 80% of the 40x40 cm² field, and symmetry was defined as $\max_{i \in n} \frac{D_i - D_{-i}}{D_{Cax}} \times 100$ (i is with respect to the isocenter of the or Cax of the treatment room).

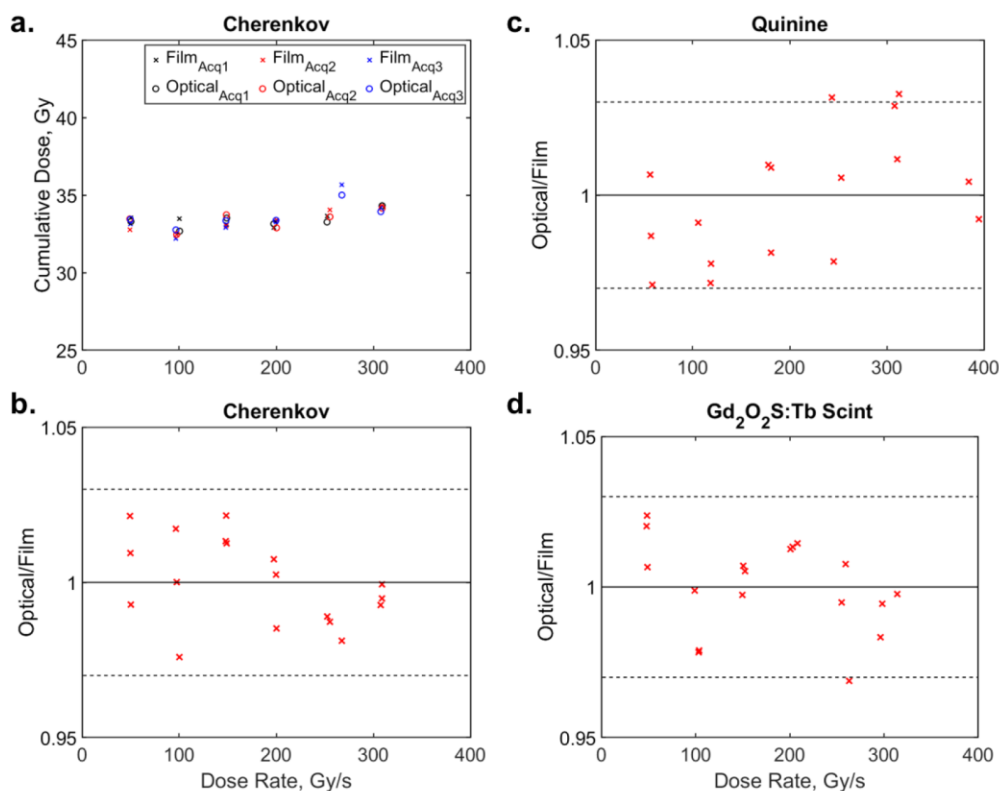


Figure 4. a. Example cumulative acquisition for Cherenkov in comparison to film. Independence of b. Cherenkov, c. scintillation screen and d. quinine sulfate solution response with varying FLASH dose rates.

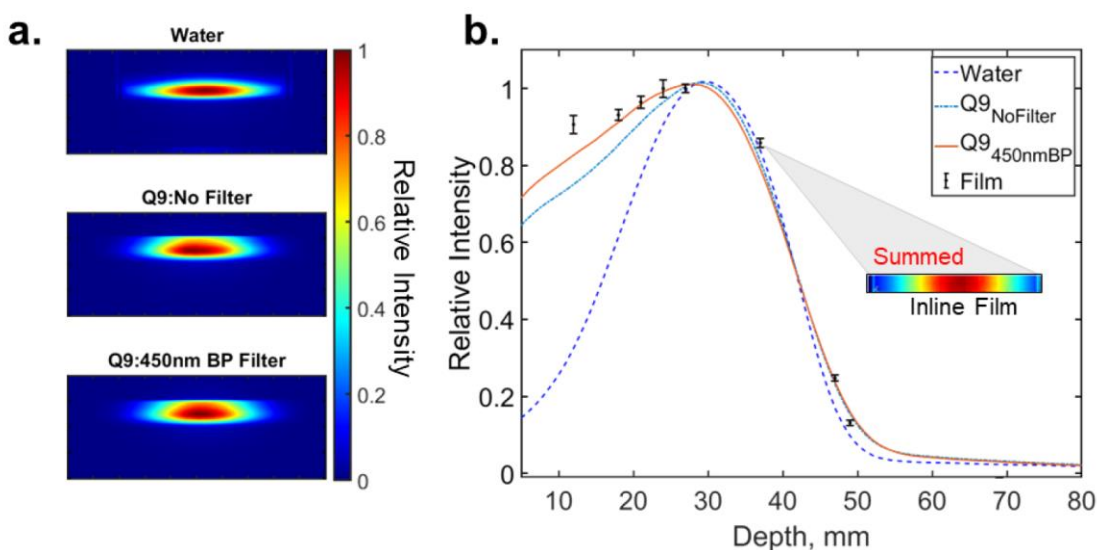


Figure 5. Comparison of projected depth dose profiles using water, 1 g/L quinine sulfate solution, and 450 nm (50 nm width) bandpass filter. a. Projected intensity profiles acquired b. Projected relative depth dose profiles along the central axis and visual of how the inline film strips were used to acquire projected dose along the central axis.